

**Doctoral Dissertation (Shinshu University)**

**Measuring and Managing the Forests at Purple  
Mountain National Forest Park in Nanjing, China  
Using Different Sensor Data by Combining RS,  
GIS and GPS Technologies**

**March, 2015**

**Department of Mountain and Environmental Science**

**Shinshu University**

**Songqiu DENG**

# Content

<b>Abstract</b> .....	i
<b>Chapter 1 Introduction</b> .....	1
<b>1.1 Forest Measurement at the Individual Level</b> .....	1
<b>1.2 Estimation of Forest Aboveground Biomass</b> .....	6
<b>1.3 Present Condition of Chinese Forests</b> .....	11
<b>Chapter 2 Materials and Methods</b> .....	13
<b>2.1 Study Area</b> .....	13
<b>2.2 Field Measurements</b> .....	16
<b>2.3 Satellite Imagery and GIS Data</b> .....	20
<b>Chapter 3 Interpretation of Forest Resources at the Individual Tree Level</b> .....	24
<b>3.1 Data Analysis Method</b> .....	24
<b>3.1.1 Interpretation of Tree Tops</b> .....	24
<b>3.1.2 Supervised Classification and Counting for Different Tree Species</b> .....	27
<b>3.2 Results</b> .....	29
<b>3.2.1 Interpretation of Tree Tops</b> .....	29
<b>3.2.2 Pixel-Based Supervised Classification of Tree Species</b> .....	32
<b>3.2.3 Object-Based Supervised Classification of Tree Species</b> .....	40
<b>3.2.4 Counting Trees of Different Species in the Study Area</b> .....	42
<b>3.3 Discussions</b> .....	44
<b>3.4 Conclusions</b> .....	52
<b>Chapter 4 Estimating Forest Aboveground Biomass</b> .....	53
<b>4.1 Data Analysis Method</b> .....	53
<b>4.1.1 Field Data</b> .....	54
<b>4.1.2 PALSAR Pre-Processing</b> .....	55
<b>4.1.3 Polarimetry and Other Parameters of the PLR/PALSAR Data</b> .....	57
<b>4.1.4 Calculating NDVIs and CVIs (Combined Volume Index)</b> .....	58
<b>4.1.5 Establishing the Relationships between the Observed AGB and Parameters</b> .....	60

4.1.6 Error Assessments of Estimated to Observed AGB.....	64
4.2 Results .....	66
4.2.1 Estimating Forest Biomass Using the FBD/PALSAR Data .....	66
4.2.2 Estimating Forest Biomass Using the PLR/PALSAR Data .....	68
4.2.3 Estimating Forest Biomass Using the WorldView-2 Data.....	69
4.2.4 Estimating Forest Biomass Using the CVIs .....	70
4.2.5 Estimating Forest Biomass by Combining the PALSAR and WorldView-2 Sensors.....	72
4.2.6 Best Estimated Model Selection and AGB Mapping in Study Area .....	74
4.2.7 The Effects of Forest Type and Vertical Structure on AGB Estimation ...	79
4.2.8 The Effects of Other Factors on AGB Estimation .....	81
4.3 Discussions .....	84
4.4 Conclusions .....	94
Chapter 5 Object-based Classification of Forest Types .....	96
5.1 Data Analysis Method .....	96
5.2 Results and discussions .....	97
5.2.1 Subset of the Study Area.....	97
5.2.2 Segmentation.....	98
5.2.3 Land Cover Classification .....	101
5.2.4 Forest Type Classification.....	105
5.3 Conclusions .....	108
Chapter 6 Management of Forests in the Study Area.....	109
6.1 Database Establishment.....	109
6.2 Priority Level of Forest Management.....	112
6.3 Conclusions .....	116
Acknowledgments .....	118
References .....	121

## **Abstract**

Forest resource information, such as species composition, stem density and DBH, is the basis of sustainable forest management. This study first attempted to measure forest resources at the individual tree level using high-resolution images by combining GPS, RS, and Geographic Information System (GIS) technologies. The images were acquired by the WorldView-2 satellite with a resolution of 0.5 m in the panchromatic band and 2.0 m in the multispectral bands. Field data of 90 plots were used to verify the interpreted accuracy. The tops of trees in three groups, namely  $\geq 10$  cm,  $\geq 15$  cm, and  $\geq 20$  cm DBH (diameter at breast height), were extracted by the individual tree crown (ITC) approach using filters with moving windows of  $3 \times 3$  pixels,  $5 \times 5$  pixels and  $7 \times 7$  pixels, respectively. In the study area, there were 1,203,970 trees of DBH over 10 cm, and the interpreted accuracy was  $73.68 \pm 15.14\%$  averaged over the 90 plots. The numbers of the trees that were  $\geq 15$  cm and  $\geq 20$  cm DBH were 727,887 and 548,919, with an average accuracy of  $68.74 \pm 17.21\%$  and  $71.92 \pm 18.03\%$ , respectively. The pixel-based classification showed that the classified accuracies of the 16 classes obtained using the eight multispectral bands were higher than those obtained using only the four standard bands. The increments ranged from 0.1% for the water class to 17.0%

for *Metasequoia glyptostroboides*, with an average value of 4.8% for the 16 classes. In addition, to overcome the “mixed pixels” problem, a crown-based supervised classification, which can improve the classified accuracy of both dominant species and smaller classes, was used for generating a thematic map of tree species. The improvements of the crown- to pixel-based classification ranged from –1.6% for the open forest class to 34.3% for *Metasequoia glyptostroboides*, with an average value of 20.3% for the 10 classes. All tree tops were then annotated with the species attributes from the map, and a tree count of different species indicated that the forest of Purple Mountain is mainly dominated by *Quercus acutissima*, *Liquidambar formosana* and *Pinus massoniana*. The findings from this study lead to the recommendation of using the crown-based instead of the pixel-based classification approach in classifying mixed forests.

Additionally, enhanced methods are required for mapping the forest aboveground biomass (AGB) over a large area in Chinese forests. This study attempted to develop an improved approach to retrieving biomass by combining PALSAR (Phased Array type L-band Synthetic Aperture Radar) and WorldView-2 data. A total of 33 variables with potential correlations with forest biomass were extracted from the above data. However, these parameters had poor fits to the observed

biomass. Accordingly, the synergies of several variables were explored to identify improved relationships with the AGB. Using principal component analysis and multivariate linear regression (MLR), the accuracies of the biomass estimates obtained using PALSAR/ALOS and WorldView-2 data were improved to approximately 65% to 71%. In addition, using the additional dataset developed from the fusion of FBD (fine beam dual-polarization) and WorldView-2 data improved the performance to 79% with an RMSE (root mean square error) of 35.13 Mg/ha when using the MLR method. Moreover, a further improvement ( $R^2 = 0.89$ , relative RMSE = 17.08%) was obtained by combining all the variables mentioned above. For the purpose of comparison with MLR, a neural network approach was also used to estimate the biomass. However, this approach did not produce significant improvements in the AGB estimates. Consequently, the final MLR model was recommended to map the AGB of the study area. Finally, analyses of estimated error in distinguishing forest types and vertical structures suggested that the RMSE decreases gradually from broad-leaved to coniferous to mixed forest. In terms of different vertical structures (VS), VS3 has a high error because the forest lacks undergrowth trees, while VS4 forest, which has approximately the same amounts of stems in each of the

three DBH (diameter at breast height) classes ( $DBH > 20$ ,  $10 \leq DBH \leq 20$ , and  $DBH < 10$  cm), has the lowest RMSE. This study demonstrates that the combination of PALSAR and WorldView-2 data is a promising approach to improve biomass estimation.

Because most plantations of China received little management, many problems arose in these man-made forests, e.g., low species richness and diversity, little landscape-level diversity, and poor growth because of high planting densities. The poor scenic and ecological value of most Chinese forests cannot meet the requirements of modern forestry. Therefore, improving the quality of the existing forests has become an urgent topic of study in China. Currently, thinning and replanting are the two most common methods of forest management in China. Accordingly, the forests at Purple Mountain were classified into three types: broadleaved, coniferous, and mixed forest by an object-based classification approach using a recent Landsat-8 imagery. Finally, we developed some recommendations for the management of the forests in the study area based on the results of the above studies.

**Keywords** Forest measurement; WorldView-2; PALSAR; Landsat-8; Synergy; Individual tree crown approach; Object-based classification; Stepwise regression; Forest management; Purple Mountain National Forest Park

# **Chapter 1 Introduction**

## **1.1 Forest Measurement at the Individual Level**

Traditional field surveys for forest resource management include the number of trees, species and measurements of DBH and tree height in small sample plots. Three to five plots are usually established in each compartment (the minimum unit of forest management). The structure of the entire forest resource is estimated by multiplying these measured values by the total forest area. However, this method is less accurate for large forests in which stand conditions, species and stem densities vary [1]. It is nearly impossible to obtain spatially-explicit stand information on tree species composition and distribution patterns over large areas purely on the basis of field assessments [2]. However, because the forests of China are vast, with a total area of approximately 195.45 million hectares in 2008 [3], conducting national forest inventories by the sample plot method every five years is too costly and time-consuming. Therefore, the acquisition of spatially detailed forest information over large areas by other enhanced methods has become an urgent topic of study [4,5].

This task has been enabled by the advent of remote sensing techniques, which can obtain various types of spatial information simultaneously, such as the coverage type of the ground surface,



position, and DEM (Digital Elevation Model) data. The launch of the LANDSAT satellite in 1972 enabled the study of forests at a global scale. For tree species classification at the crown scale in forests with high species diversity, data with both high spatial and spectral resolution that can identify objects of small sizes, such as cars and tree crowns, are required [6–8]. Since the 1990s, airborne digital sensors with four multispectral bands and very high spatial resolution have been applied successfully for forest studies in developed countries, such as the USA, Canada, Germany and Japan [9–12]. However, due to their wide field of view, aerial photos are subject to strong effects caused by the bi-directional reflectance characteristics of most land cover types [2]. Depending on the sun-view-geometry, which varies with the position of the object within the image, the spectral signature of an object can differ significantly [2]. Although these effects can be useful in special image analysis techniques [13], they are usually regarded as a limiting factor in the automated analysis of aerial images. Due to high costs and their limited availability, airborne data have gained only limited acceptance for operational use.

Commercial satellites, including IKONOS, QuickBird, GeoEye-1 and WorldView-2, were launched successfully in 1999, 2001, 2008 and 2009, respectively. These satellites can obtain imagery at low cost

for several areas simultaneously with a very high resolution of 1 m or less in panchromatic mode, enabling the measurement of forest resources at the individual tree level by satellite remote sensing and computer technology [14–16]. In recent years, the damaged ecological environment of China has required forest conservation instead of wood harvest. For the purpose of forest protection, many forest parks and nature reserves have been established in China, and most of them have been transformed from state-owned forest farms whose goal of operation in the past was the production of wood. However, because of little management, there were many problems in these young man-made forests, such as low species richness and diversity, simple structure and poor growth because of high density. The management of these areas requires spatially detailed information concerning the forest on a large scale. In addition, in modern forest management, the selective thinning approach was used to replace the traditional clear-cutting of trees. Accurate forest information at the individual tree level is of high importance for the selection of target trees. Therefore, individual tree crown delineation methods have received greater attention from researchers in the forest remote sensing field [17–20].

Several algorithms can automate tree crown delineation. Extraction methods for delineating tree crowns include three main approaches:

bottom-up, top-down and template matching algorithms. The valley-following method is a bottom-up algorithm. Top-down algorithms can be divided into watershed, multiple-scale edge segments, threshold-based spatial clustering and double-aspect methods. The template-matching algorithms match a synthetic image model or template of a tree crown to radiometric values [21–23]. The valley-following method, developed by Gougeon [24], has been successfully used to extract tree crowns and tops of man-made coniferous forests in temperate zones by using aerial photographs [18–20]. Additionally, the individual tree crown (ITC) approach using the valley-following method has been successfully programmed by the Pacific Forestry Centre of the Canadian Forest Service, which made it possible to delineate tree crowns and tops on a large scale. This approach can be used to gather detailed crown information at the stand level over a large area for forest inventories [14]. However, the usefulness of this method for various types of vegetation remains to be verified. In addition, few studies of the semi-automatic extraction of tree tops, the delineation of tree crowns, and tree quantifications of forests using satellite images with high resolution have been reported [2,25].

The WorldView-2, a new satellite-borne sensor, was launched by

DigitalGlobe in 2009. Its very high spatial resolution (0.5 m in the panchromatic band and 2.0 m in multispectral bands) and four new multispectral bands (Coastal, Yellow, Red-Edge and NIR2) in addition to the four standard bands (Blue, Green, Red and NIR1) were expected to have high potential for forest studies, because the satellite provides more abundant multispectral information compared to traditional optical sensors [2,26,27]. In this study, using WorldView-2 data, we attempt to first quantify the forest resources of the Purple Mountain in Nanjing at the tree level by applying the ITC approach, a semi-automatic approach of tree crown delineation with a valley-following algorithm, and tree top extraction with a local maxima filtering technique [28]. We also hope to clarify the validity of this method for various forest types with complicated spatial structures in the transitional zone between subtropical and warm-temperate forests. Therefore, the entire mountain, which is mainly composed of man-made single forests, secondary deciduous forest and coniferous-broadleaved mixed forest dominated by *Pinus massoniana*, *Liquidambar formosana* and *Quercus acutissima*, was the object of interest in this study. Finally, we focus on the question of whether the four additional bands of WorldView-2 can improve the classification accuracy significantly compared to the four standard

bands.

## **1.2 Estimation of Forest Aboveground Biomass**

Precise quantification of forest aboveground biomass (AGB) on a regional to global scale is of increasing importance in the context of reducing emissions from deforestation and forest degradation in developing countries (REDD+) and compliance with the Kyoto Protocol [29–31]. In a forest inventory, the sample plotting method provides very accurate AGB values at the plot level [32]. Due to the high cost of this traditional plot-based investigation for AGB and the difficulties of its implementation in remote areas, interest in the use of remotely sensed data acquired from spaceborne or airborne sensors to estimate forest AGB has increased in recent decades. Remote sensing provides a key source of data for updated, consistent, and spatially explicit assessment of forest biomass and its dynamics, particularly in large countries with limited accessibility [33,34].

Optical images have long been used to estimate forest parameters and assess wood biomass [35–37]. Estimating the AGB has been mainly achieved by using spectral reflectance and/or vegetation indices, such as the normalized difference vegetation index (NDVI), which is computed from the red and near-infrared (NIR) bands [38–40]. However, a major limitation of vegetation indices is that these

indices reach a saturation level during the estimation of high-density biomass [41–43]. The saturation point varies greatly depending on the source data and the vegetation type and ranges from 15 to 100 Mg/ha for visible/NIR vegetation indices [39,44]. Other studies have also indicated that the NDVI approaches a saturation level when the vegetation age is greater than 15 years in tropical forests [36]. In addition, optical remote sensing provides limited information on the vertical distribution of forest structure [45], and compiling a temporally and radiometrically consistent cloud-free datasets over large areas is not always possible [34].

Over the past two decades, a large number of researchers have contributed to the study of the application of radar (Radio Detection and Ranging) for forestry [46,47]. Many studies have shown that forest biomass can be retrieved using SAR (Synthetic Aperture Radar) data because SAR can penetrate cloud and forest canopies [48–50]. The major advantage of all SAR systems is the weather- and daylight-independency of the system [48,51,52]. In addition, numerous studies have also reported that long-wavelength (e.g., L and P bands) SAR is more appropriate than short-wavelength (e.g., X and C bands) SAR for forest biomass estimations [53,54]. In this case, the detected radiation is mostly due to backscattering from the branches

and stems of the trees, and thus L- and P-band SAR should respond characteristically to forest volume and biomass [50,55,56]. Additionally, long wavelength can travel without having a sight. The successful launch of ALOS (Advanced Land Observing Satellite) in 2006 increased the potential for the use of radar to measure AGB because PALSAR/ALOS is the first long-wavelength (L-band, 23-cm wavelength) SAR satellite sensor with the capability of collecting cross-polarized HV (horizontal-send, vertical-receive) and VH (vertical-send, horizontal-receive) data in addition to HH (horizontal-send, horizontal-receive) and VV (vertical-send, vertical-receive) data. Although the ALOS satellite stopped to operate in April 2011, the systematically collected PALSAR data from this satellite show great potential for AGB estimates on a large scale [53,57,58]. However, AGB estimation using the biomass-PALSAR backscattering relationship remains problematic due not only to the saturation at high biomass levels (*i.e.*, the backscatter power no longer increases with AGB or volume) but also to the spatial heterogeneity of forests, which can generate unclear data [31,49,59].

Light detection and ranging (LiDAR) data can provide detailed vegetation structure measurements at discrete locations covering circular or elliptical footprints from a few centimeters to tens of

meters in diameter [60,61]. LiDAR instruments mounted on airplanes emit active laser pulses and measure various echoes of the signal, resulting in accurate AGB estimations for various forests with no saturation at higher biomass levels [62–64]. However, LiDAR systems are often limited to airborne acquisition, which is better suited to providing samples (e.g., transects) rather than full wall-to-wall coverage over large areas [32,65,66]. Therefore, even though LiDAR provides the best estimates of forest biomass, observations over large areas remain problematic, making complete coverage at landscape and regional scales uncommon, with data costs often dictating government support for LiDAR or its inclusion in collection activities [67].

The globally and freely available Landsat TM (Thematic Mapper) and ETM+ (Enhanced Thematic Mapper Plus) data, which have a medium resolution (30 m for TM/ETM+ multispectral bands), have been widely used for mapping forest biomass on a regional to global scale in numerous studies [34,42,68,69]. However, the limited spatial detail misses small-scale biomass variability. In recent years, the successful launch of a number of commercial satellites with high resolution from tens of centimeters to a few meters (e.g., IKONOS, QuickBird, SPOT5, GeoEye-1, WorldView-1&2) has provided an approach to this problem. The WorldView-2, launched in October



2009, acquires data with more multispectral bands (eight bands) and higher spatial resolution (0.5 m in the panchromatic band and 2 m in the multispectral bands) than previously launched satellite sensors while reducing the unnecessary redundancy found in hyper-spectral data [70]. These high spectral and spatial resolutions were expected to have great potential for forest studies [37]. WorldView-2 images have been successfully used for land cover classification and tree species identification with higher accuracy than that obtained using traditional sensors with four bands [2,71,72]. However, few studies have used WorldView-2 data to estimate forest AGB [73].

Recently, the fusion of optical, radar, and/or LiDAR data for estimating forest biomass has become a popular approach that attempts to overcome the limitations associated with the use of single sensors. However, most studies of these studies have mainly focused on temperate and tropical forests [43,54,61,62,66,74,75]. Estimating forest biomass in China has mainly been achieved by conducting national forest inventories using the sample plotting method every five years. Because the forests of China are vast, with a total area of approximately 195.45 million hectares in 2008 [3], developing improved remotely sensed methods that can accurately retrieve forest biomass on a large scale has become an urgent topic of study. Thus, in

this study, a combination of ALOS PALSAR and WorldView-2 data was used to develop an enhanced approach to AGB retrieval in an attempt to meet the continued need for both new experimental data and further improvement of existing models for biomass estimation.

The aims of the present study were the following:

1. To evaluate the possibility of retrieving forest AGB using WorldView-2 data;
2. To determine if a new index generated from the combination of ALOS PALSAR and WorldView-2 data can increase the AGB inversion accuracy;
3. To assess the potential of combining ALOS PALSAR and WorldView-2 data to map the forest AGB; and
4. To compare the predictive capability of the multivariate stepwise model with that of an artificial neural network (ANN) model for estimating biomass.

### **1.3 Present Condition of Chinese Forests**

Currently, increasing numbers of developing countries are giving special consideration to the planning of green environments in their urban development activities. Consequently, a total of 746 national forest parks have been established in China in the past 30 years (1982–2011) [76]. However, most of these parks were directly

transformed from state-owned forest farms whose purpose had been wood production. As in many countries, almost all of the native forests of China have been harvested through clear-cutting. These forests were replaced by repeated rotations of plantations in the 1950s–1970s [77]. Because these plantations received little management, many problems arose in these young man-made forests, e.g., low species richness and diversity, little landscape-level diversity, and poor growth because of high planting densities [78]. The poor scenic and ecological value of most Chinese forests cannot meet the requirements of modern forest tourism. Therefore, improving the quality of the existing forests has become an urgent topic of study in China.

## **Chapter 2 Materials and Methods**

### **2.1 Study Area**

The study area, Purple Mountain National Park (32°01'–32°06'N, 118°48'–118°53'E) (Figure 1), is a well-known historic and scenic site in China that is popular with tourists. It has an area of approximately 4500 ha and is situated in the center of Nanjing City in southeastern Jiangsu Province, China. The altitude above sea level ranges from 20 to 449 m with an average annual precipitation ranging from 1000 to 1050 mm and average sunshine hours of approximately 2213 h per year. The annual mean temperature is 15.4 °C, with an extremely highest temperature of 40.7 °C in August and an extremely lowest temperature of –14.0 °C in January. The zonal soil color is yellow brown, with purple forest soil found on the northern mountain with a steep slope [71].

The zonal vegetation type in Nanjing is deciduous broad-leaved mixed forest with some evergreen trees. However, because of long-term wars and human disturbances, all of the natural forests in Purple Mountain National Park have been damaged, with the exception of some areas around Linggu Temple and Ming Xiaoling Mausoleum. Since the 1930s, greater attention has been paid to afforestation in the study area. The mountain was covered completely

by forest vegetation until the 1960s. In the late 1970s, many coniferous trees died from pine wilt disease. Many broad-leaved trees, such as *Quercus acutissima* and *Pistacia chinensis*, successfully invaded and grew in the gaps left by this disease. Concurrently, the surviving zonal vegetation recovered favorably because cutting was forbidden. Today, the forests of Purple Mountain are mainly composed of manmade single forests approximately 60 to 80 years of age, as well as secondary deciduous forests and coniferous-broadleaved mixed forests dominated by *Pinus massoniana*, *Quercus fabri*, *Liquidambar formosana*, and *Quercus acutissima* [71].

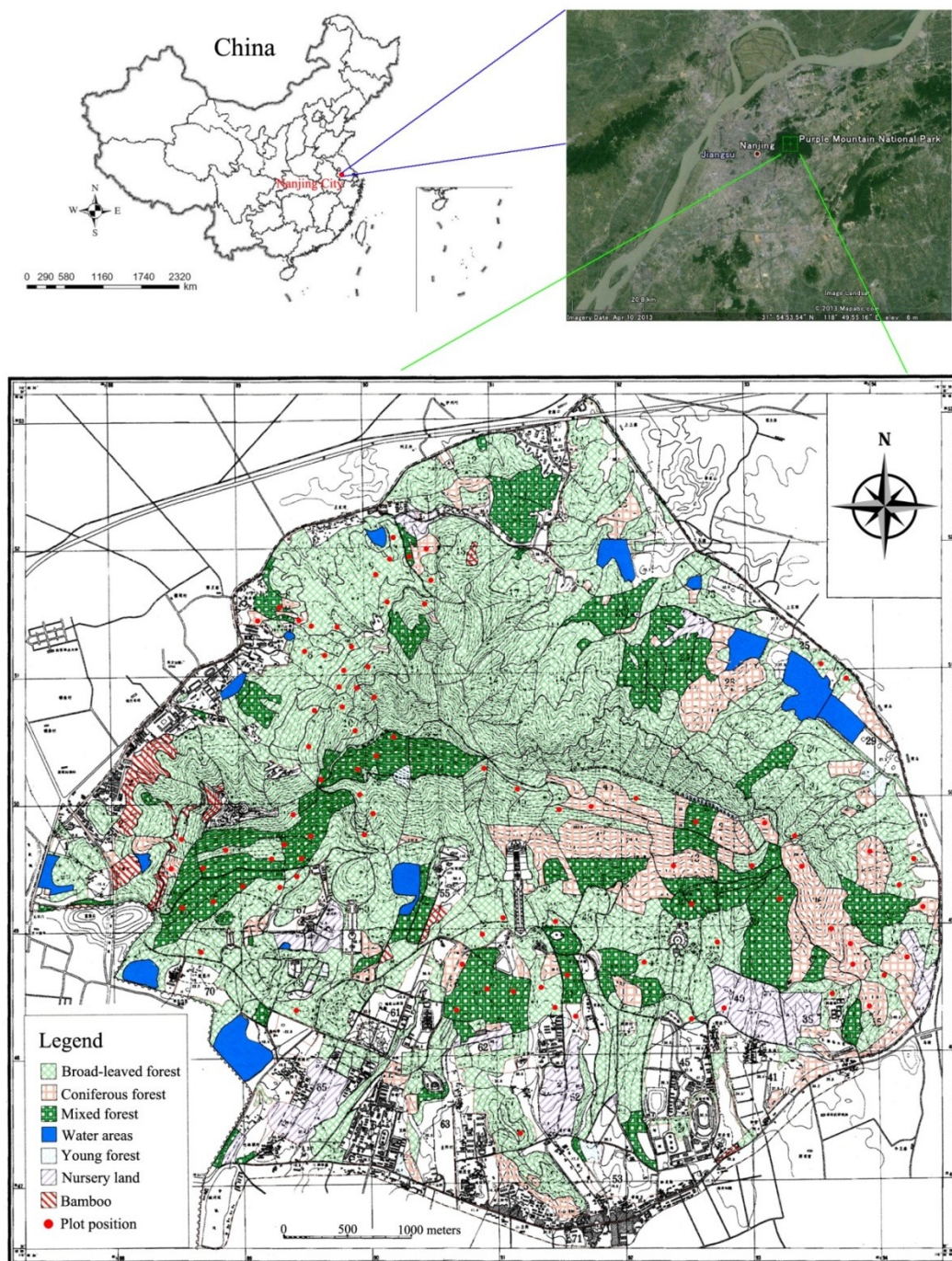


**Figure 1.** Location map of the study area with vegetation types in 2002 and the plot positions investigated in September 2011. The location map was cited from Google Earth, and the vegetation map was from the ArcGIS (GIS, Geographic Information System) database established in 2002.



## 2.2 Field Measurements

In this study, we selected the entire mountain, with an area of approximately 30 km<sup>2</sup>, as the research object. A total of 90 plots with sizes of 15 × 15 m, 20 × 20 m or 25 × 25 m were established in September 2011, for testing the accuracy of the interpretation of the tree tops and the supervised classification of tree species (Figure 1). Most plots had a size of 20 × 20 m. The plots were larger in heterogeneous areas and smaller in homogeneous forests. These plots were chosen on the basis of forest conditions, various terrains, and accessibility for measurement and were distributed in different forest types. The measurements were conducted for different forest growth stages, which ranged from regrowing young forest to dense mature forest.

All trees with a DBH larger than 5 cm were surveyed, and the species, DBH, and height were recorded. In addition, the center of each plot was located by GPS (Garmin MAP 60CS, accuracy ±3 m). All central points of the 90 plots were recorded when the GPS steadily displayed the highest accuracy of ±3 m. The average DBH, tree height, stem density, volume, and AGB in each plot were calculated, and the 90 plots were divided into three stand types: broad-leaved (B), coniferous (C), and mixed (M) forest (Table 1). The conditions of the

90 plots are documented in Table 1.

**Table 1.** The condition of the 90 plots surveyed in September 2011. DBH, diameter at breast height. B, broad-leaved; M, mixed; C, coniferous.

No.	Density (Stem/ha)	Average DBH (cm)	Average Height (m)	AGB (Mg/ha)	Forest Type
1	311	36.2	12.0	272.8	B
2	1956	10.1	8.6	80.6	B
3	1467	13.0	10.0	119.3	M
4	1289	12.4	9.5	100.9	C
5	1378	16.2	10.8	203.1	C
6	844	16.6	11.2	112.7	B
7	1644	12.2	9.4	101.9	M
8	1956	12.7	9.5	165.6	M
9	1100	17.2	11.4	180.1	M
10	1156	16.5	11.1	160.0	M
11	1375	14.0	10.0	117.5	M
12	1244	13.2	9.4	142.0	C
13	2075	10.7	8.4	158.1	C
14	1822	11.6	8.9	170.5	M
15	844	17.8	11.3	170.0	B
16	1644	11.9	8.6	147.7	M
17	1650	13.6	10.4	124.7	B
18	650	15.7	11.1	72.7	M
19	1333	13.0	9.2	159.3	M
20	1125	13.4	9.3	121.7	B
21	1400	10.2	7.9	99.1	B
22	1325	15.4	10.3	341.5	B
23	1156	13.5	9.6	106.2	B
24	978	19.4	12.4	207.1	B
25	1289	12.2	9.2	108.4	B
26	800	16.1	10.3	158.3	M
27	1689	10.8	8.7	103.3	B
28	1689	10.3	8.9	70.0	M
29	1378	11.9	9.3	159.7	B
30	1467	12.2	9.2	126.0	B



**Table 1. *Cont.***

<b>No.</b>	<b>Density (Stem/ha)</b>	<b>Average DBH (cm)</b>	<b>Average Height (m)</b>	<b>AGB (Mg/ha)</b>	<b>Forest Type</b>
31	1422	15.5	10.8	169.1	M
32	1467	15.9	10.8	145.1	M
33	550	27.9	14.4	242.2	M
34	1067	16.6	10.0	278.0	B
35	889	20.4	11.6	268.1	B
36	1200	13.4	9.6	147.7	B
37	1333	11.1	9.4	54.8	B
38	1911	8.4	7.9	51.1	B
39	1800	11.4	9.2	102.4	M
40	800	17.2	11.2	164.0	M
41	933	14.9	10.7	154.1	B
42	2533	9.5	8.0	121.7	M
43	2711	9.3	7.9	195.4	M
44	1556	12.6	9.5	142.0	M
45	1600	12.5	9.4	134.4	M
46	2000	11.9	8.8	176.0	M
47	1422	12.9	9.6	107.7	M
48	711	18.0	11.0	266.3	B
49	1022	12.5	9.4	87.6	M
50	2178	11.2	8.8	153.2	M
51	2178	10.1	8.4	103.6	M
52	1378	12.6	9.4	132.5	M
53	1422	15.4	10.4	204.3	M
54	1778	12.1	9.2	120.4	M
55	1067	13.6	10.1	96.3	M
56	1111	15.3	11.0	106.5	C
57	1200	11.0	8.9	82.4	B
58	1156	14.8	10.3	138.7	B
59	1689	11.9	9.7	90.6	B
60	1911	10.8	8.6	221.6	M
61	1067	10.0	8.0	81.2	M
62	1467	10.6	8.7	121.7	B
63	1111	14.6	10.4	124.0	B

**Table 1. *Cont.***

<b>No.</b>	<b>Density (Stem/ha)</b>	<b>Average DBH (cm)</b>	<b>Average Height (m)</b>	<b>AGB (Mg/ha)</b>	<b>Forest Type</b>
64	1644	13.5	9.8	156.4	C
65	1175	11.5	8.6	100.4	B
66	1250	13.2	9.5	108.3	B
67	533	11.3	9.0	40.4	B
68	533	17.5	11.1	116.6	B
69	889	9.9	8.4	40.7	B
70	1556	10.0	8.2	75.5	M
71	1111	11.4	8.6	155.8	B
72	1778	10.2	8.3	99.7	B
73	1378	15.2	9.9	179.3	B
74	933	17.7	10.9	331.2	B
75	1956	10.1	8.4	140.4	B
76	1911	10.6	8.7	82.8	B
77	1289	13.8	10.4	153.5	B
78	1467	13.5	10.1	115.5	B
79	2000	11.6	9.4	119.0	C
80	978	8.6	7.7	35.5	B
81	1556	14.1	10.5	166.6	C
82	978	20.6	12.7	233.3	B
83	1289	14.9	10.6	129.4	B
84	1022	21.0	12.4	258.5	B
85	800	16.1	11.3	105.7	B
86	933	15.8	10.7	138.2	B
87	400	10.1	8.5	25.5	B
88	356	15.4	11.1	53.3	B
89	1156	18.0	11.7	227.7	B
90	1200	17.8	11.3	192.6	B

## 2.3 Satellite Imagery and GIS Data

One of the optical images was acquired by the WorldView-2 satellite on 10 December 2011 during good weather and clear skies. At this time of the year, the leaves of some of the deciduous tree species had fallen, and some trees had leaves that were turning yellow, while the evergreen trees were full of chlorophyll, providing good conditions for tree species identification and classification. The satellite has a panchromatic band (0.46–0.80  $\mu\text{m}$ ) with 0.5-m ground resolution at the nadir and eight multispectral bands with 2.0-m resolution. In addition to the four standard colors, Blue (0.45–0.51  $\mu\text{m}$ ), Green (0.51–0.58  $\mu\text{m}$ ), Red (0.63–0.69  $\mu\text{m}$ ), and Near Infrared 1 (NIR1) (0.77–0.90  $\mu\text{m}$ ), four new, additional bands were available: Coastal Blue (0.40–0.45  $\mu\text{m}$ ), Yellow (0.59–0.63  $\mu\text{m}$ ), Red-Edge (0.71–0.75  $\mu\text{m}$ ), and Near Infrared 2 (NIR2) (0.86–1.04  $\mu\text{m}$ ). The size of the image was 8868 lines  $\times$  9358 pixels at the nadir with 16-bit data stored, and the geometric projection was UTM (Universal Transverse Mercator) WGS 84 Zone 50 North. The satellite data were ordered as the premium product level, suggesting that the data had been sensor-corrected, ortho-rectified, and geo-corrected by the data provider, DigitalGlobe Inc. [73]. According to DigitalGlobe, the geolocation accuracy of the delivered image ranges from 4.6 m to 10.7

m (CE90). This accuracy was verified by comparing the data to the standard map of the mountain created by an infrared airborne photograph taken in 1991 with an accuracy of 5 m. The two datasets were in good agreement, as verified by matching spatial positions such as the intersections of roads, single buildings, and water areas. The optical data were atmospherically corrected using the Fast Line-of-Sight Atmospheric Analysis of Spectral Hypercubes (FLAASH) algorithm in ENVI 4.8 software. The reflectance values of the eight multispectral bands were then used to calculate vegetation indices and to correlate with the observed forest biomass.

Another optical imagery used for the classification of stand types in our study was acquired by the Landsat-8 satellite on 11 August 2013 during good weather and clear skies. The OLI (Operational Land Imager) sensor of the Landsat-8 satellite has a panchromatic band (0.500–0.680  $\mu\text{m}$ ) with 15-m ground resolution at the nadir and eight multispectral bands with 30-m resolution. In addition to the four standard colors, Blue (0.450–0.515  $\mu\text{m}$ ), Green (0.525–0.600  $\mu\text{m}$ ), Red (0.630–0.680  $\mu\text{m}$ ), and Near Infrared (NIR) (0.845–0.885  $\mu\text{m}$ ), four additional bands were available: Coastal (0.433–0.453  $\mu\text{m}$ ), Short Wavelength Infrared 1 (SWIR1) (1.560–1.660  $\mu\text{m}$ ), Short Wavelength Infrared 2 (SWIR2) (2.100–2.300  $\mu\text{m}$ ), and Cirrus (1.360–1.390  $\mu\text{m}$ ).

The geometric projection of the image was UTM WGS 84 Zone 50 North. The accuracy of the image was verified by comparing the data to the standard map of the mountain created in 1991 with an accuracy of 5 m. The two datasets were in good agreement, as verified by matching spatial positions such as the intersections of roads, single buildings, and water areas.

The two scenes of SAR data used in this study were collected by the ALOS PALSAR sensor in fine beam dual-polarization mode (FBD) (HH and HV polarizations) on 11 October 2010, with an off-nadir angle of  $34.3^\circ$  and in polarimetric mode (PLR) (HH, HV, VH, and VV polarizations) on 22 March, 2011, with an off-nadir angle of  $21.5^\circ$ . These PALSAR datasets were ordered as L1.1 level with the single look complex (SLC) format. The FBD data had a spatial resolution of 9.4 m in slant range and 3.2 m in azimuth. The spatial resolution of the PLR data was 9.4 m in slant range and 3.5 m in azimuth [79]. The detailed processing and analysis approaches of the SAR data will be introduced at the corresponding chapter later.

In addition, in this study, geographic data such as the boundary line of the mountain and the forest base maps were obtained from the ArcGIS (GIS, Geographic Information System) database, which was established in 2002 based on the forest inventory data of 662 plots

investigated by a special project in 2001 [80]. This database was also used to support the field investigation. The field data for the 90 plots surveyed in September 2011 were inputted into the above database, including stem density, average DBH (diameter at breast height of 1.3 m), average tree height, forest type, dominant species, volume, AGB, and GPS (Global Positioning System) data for the plot center. These data were used to test the accuracy of the interpreted tree tops, to perform a supervised classification of tree species, and to test the accuracy of the forest biomass inversion.

## Chapter 3 Interpretation of Forest Resources at the Individual Tree Level

### 3.1 Data Analysis Method

The research flow chart in Figure 2 provides an overview of the methods.

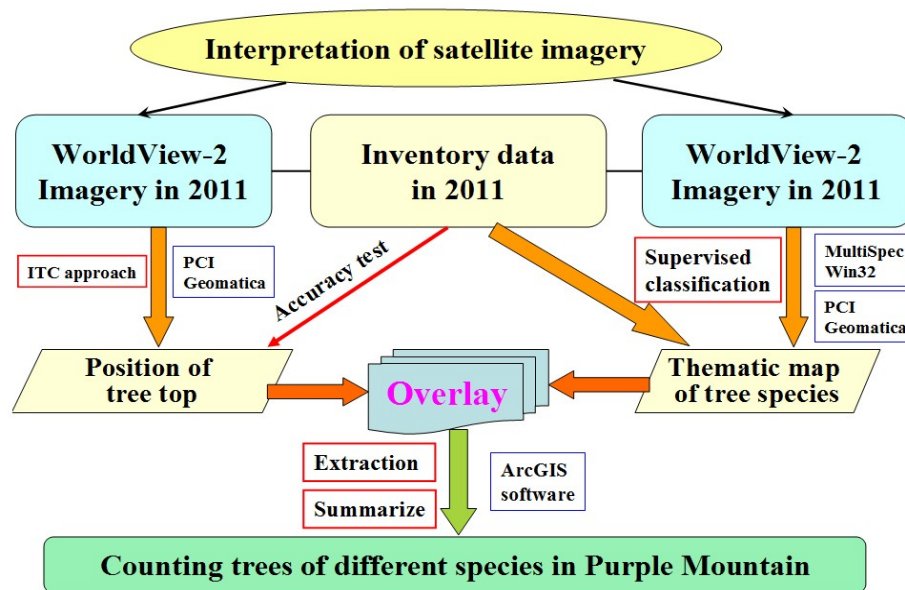


**Figure 2.** Research flow chart. ITC, individual tree crown.

#### 3.1.1 Interpretation of Tree Tops

Tree tops were interpreted with the ITC approach using WorldView-2 imagery in PCI Geomatica v9.1 software with the ITC Suite [18,28,81]. First, preprocessing for tree top interpretations was necessary to normalize the panchromatic band based on its own range in the illumination image, which was performed twice to smooth using an averaging filter of  $5 \times 5$  pixels (2.5 by 2.5 m) [18,28]. Second, an

NDVI (Normalized Difference Vegetation Index) image was generated using the Vegetation Index Image function. Third, a bitmap of the non-vegetation area was automatically created using the NVEG MASK function of the ITC Suite by comparing (normalized or not) the NIR and the visible values [28]. In this step, man-made structures, such as buildings and roads, soil and water zones, were extracted with good results, but some grass areas composed of herbs could not be extracted, because the grasses had similar multispectral characteristics to the forest area; an error in which some forest area was identified as non-vegetation area was generated from the automatic extraction, due to the image acquired in December 2011. These two problems were solved by the following approach: first, the minimum and maximum values of the NDVI and/or panchromatic band were found for the grass and misclassified forest areas (in this study, the panchromatic value of 40 to 80 and the NDVI value of 170 to 195 could be used to separate the grass areas and to correct the misclassified forests, respectively); second, two bitmaps for these areas were established by the THR (Thresholding Image to Bitmap) function; finally, the correct non-forested regions of the image were extracted by the non-vegetation zone plus grass and minus misclassified forest area by the BLO function (Bitmap Logical Operation).



The ITC isolation image was produced by using the valley-following algorithm. Using the normalized panchromatic band and the non-forested mask, this method treats the spectral values as topography, with shaded and darker areas representing valleys and bright pixels delineating the tree crowns [18]. This method produces a bitmap of segments of valley and crown materials in forest areas. A rule-based system follows the boundary of each segment of crown material to create isolations, which are taken to represent tree crowns, while the pixel with the highest gray value at each tree crown is interpreted as the tree top by the local maxima filtering technique [28]. Because of the coverage of canopy trees, small trees in the understory were difficult to interpret [1,11]. Therefore, based on the present condition of the surveyed plots, all forests at Purple Mountain were divided into three groups: trees  $\geq 10$  cm DBH,  $\geq 15$  cm DBH and  $\geq 20$  cm DBH. We attempted to extract the tops of trees in these three groups by using filters with a moving window of  $3 \times 3$  pixels ( $1.5 \times 1.5$  m),  $5 \times 5$  pixels ( $2.5 \times 2.5$  m) and  $7 \times 7$  pixels ( $3.5 \times 3.5$  m), respectively, which, in theory, may extract trees with crown diameters of more than 1.5 m, 2.5 m and 3.5 m, respectively.

The field data for the 90 plots were used to test the accuracy. We verified the correspondence of the observed and estimated tree

densities in the central point of each plot and calculated the accuracy of the interpretation of the tree tops. The interpreted accuracy of tree tops can be calculated by the following formula:

$$\Phi = (1 - |D_I - D_S| / D_S) \times 100 \quad (1)$$

where  $\Phi$  is the interpreted accuracy (%),  $D_I$  is the stem density of trees interpreted by the ITC method and  $D_S$  is the stem density of trees in the surveyed plot.

### **3.1.2 Supervised Classification and Counting for Different Tree Species**

Based on forest inventory data and other information, including photos linked in Google Earth and existing thematic maps, the WorldView-2 imagery of the study area was classified into 16 classes by using a supervised classification process of eight multispectral bands with the Maximum Likelihood algorithm in ERDAS Imagine v8.6 and in MultiSpec Win32. In spite of having attempted to define an exhaustive list of classes and having enhanced the statistics, there will still be some pixels that have a low likelihood of being members of even the most likely class. Though the probability results map will show where these pixels are, the MultiSpec thresholding capability can provide quantitative information about them. For example, if a threshold of 2% is selected, the threshold level will be calculated, such

that 2% of an ideal Gaussian distribution with the same mean vector and covariance matrix will be thresholded in each class [82]. The lower the threshold value is, the higher the rate of classified pixels, whereas the lower the classified accuracy. The threshold was set at the 2% default in our study, because the 2% level had the best classification results compared to other values. Additionally, to overcome the “mixed pixels” problem of the pixel-based classification (*i.e.*, some pixels within a tree crown may be classified into two or more different classes), an object-based supervised classifier (called crown-based classification) was designed for tree species classification in the ITC Suite [28], which was used to generate another thematic map of the tree species in this study. This crown-based classification was completed by the ITCSC (Individual Tree Crown Supervised Classifier) function of the ITC Suite. The ITCSC classified the individual tree crowns (ITCs) of the image into different species using a Maximum-Likelihood (ML) decision rule [28]. The classification was based on comparing the signature of each ITC, one by one, with the ITC-based signatures of the various species. The species signatures were produced by the ITCSSG (Individual Tree Crown Species Signatures Generation) program using the training areas created at the section of the pixel-based classification. Finally,

when the tree tops interpretation and the supervised classification processes were completed, all tree tops were annotated with a species attribute from the species thematic map delineated by the crown-based classification using an overlay by the extraction function in ArcGIS v9.2. The total number of trees of different species at Purple Mountain was counted using the summarize function.

## **3.2 Results**

### **3.2.1 Interpretation of Tree Tops**

In this study, the tree tops of the three groups,  $\geq 10$  cm DBH,  $\geq 15$  cm DBH and  $\geq 20$  cm DBH, were extracted using filters with moving windows of  $3 \times 3$  pixels,  $5 \times 5$  pixels and  $7 \times 7$  pixels, respectively. For the total mountain, there were 1,203,970 trees of DBH over 10 cm, and the accuracy of interpretation was  $73.68 \pm 15.14\%$  (average value and standard deviation) averaged for the 90 plots. The number of trees  $\geq 15$  cm and  $\geq 20$  cm DBH is 727,887 and 548,919, with an average accuracy of  $68.74 \pm 17.21\%$  and  $71.92 \pm 18.03\%$ , respectively.

According to the composition of tree species, the 90 plots were divided into three types: broad-leaved forest, coniferous forest and mixed forest. The average interpretation accuracies of the different forest types in the three groups were calculated as shown in Figure 3

(average value and standard deviation). In the broad-leaved forest, the accuracy in the DBH  $\geq 10$  cm layer was higher than that in the DBH  $\geq 15$  cm layer and the DBH  $\geq 20$  cm layer, indicating that with the growth of broad-leaved trees, the tree tops become difficult to identify, in contrast to coniferous forests [18]. There is no significant difference in accuracy between the three groups for mixed forest.

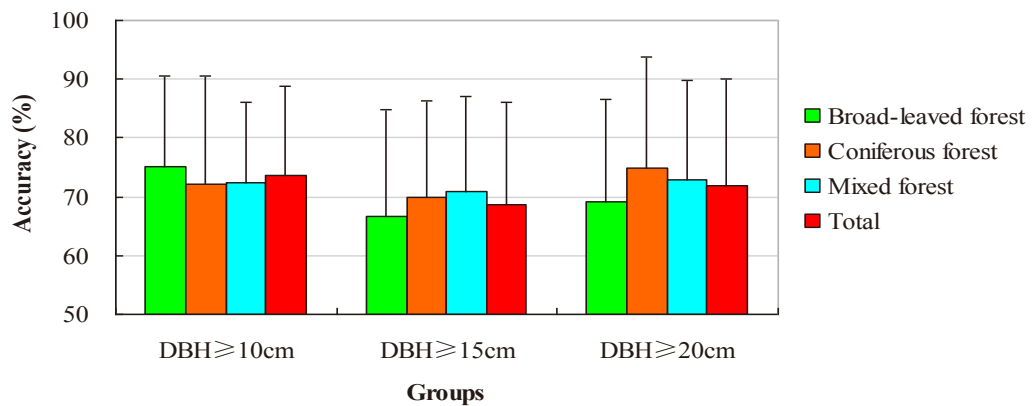
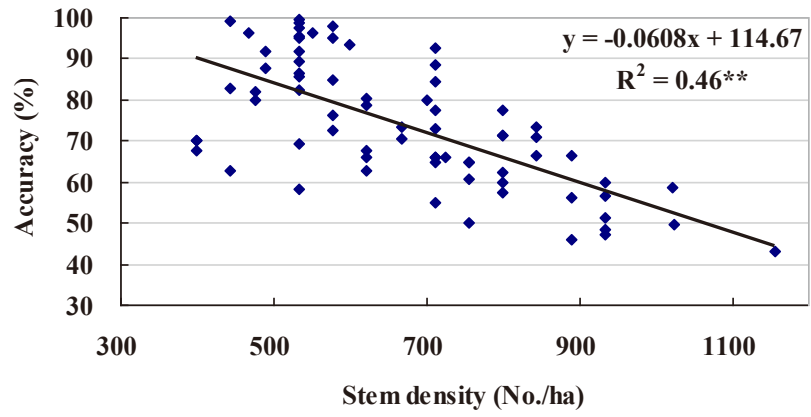
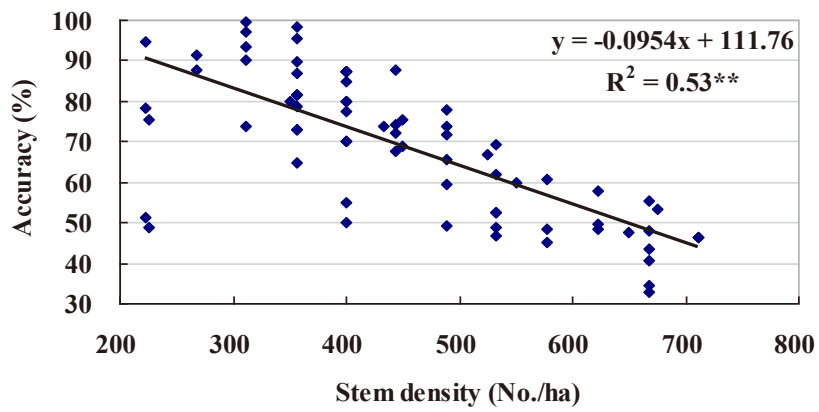


**Figure 3.** The difference in accuracy between forest types for the three groups.

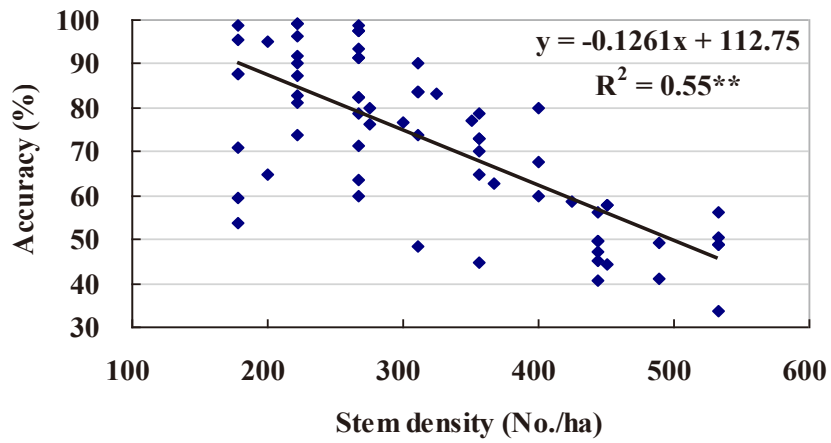
In addition, the effects of stem density in the surveyed plots on interpretation accuracy were analyzed. The regressions of stem density and interpreted accuracy were performed as shown in Figure 4. The results indicate that the accuracy decreases as the stem density increases, because the chance of overlap between crowns increases with incremental stem density.



(a)



(b)



(c)

**Figure 4.** Regression of accuracy and stem density of the surveyed plots. (a)  $3 \times 3$  pixels for  $DBH \geq 10$  cm; (b)  $5 \times 5$  pixels for  $DBH \geq 15$  cm; (c)  $7 \times 7$  pixels for  $DBH \geq 20$  cm.

### **3.2.2 Pixel-Based Supervised Classification of Tree Species**

Based on forest inventory data and other information, a supervised classification was performed on the WorldView-2 imagery with eight multispectral bands in the MultiSpec Win32 software. The imagery was classified into two types of land cover with a total of 16 classes. One of these types was non-forested area with five classes: building, water, soil, road and grass; and the other was forest area: open forest, eight main tree species, bamboo and shadow (Figure 5). The open forest was defined as the zones composed of nursery, shrubland or sparse trees. The shadow class mainly formed from the northern regions neighboring mountain ridges, where the abrupt slope and trees with fallen leaves with small sizes and low density led to the shaded and darker areas.

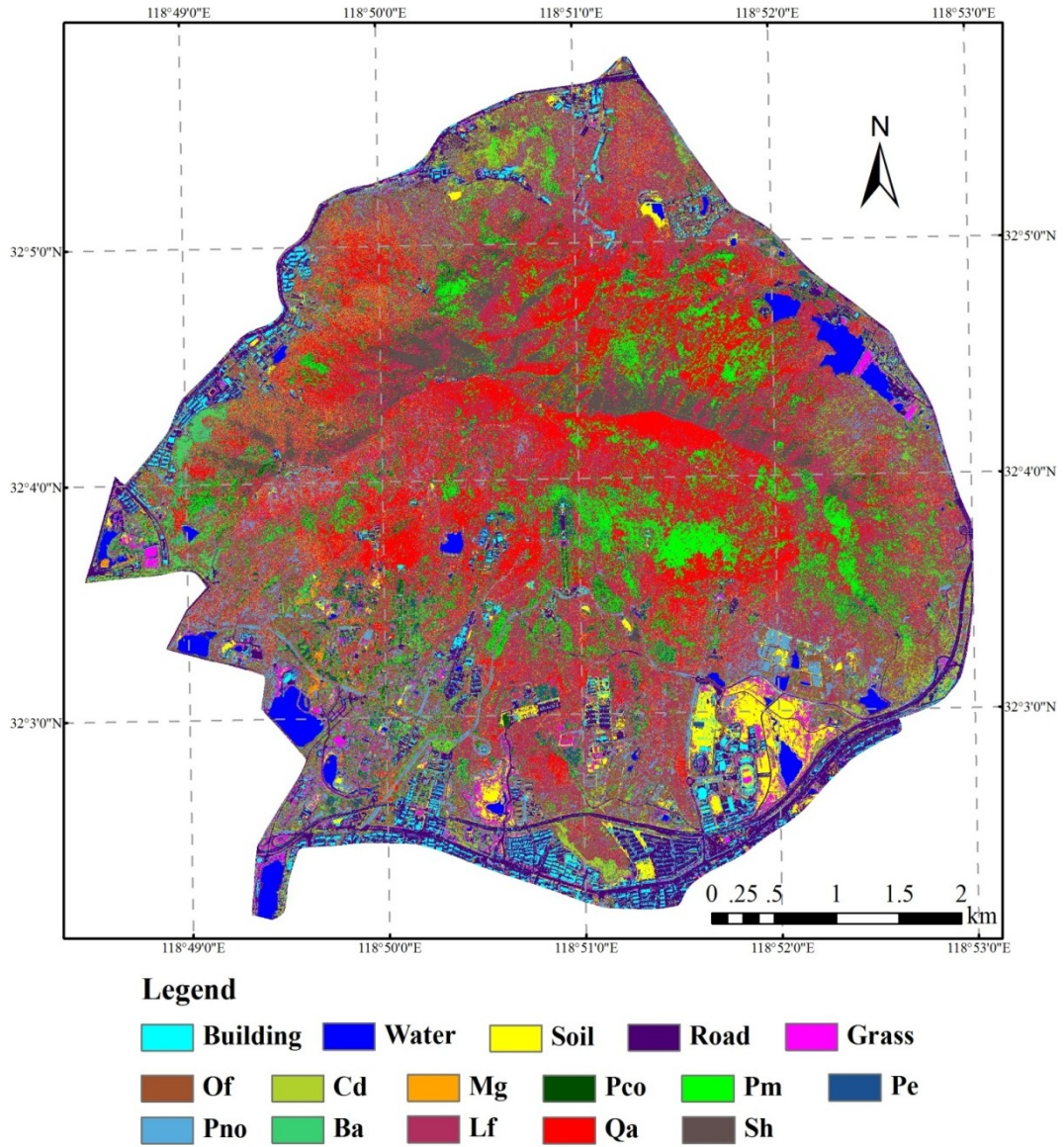


**Figure 5.** Distribution of 16 classes classified by MultiSpec Win32 for eight multispectral bands. Of: open forest; Cd: *Cedrus deodara*; Mg: *Metasequoia glyptostroboides*; Pco: *Platycladus orientalis*; Pm: *Pinus massoniana*; Pe: *Pinus elliottii*; Pno: *Platanus orientalis*; Ba: bamboo; Lf: *Liquidambar formosana*; Qa: *Quercus acutissima*; Sh: shadow.



In the process of classification, 282 training areas with a total number of 194,117 pixels ( $4.0 \text{ m}^2/\text{pixel}$ ) were created for the 16 classes (for a detailed number of each class, see Table 2). Using the mean digital number (DN, representing the reflectance of the objects on sunshine) of the test pixels of each class for all multi-color bands, a straight-line map was used to compare the spectral characteristics of the different classes (Figure 6). Band DNs for the spectral values were highest for Green (ranging  $0.51\text{--}0.58 \mu\text{m}$ ), either in non-forested areas or forest areas, and lowest for Red ( $0.63\text{--}0.69 \mu\text{m}$ ) for most of the classes. The mean DNs of the Blue band ( $0.45\text{--}0.51 \mu\text{m}$ ) for most of the classes in non-forest regions were higher than those of other bands. However, most tree species had nearly equal spectral values in the Blue, Red-Edge, NIR1 and NIR2 bands. In addition, the water and shadow classes had similar trend lines, with the lowest DN value in band NIR2. The DN values of broad-leaved trees were greater than those of conifers, and *Platanus orientalis* was the highest for most bands. Although the DNs of most bands differed markedly between broad-leaved and coniferous trees, little discrepancy was found in some conifers, such as *Platycladus orientalis* and *Pinus massoniana*, which was disadvantageous for classifying them. Additionally, the statistical test of separability using the Transformed Divergence

method indicated a good separability between most of the classes (Table 3).

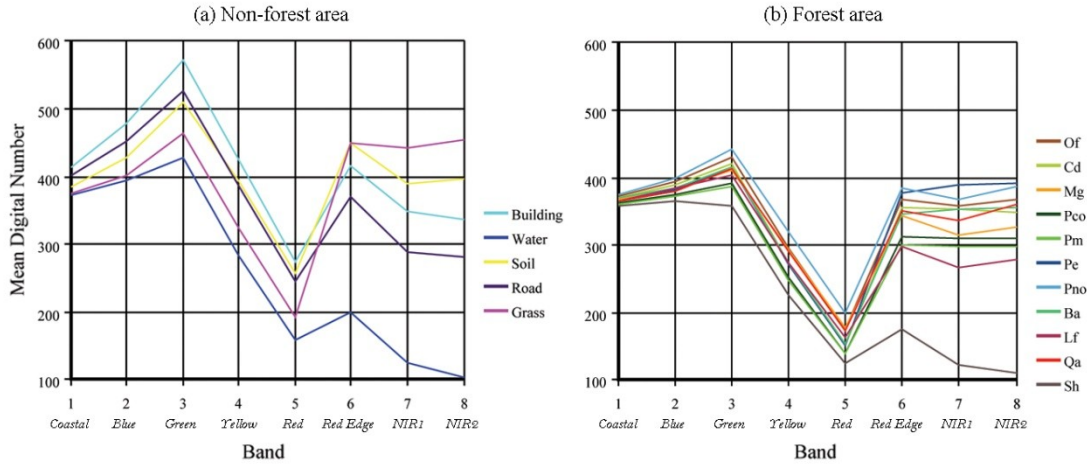


**Figure 6.** Comparison of the mean digital number (DN) values of different classes using a line chart. The abbreviations are the same as in Figure 5.

The confusion matrix for the test areas for the 16 classes using WorldView-2 imagery with eight bands by MultiSpec Win32 is shown in Table 2. Non-forested areas are typically classified with high accuracy, with the exception of road type, because the spectral signatures of many road pixels are similar to those of buildings and were misclassified as buildings. Regarding tree species, the confusion matrix indicated the dominant species in the canopy layer, *Pinus massoniana* and *Quercus acutissima*, which were classified at 80.6% and 93.0%, respectively. However, the accuracy of another dominant species, *Liquidambar formosana*, was relatively low at 67.5%,

because it was in the subdominant layer and many individuals were covered by *Quercus acutissima*. By contrast, some species were misclassified with low accuracy. For example, *Platycladus orientalis* and *Platanus orientalis* were misclassified into *Pinus massoniana* and open forest, respectively, mainly due to their low proportion and because most of the forest in the study area was composed of uneven-aged mixed forest with a complex spatial structure.

MultiSpec Win32 is the common software for land cover and forest classification and has been used for forest studies worldwide free of charge. ERDAS Imagine is the comprehensive software available for processing remote sensing images, such as geometric and ortho correction, image enhancement and classification and integration with GIS (Geographic Information System). In this study, using the same training areas, a supervised classification on the same WorldView-2 image with eight multispectral bands was completed by ERDAS Imagine 8.6. Although the classified accuracies of *Cedrus deodara* and *Metasequoia glyptostroboides* obtained by ERDAS were higher than those determined by MultiSpec, most of the class accuracies determined by MultiSpec were better than those determined by ERDAS, with an average increment of 1.8% for the 16 classes (Figure 7). Therefore, we selected the results classified by MultiSpec Win32

for the output thematic map and to conduct the subsequent study. In addition, to clarify whether the four additional bands of WorldView-2 could improve the classification accuracy significantly compared to the four standard bands, the object image with the four standard bands (Blue, Green, Red, and NIR1) was classified again using the same test pixels by MultiSpec Win32. The results indicated that the classified accuracies of the 16 classes obtained by using all of the multispectral bands were higher than those obtained by using only the four standard bands. The increments ranged from 0.1% for the water class to 17.0% for *Metasequoia glyptostroboides*, with an average value of 4.8% for the 16 classes (Figure 7).

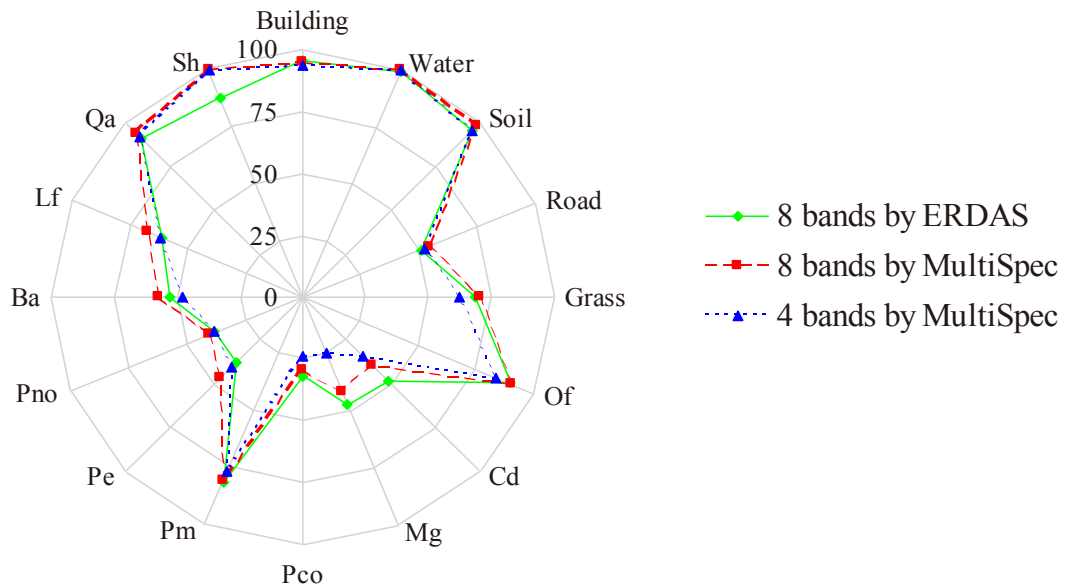


**Figure 7.** Spider chart representing the user accuracies for different classification approaches. The abbreviations are the same as in Figure 5.

**Table 2.** Confusion matrix for the 16 classes using WorldView-2 imagery with eight bands by MultiSpec Win32.

Class Name*	Class NO.	1	2	3	4	5	6	7	8	9	10	11	12	13	14	15	16	Number Samples	Producer's Accuracy (%)
Building	1	12,819	49	103	6,930	3	36	10	2	0	0	1	1	2	3	6	0	22,966	55.8
Water	2	4	81,143	0	5	0	0	0	0	611	8	82	0	5	0	0	0	83,059	97.7
Soil	3	185	0	11,067	23	17	20	0	0	0	0	0	4	0	0	0	0	11,774	94.0
Road	4	424	6	38	8,299	2	2	0	0	0	0	0	0	0	0	0	0	9,037	91.8
Grass	5	4	0	6	0	2,739	237	52	6	0	0	86	192	33	9	106	0	3,607	75.9
Of	6	5	5	170	14	965	8,688	526	96	145	159	708	2,883	1,140	1,580	120	0	17,875	48.6
Cd	7	0	0	0	1	5	13	1,132	0	80	31	27	0	118	3	0	0	1,419	79.8
Mg	8	0	1	0	0	0	4	0	1,215	0	5	0	49	4	132	93	0	1,543	78.7
Pco	9	0	2	0	0	3	6	33	2	829	300	103	0	48	9	3	0	1,352	61.3
Pm	10	0	8	0	0	3	55	445	3	664	4,306	144	1	89	73	40	15	5,902	73.0
Pe	11	1	0	0	0	68	50	441	7	289	190	1,144	0	267	7	33	0	2,570	44.5
Pno	12	1	0	5	2	27	102	0	116	0	0	0	2,583	1	164	52	0	3,099	83.3
Ba	13	0	1	0	0	30	87	239	4	135	107	152	0	2,365	11	29	0	3,178	74.4
Lf	14	10	2	0	0	2	233	0	415	12	86	1	141	27	6,427	136	24	7,694	83.5
Qa	15	8	0	0	0	37	137	0	1,076	30	68	37	548	29	1061	8,265	0	11,662	70.9
Sh	16	0	10	0	0	0	0	0	0	4	84	0	0	0	39	2	7,033	7,380	95.3
Total		13,461	81,227	11,389	15,274	3,901	9,670	2,878	2,942	2,799	5,344	2,485	6,402	4,128	9,518	8,885	7,072	194,117	
User's Accuracy (%)		95.2	99.9	97.2	54.3	70.2	89.8	39.3	41.3	29.6	80.6	46.0	40.3	57.3	67.5	93.0	99.4		

Notes: Overall Class Performance (160054/194117) = 82.5%; Kappa Statistic (X100) = 77.9%; Kappa Variance = 0.000001. \* Of: open forest; Cd: *Cedrus deodara*; Mg: *Metasequoia glyptostroboides*; Pco: *Platycladus orientalis*; Pm: *Pinus massoniana*; Pe: *Pinus elliotii*; Pno: *Platanus orientalis*; Ba: bamboo; Lf: *Liquidambar formosana*; Qa: *Quercus acutissima*; Sh: shadow.

**Table 3.** The statistical test of the Signature Separability for the 16 classes using the Transformed Divergence method.

Signature Name*	Class NO.	1	2	3	4	5	6	7	8	9	10	11	12	13	14	15	16
Building	1	0	2,000	2,000	2,000	2,000	2,000	2,000	2,000	2,000	2,000	2,000	2,000	2,000	2,000	2,000	2,000
Water	2	2,000	0	2,000	2,000	2,000	2,000	2,000	2,000	2,000	2,000	2,000	2,000	2,000	2,000	2,000	2,000
Soil	3	2,000	2,000	0	1,998	1,974	1,988	2,000	2,000	2,000	2,000	2,000	1,991	2,000	2,000	1,999	2,000
Road	4	2,000	2,000	1,998	0	2,000	2,000	2,000	2,000	2,000	2,000	2,000	2,000	2,000	2,000	2,000	2,000
Grass	5	2,000	2,000	1,974	2,000	0	1,663	1,996	1,997	2,000	1,999	1,911	1,953	1,972	1,998	1,924	2,000
Of	6	2,000	2,000	1,988	2,000	1,663	0	1,943	1,870	1,994	1,986	1,776	1,619	1,775	1,775	1,810	2,000
Cd	7	2,000	2,000	2,000	2,000	1,996	1,943	0	2,000	1,702	1,566	1,364	2,000	1,102	1,990	1,997	2,000
Mg	8	2,000	2,000	2,000	2,000	1,997	1,870	2,000	0	2,000	1,999	1,999	1,643	1,997	1,410	1,430	2,000
Pco	9	2,000	2,000	2,000	2,000	2,000	1,994	1,702	2,000	0	902	1,346	2,000	1,518	1,985	1,998	2,000
Pm	10	2,000	2,000	2,000	2,000	1,999	1,986	1,566	1,999	902	0	1,543	2,000	1,599	1,946	1,994	2,000
Pe	11	2,000	2,000	2,000	2,000	1,911	1,776	1,364	1,999	1,346	1,543	0	2,000	968	1,991	1,977	2,000
Pno	12	2,000	2,000	1,991	2,000	1,953	1,619	2,000	1,643	2,000	2,000	2,000	0	2,000	1,629	1,633	2,000
Ba	13	2,000	2,000	2,000	2,000	1,972	1,775	1,102	1,997	1,518	1,599	968	2,000	0	1,971	1,984	2,000
Lf	14	2,000	2,000	2,000	2,000	1,998	1,775	1,990	1,410	1,985	1,946	1,991	1,629	1,971	0	1,730	2,000
Qa	15	2,000	2,000	1,999	2,000	1,924	1,810	1,997	1,430	1,998	1,994	1,977	1,633	1,984	1,730	0	2,000
Sh	16	2,000	2,000	2,000	2,000	2,000	2,000	2,000	2,000	2,000	2,000	2,000	2,000	2,000	2,000	2,000	0

Notes: Distance measure: Transformed Divergence; using layers: 1, 2, 3, 4, 5, 6, 7, 8; best average separability: 1,906.84; combination: 1, 2, 3, 4, 5, 6, 7, 8.

\* Of: open forest; Cd: *Cedrus deodara*; Mg: *Metasequoia ghyptostroboides*; Pco: *Platycladus orientalis*; Pm: *Pinus massoniana*; Pe: *Pinus elliotii*; Pno: *Platanus orientalis*; Ba: bamboo; Lf: *Liquidambar formosana*; Qa: *Quercus acutissima*; Sh: shadow.

### **3.2.3 Object-Based Supervised Classification of Tree Species**

For the purpose of avoiding the “mixed pixels” effect of the pixel-based classification, a crown-based supervised classification was performed on the forest areas with eight multispectral bands in PCI Geomatica v9.1 with the ITC Suite. As a consequence, with a magnified area, the crown-based thematic map of tree species was generated and documented in Figure 8 by overlaying the non-forest classes produced by the pixel-based classification. When the object-based classification was completed, a total number of 500 random sample trees were used for the accuracy assessment. The 500 sample points were generated by the stratified random rule, and the minimum number of each species was 30. Then, all sample trees were assigned their reference classes based on forest inventory data and other additional information, including photos linked in Google Earth and existing thematic maps. Finally, an accuracy report was generated and displayed in Table 4. The results indicated that the ITC-based classification was much better than the pixel-based classification for the forested area, although the overall accuracy of the latter was slightly higher than that of the former, because the overall accuracy for the pixel-based classification included the non-forested classes, such as water, building and soil, with very good classified results. The



improvements of the object- to pixel-based classification ranged from −1.6% for the open forest class to 34.3% for *Metasequoia glyptostroboides*, with an average value of 20.3% for the 10 classes.

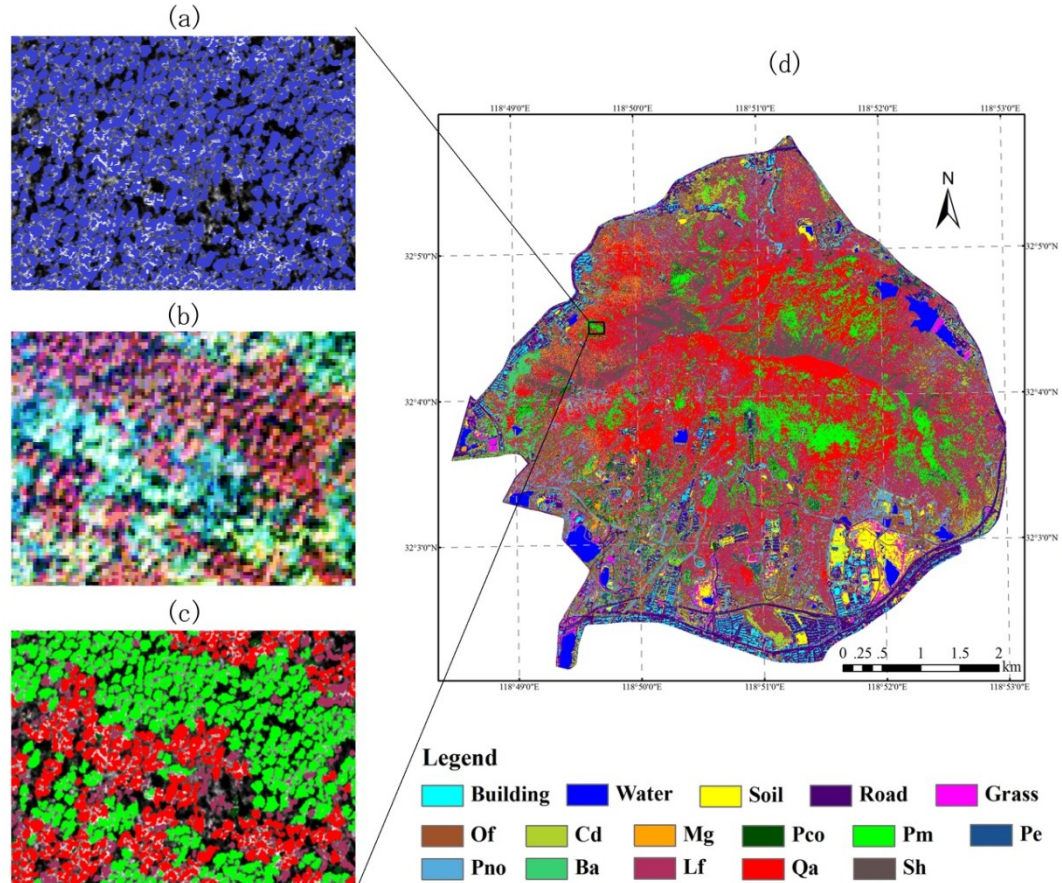


**Figure 8.** Distribution of tree species classified by the crown-based approach for eight multispectral bands. (a) the magnified area displayed by delineated tree crowns overlaying the panchromatic band; (b) the magnified area displayed by R: G: B = 7(NIR1): 5(Red): 2(Blue); (c) the magnified area displayed by object-based classified tree crowns overlaying the panchromatic band; (d) the crown-based classification map of tree species at Purple Mountain by overlaying the non-forested classes. The abbreviations are the same as in Figure 5.



**Table 4.** Error matrix for the 10 classes classified by the ITC-based classification approach.

Class Name *	Of	Cd	Mg	Pco	Pm	Pe	Pno	Ba	Lf	Qa	Number Samples	Producer's Accuracy (%)
Of	<b>30</b>	0	1	0	0	0	1	0	1	0	33	90.9
Cd	0	<b>27</b>	1	2	2	2	1	2	0	0	37	73.0
Mg	1	0	<b>34</b>	0	0	0	5	0	5	0	45	75.6
Pco	0	5	0	<b>19</b>	1	4	0	1	0	0	30	63.3
Pm	0	1	0	2	<b>57</b>	2	0	2	0	1	65	87.7
Pe	0	1	1	3	3	<b>33</b>	0	1	0	0	42	78.6
Pno	2	2	4	0	0	0	<b>34</b>	0	8	0	50	68.0
Ba	0	2	0	1	2	2	1	<b>22</b>	0	1	31	71.0
Lf	1	1	4	3	1	0	4	0	<b>71</b>	2	87	81.6
Qa	0	0	0	1	0	0	0	0	1	<b>78</b>	80	97.5
Total	34	39	45	31	66	43	46	28	86	82	500	
User's Accuracy (%)	88.2	69.2	75.6	61.3	86.4	76.7	73.9	78.6	82.6	95.1		

Notes: Overall classification accuracy (405/500) = 81.0%; Kappa Statistic (X100) = 76.3%; Kappa Variance = 0.000001. \* Of: open forest; Cd: *Cedrus deodara*; Mg: *Metasequoia glyptostroboides*; Pco: *Platycladus orientalis*; Pm: *Pinus massoniana*; Pe: *Pinus elliottii*; Pno: *Platanus orientalis*; Ba: bamboo; Lf: *Liquidambar formosana*; Qa: *Quercus acutissima*.

### 3.2.4 Counting Trees of Different Species in the Study Area

In this study, using an overlay from the extraction function in ArcGIS v9.2, all tree tops extracted by the ITC method were annotated with species attributes from the thematic map classified by the crown-based approach using the WorldView-2 image with eight multispectral bands. The total number of trees of different species at Purple Mountain was counted using the summarize function in ArcGIS (Figure 9).

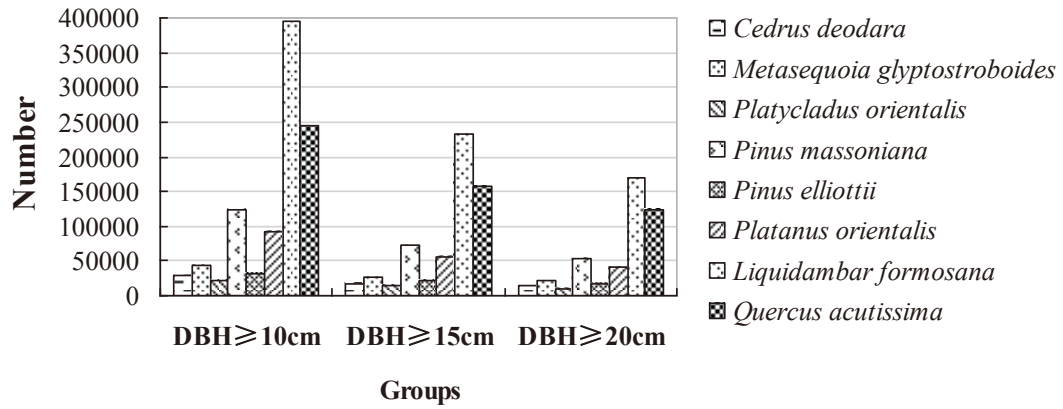


**Figure 9.** Tree count of different species at Purple Mountain.

The count indicated that the density of the forest in the study area was mainly dominated by *Liquidambar formosana* and *Quercus acutissima* in three layers. *Pinus massoniana* was the dominant species compared with other coniferous species. The results were in accordance with forest inventory data.

### **3.3 Discussions**

In modern forest management, pure stands are replaced by heterogeneous, mixed stands. Therefore, spatially detailed forest information over large areas is of great importance. The traditional forest inventory method using sample plotting is nearly impossible to accomplish due to its low accuracy and scale limitation. Therefore, enhanced methods are required to obtain spatially explicit information on tree species composition and distribution patterns [2]. This study attempted to acquire forest resource information at the individual tree level by using remote sensing techniques on a large scale.

Tree tops were first interpreted by the ITC method. This approach is very effective for extracting tree tops of even-aged single forests using a filter of a moving window with a single size. For a large forest composed of uneven-aged stands with different tree crown sizes, the homogeneity function of the ITC Suite can be used to separate young tree areas from mature forests [1,24]; the tops of small and large-sized trees can then be interpreted by using filters with different moving window sizes on small and large tree areas, respectively. However, because cutting has been forbidden since the 1980s, there are few stands of a single species or size distributed at Purple Mountain today, and most forests have a complex spatial structure that is difficult to

interpret using a filter with a fixed moving window. Therefore, the forests in the study area were divided into three groups: trees  $\geq 10$  cm DBH,  $\geq 15$  cm DBH and  $\geq 20$  cm DBH. The tree tops in the three groups were then extracted by using filters with a moving window of  $3 \times 3$  pixels ( $1.5 \times 1.5$  m),  $5 \times 5$  pixels ( $2.5 \times 2.5$  m) and  $7 \times 7$  pixels ( $3.5 \times 3.5$  m), respectively, which, in theory, should extract trees with crown diameters of greater than 1.5 m, 2.5 m and 3.5 m, respectively.

Although the tree crowns were delineated using the individual tree crown approach based on the DBH knowledge of the 90 plots, the interpreted results of the tree crowns and tree tops are independent of the DBH information. Consequently, this approach can also be used to delineate the trees in the areas with no DBH information. In the even-aged forests, the trees can be easily mapped using a fixed moving window, because of the approximately same crown sizes. Additionally, the trees in the areas having a mixed DBH class can be delineated using a similar method as our study. The filter window size(s) can be determined by roughly estimating the tree crown sizes combining the spatial resolution of the remotely sensed data. When the tree crown delineations were completed, the DBH inversion of the interpreted trees may be true using the correlations between the tree crowns and DBHs of observed trees. This topic will be verified in the

next study using the 10 large-sized plots investigated in May 2012, in which the detailed position information of the individual trees was recorded in addition to the crown sizes.

In addition, we selected the entire mountain, which has an area of approximately 30 km<sup>2</sup>, as the research study area and established 90 plots distributed in different forest types to test accuracy. Due to time limitations and the large number of plots, we only measured DBH and the height of the trees  $\geq 5$  cm DBH and did not include the coordinates of every tree. The center of every plot was noted by GPS (Garmin MAP 60CS, accuracy  $\pm 3$  m) and as sample points. We considered that the observed stem density in sample points could represent the condition of forest stands around sample points. For extracted trees, the densities in every central point were calculated by the buffer function in ArcGIS v9.2. Finally, we verified the agreement of the observed and estimated tree densities in every central point and calculated the interpreted accuracy. We plan to verify the agreement of the observed and estimated trees individually by creating some large size plots in our next study.

WorldView-2 was expected to have great potential for forest studies, because the satellite has higher spatial resolution and can provide more abundant multispectral information compared with traditional

sensors. The findings of our study suggested that the four new bands (Coastal, Yellow, Red-Edge and NIR2) of the WorldView-2 have a positive effect on the species classification. The classified accuracies of the 16 classes obtained using all of the eight multispectral bands were higher than those obtained using only the four standard bands. The improvements ranged from 0.1% for the water class to 17.0% for *Metasequoia glyptostroboides*, with an average value of 4.8% for the 16 classes.

At Purple Mountain, most stands have a complex spatial structure, with more than two layers and many regenerated species that differ from those of the canopy trees distributed in understories and the gaps between tree crowns, complicating the identification of individual tree crowns and species. The broad-leaved species, *Quercus acutissima*, the most dominant species in the canopy layer, was classified with good user accuracy. In the late 1970s, many large *Pinus massoniana* trees, the dominant coniferous species, were damaged by pine wilt disease. Broad-leaved trees, including *Quercus acutissima* and *Pistacia chinensis*, successfully invaded the gaps and had good growth. As a result, *Pinus massoniana* has been classified with an accuracy of 80.6%. Another dominant species, *Liquidambar formosana*, had relatively lower classification performance, because it was in a

subdominant layer and many individuals were covered by *Quercus acutissima*. However, some species were misclassified by the pixel-based classification with low accuracy, due mainly to their low proportion. The season in which the images were acquired also had negative effects on tree species classification in some cases. In winter, the leaves of some deciduous tree species had fallen, and some trees were turning yellow or dying off, which would lead to a change in forest reflectance in the spectrum. Therefore, it is essential to classify forests by combining the data acquired in summer with those acquired in winter using other classification methods in future studies.

For the classification analysis of images with very high spatial resolution, object-based approaches are superior over pixel-based approaches when the pixel size is significantly smaller than the average size of the objects of interest [83,84]. Immitzer *et al* also found that by classifying objects instead of pixels, the user accuracies could increase significantly for most tree species in a forest study of a temperate zone [2], and the positive impact was higher for conifers than broadleaved trees. Additionally, there may be a “mixed pixels” issue in the pixel-based classification, *i.e.*, the pixels within the tree crowns of large sizes might be classified into two or more different classes. The ITC-based classifier presented by Gougeon [28] can

overcome this “mixed pixels” problem, which classifies the pixels within the single crown into the same species by comparing the signature of each tree crown with the ITC-based signatures of the various species using the Maximum-Likelihood algorithm. The results of the present study indicated that the crown-based classification improves the classified accuracy of both dominant species and smaller classes. This result is because the ITC-based classification cannot only avoid the pixels within tree crowns being classified into non-forested classes, such as building and road, but it can also mitigate the effect of the shadows between tree crowns on species classification. Therefore, the findings from this study lead to the recommendation of using the ITC-based instead of the pixel-based classification approach in classifying highly mixed forests.

Generally, the DN values of forestland in NIR bands were higher than those in other bands, such as Blue, Green and Red [85–87]. However, we determined that the band with the highest DN values was Green (0.51–0.58  $\mu\text{m}$ ) for all of the species rather than the NIRs in this study, and the spectral values of forest areas in NIR bands were much lower than those of other published studies [2,18,88]. It is likely that the reflectances of forestland on NIRs were mainly affected by the structure of tree cells, and the image used in this study was taken in



December 2011, when the low temperature in the study area inhibited the growth of trees and induced dormancy, thus resulting in changes in cell structure, such as a decrease in water content. The details of the influencing mechanisms require further study.

All of the extracted tree tops were annotated with species attributes from the thematic map established by the ITC-based supervised classifications, and the numbers of trees of different species were counted in this study. We studied how to interpret other parameters of forest resources, such as tree height, DBH and volume at the individual level, automatically by remote sensing. An available method to measure tree height using DSM (Digital Surface Model) minus DTM (Digital Terrain Model), which might be extracted from airborne LiDAR data, was reported by Katoh [89]. However, it is very difficult to interpret DBH information directly using satellite or airborne imagery. It has become possible to measure the DBHs of individual trees by regression models of DBH as the dependent variable and tree height as the independent variable and combining the location information of the extracted tree tops. Moreover, with the development of computer technology, some software, such as E3De v3.1, can automatically create three-dimensional models of individual trees using airborne LiDAR data with high point-densities, potentially

enabling the interpretation of DBH. However, its usefulness needs to be verified in future studies.

### 3.4 Conclusions

The present study has measured the forest resources at Purple Mountain at the individual tree level using the WorldView-2 data by combining GPS, RS, and Geographic Information System (GIS) technologies. The tree tops were first interpreted by the ITC approach. Second, the study area was classified into two types of land cover with a total of 16 classes using the pixel-based classification. The results of our study suggested that the four new bands (Coastal, Yellow, Red-Edge and NIR2) of the WorldView-2 have a positive effect on the species classification. To overcome the “mixed pixels” problem of the pixel-based approach, a crown-based supervised classification was used for generating a thematic map of tree species. The findings from this study lead to the recommendation of using the crown-based instead of the pixel-based classification approach in classifying mixed forests. Finally, all tree tops were annotated with the species attributes from the thematic map, and a tree count of different species indicated that the forest of Purple Mountain is mainly dominated by *Quercus acutissima*, *Liquidambar formosana* and *Pinus massoniana*.

## Chapter 4 Estimating Forest Aboveground Biomass

### 4.1 Data Analysis Method

The research flow chart in Figure 10 provides an overview of the methods.

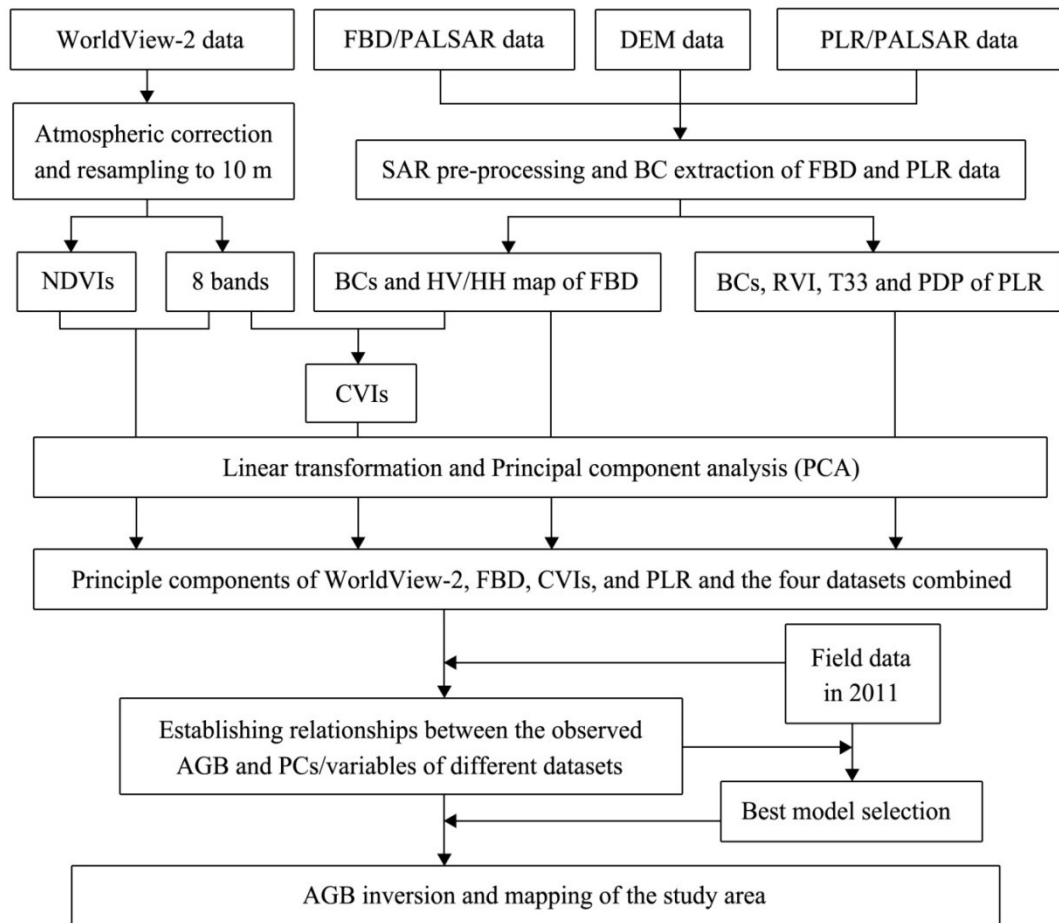


**Figure 10.** Research flow chart. DEM: Digital Elevation Model; BC: Backscattering Coefficient; NDVI: Normalized Difference Vegetation Index; RVI: Radar Vegetation Index; PDP: Polarimetric Decomposition Parameters; CVI: Combined Volume Index.

#### 4.1.1 Field Data

In our investigation, the aboveground biomass ranged from approximately 25 Mg/ha for regenerating stands to 342 Mg/ha for mature, highly stocked stands. The observed dataset ( $n = 90$ ) was randomly split into 70% and 30% portions for a calibration dataset ( $n = 63$ ) and a validation independent dataset ( $n = 27$ ), respectively. Because the number of surveyed plots was limited, obtaining a similar AGB distribution in both datasets was also considered when making the division. Consequently, the calibration dataset, which had a biomass value of  $140.78 \pm 57.68$  Mg/ha (average  $\pm$  standard deviation), was used to train the prediction models, while the validation dataset, which had a biomass value of  $142.90 \pm 71.79$  Mg/ha, was separately used to test the quality and reliability of the prediction models.

Generally, the AGB of a forest can be accurately estimated by summing the biomass of all the individual trees in the plot, which can be calculated using allometric equations based on the DBH and the height of the trees [44,59,90]. However, no allometric equations are available for the study area. Therefore, we used the method presented by Fang *et al.* [91] to estimate the AGB of the 90 plots. First, the volumes of all individual trees were calculated using a volume table

based on the DBH and height of the trees. Next, the total volumes in each plot were summed. Then, the biomass of each plot was estimated by the regression between biomass ( $B$ ) and total volume ( $V$ ), expressed as:

$$B = aV + b \quad (2)$$

where  $a$  and  $b$  are coefficients that vary with forest types and have been listed in [91] for different forests.

#### **4.1.2 PALSAR Pre-Processing**

The pre-processing was completed using the ENVI SARscape software. To reduce speckle and generate square pixels, the two PALSAR datasets were first multi-looked using factors of 1 and 4 for FBD image and factors of 1 and 7 for PLR data, respectively, for the range and azimuth directions. The datasets were then calibrated to obtain SAR backscattering images. The updated calibration factor provided by JAXA was used for absolute calibration [92]. In addition, the images were speckle filtered using the Lee Refined Filter during processing.

SAR data are acquired in a side-looking geometry, which leads to a number of distortions in the imagery. Terrain correction removes these geometry-induced distortions by making use of a digital elevation model (DEM). The process of terrain correction can be divided into

two separate parts: geometric terrain correction and radiometric terrain correction. Geometric terrain correction adjusts the individual pixels of an amplitude image to ensure their proper location (*i.e.*, it places the ridgelines and valleys where they geometrically belong). Radiometric terrain correction adjusts the brightness of the pixels with respect to the observation geometry, as defined by the incidence angle as well as the slope and aspect of the local terrain. Castel *et al.* [49] reported that areas of sloped terrain can induce 2–7 dB dispersion on radar backscattering. Therefore, the area having slopes facing the radar sensor without radiometric normalization would have higher backscatter coefficients than flatter areas, which is a problem when assessing properties of backscatter [67]. Hence, these topographic effects were addressed through radiometric normalization of the backscatter coefficient. To obtain a better representation of the backscatter coefficient for distributed targets (*i.e.*, the forest areas), a conversion from sigma nought to gamma nought was applied [67,93]. In this study, using the DEM data with a resolution of 30 m downloaded from the ASTER GDEM website, the two images were geometrically and radiometrically terrain corrected and geo-coded to the zone 50 north of the UTM projection and were outputted as GeoTIFF maps with a pixel size of 10 m.

### **4.1.3 Polarimetry and Other Parameters of the PLR/PALSAR Data**

In addition to backscatter intensities, a target decomposition technique was applied to the PLR data to obtain polarimetric products. Polarimetric decomposition provides information about the scattering properties from the targets [51,94–97]. The relationships between a feature's physical properties and its polarimetric behavior can be interpreted by examining the underlying scattering mechanisms; the scattering process can change between forest stands of different structural types and ages [67]. In our study, the entropy (H), alpha ( $\alpha$ ) angle, and anisotropy (A) decomposition parameters and the combination of  $H(1-A)$  were generated using the PolSARpro v4.2 software provided by the European Space Agency (ESA). For detailed information about these decomposition parameters, please see previous studies [51,95,97,98].

The RVI (radar vegetation index) derived from the PLR/PALSAR data can also be used to analyze the scattering from the vegetated area [99]. Woody vegetation has high cross-polarization components and high RVI values [97]. The RVI is derived from the radar backscattering coefficient ( $\gamma^\circ$ ) of the HH, HV, and VV polarizations [100].



$$RVI = 8\gamma_{HV}^0 / (\gamma_{HH}^0 + \gamma_{VV}^0 + 2\gamma_{HV}^0) \quad (3)$$

In addition, the PolSARPro works with two different domains. One domain is the coherency matrix **T3**, which is derived from the Pauli scattering vector **k**. The other is the covariance matrix **C3**, which is based on the lexicographic scattering vector **Ω**. Often, the polarimetric data in the PolSARPro are stored as a **T3** matrix because the diagonal matrix elements allow a physical interpretation. The T11 element represents single-bounce scattering (e.g., waters and roads), the T22 element shows the feature of double-bounce scattering (e.g., buildings), and the T33 element indicates the properties of volume scattering (e.g., forest vegetations). Therefore, the T33 map was also used to retrieve the forest AGB in our study.

#### 4.1.4 Calculating NDVIs and CVIs (Combined Volume Index)

NDVI was selected because this vegetation index is commonly used to estimate biomass [101–104]. As shown in Figure 10, the atmospherically corrected image was used to generate the NDVI maps. To match the pixel size of the backscatter coefficient maps, the optical image had to be resampled to a spatial resolution of 10 m. Then, a standard NDVI map was produced using band 7 (NIR1) and band 5 (Red) according to the following formula:

$$NDVI_{7-5} = (R_{NIR1} - R_{Red}) / (R_{NIR1} + R_{Red}) \quad (4)$$

where  $R$  is the reflectance value. The other 3 developed NDVIs,  $NDVI_{8-5}$ ,  $NDVI_{7-6}$ , and  $NDVI_{8-6}$ , were also calculated by the same method using band 8 (NIR2) and band 5 (Red), band 7 (NIR1) and band 6 (Red-Edge), and band 8 (NIR2) and band 6 (Red-Edge), respectively.

In addition, as described in the Introduction section, optical images can provide the most information about tree crowns, such as LAI (leaf area index) and crown density, while SAR data measure forests based on backscattering from the branches and stems of the trees. Accordingly, the synergistic use of optical and SAR sensors was expected to have great potential for biomass estimation. Moreover, we determined that the observed AGB was positively correlated with the backscatter coefficient of the HV/FBD data by a moderate  $R^2$  (coefficient of determination) value and was negatively correlated with bands 1 to 6 of the WorldView-2 image fitted by a compound function expressed by the Equation (7). In our study, the trend line of this function was similar to the exponential function in the correlation with the observed biomass but had greater significance than the latter in the model test (Table 5). Therefore, a new parameter denoted the combined volume index (CVI) because of the good linear relationships between the CVIs and plot volume was generated by

combining the HV backscattering of the FBD data and the eight multispectral bands of WorldView-2 image in this study. The CVI can be expressed as follows:

$$CVI_i = (\gamma_{HV}^0 - R_i) / (\gamma_{HV}^0 + R_i) \quad (5)$$

where  $\gamma_{HV}^0$  is the backscatter coefficient of the HV/FBD data and  $R_i$  is the reflectance value of the WorldView-2 bands (1 to 8). Before calculating CVIs, the backscattering and reflectance images were resampled to the data type of unsigned 8 bit integers.

#### **4.1.5 Establishing the Relationships between the Observed AGB and Parameters**

In Table 5, a total of 33 variables that may be correlated with the forest biomass were first fitted with the observed AGB using the following 8 functions (Equations (6) to (13)). Then, the best-fitting equation for each variable (except for bands 7 and 8 of WorldView-2 due to their insufficient correlation with the AGB), as judged by the  $R^2$  value and significance, was used for the linear transformations. The linear-transformed variables were then used to perform the subsequent principal component analysis (PCA). Finally, the results of the PCA were used to model the biomass by multivariate stepwise regression. The coefficients ( $b_0$ ,  $b_1$ ) of the best-fitted model for each variable are listed in Table 5.

(a) Linear function:

$$y = b_0 + b_1 x \quad (6)$$

(b) Compound function:

$$y = b_0 \times b_1^x \quad (7)$$

(c) Growth function:

$$y = e^{(b_0 + b_1 x)} \quad (8)$$

(d) Logarithmic function:

$$y = b_0 + b_1 \ln x \quad (9)$$

(e) *S* function:

$$y = e^{(b_0 + b_1 / x)} \quad (10)$$

(f) Exponential function:

$$y = b_0 e^{b_1 x} \quad (11)$$

(g) Inverse function:

$$y = b_0 + b_1 / x \quad (12)$$

(h) Power function:

$$y = b_0 x^{b_1} \quad (13)$$

As shown in Table 5, most of the fitted equations are curvilinear models, indicating that implementing linear transformations for these parameters is essential before performing the multivariate linear regression (MLR). In addition, it is easily deduced that Equations (14),

(15), and (16) are equivalent. Thus, the maps of these parameters fitted by curvilinear models had to be operated using the formula listed in the last column of Table 5. Moreover, because some parameters were generated from other parameters, a multicollinearity problem will remain if these parameters are directly used as independent variables to perform the multivariate stepwise regression. Consequently, on the basis of their sources, these parameters were divided into five datasets: A (FBD/ALOS), B (PLR/ALOS), C (WorldView-2), D (CVIs), and E (all 31 parameters) (Table 5). A PCA was then performed for each dataset. As a result, 2, 5, 4, 3, and 7 principal components (PC) were extracted from the dataset A to E, with cumulative variances of 99.99%, 98.31%, 99.09%, 99.56%, and 92.03%, respectively. Normality tests showed that these PCs are normally distributed. Finally, the relationships between the forest AGB and the above principal components were established using a stepwise linear regression approach.

$$Y(X) = m_1[a_1f(x_1) + b_1] + m_2[a_2f(x_2) + b_2] + \cdots + m_n[a_nf(x_n) + b_n] \quad (14)$$

$$Y(X) = m_1a_1f(x_1) + m_2a_2f(x_2) + \cdots + m_na_nf(x_n) + m_1b_1 + m_2b_2 + \cdots + m_nb_n \quad (15)$$

$$Y(X) = M_1f(x_1) + M_2f(x_2) + \cdots + M_nf(x_n) + N \quad (16)$$

where  $m_n$ ,  $a_n$ ,  $b_n$ ,  $M_n$ , and  $N$  are constants.

**Table 5.** Regression models between the observed aboveground biomass (AGB) as the dependent variable and the parameters derived from different RS (remote sensing) sources as the independent variables.

RS Sources	Parameter	Best Equation	$b_0$	$b_1$	$R^2$ (sig.)	Linear Transform
FBD/ALOS (dataset A)	F-HH	Growth	6.095	0.127	0.43 *	Exp( $b_1x$ )
	F-HV	Growth	6.333	0.104	0.51 **	Exp( $b_1x$ )
	F-HV/HH	Logarithmic	110.087	82.843	0.24 *	ln( $x$ )
PLR/ALOS (dataset B)	P-HH	Inverse	127.077	-78.192	0.41 *	$b_1/x$
	P-HV	Compound	162.352	1.018	0.36 *	$b_1^x$
	P-VH	Linear	174.712	2.447	0.22 <sup>ns</sup>	$x$
	P-VV	Linear	156.054	1.902	0.19 <sup>ns</sup>	$x$
	Entropy (H)	Growth	3.674	1.343	0.33 *	Exp( $b_1x$ )
	Alpha ( $\alpha$ )	Compound	63.892	1.016	0.35 *	$b_1^x$
	Anisotropy (A)	Compound	155.239	0.377	0.23 <sup>ns</sup>	$b_1^x$
	H(1-A)	Growth	4.144	1.003	0.37 *	Exp( $b_1x$ )
	RVI	Compound	74.608	2.152	0.45 *	$b_1^x$
	T33	$S$	5.043	-0.025	0.40 *	Exp( $b_1/x$ )
WorldView-2 (dataset C)	Band 1 (Coastal)	Compound	199.643	0.986	0.35 *	$b_1^x$
	Band 2 (Blue)	Compound	226.947	0.980	0.41 *	$b_1^x$
	Band 3 (Green)	Compound	211.070	0.985	0.39 *	$b_1^x$
	Band 4 (Yellow)	Compound	192.902	0.988	0.32 *	$b_1^x$
	Band 5 (Red)	Compound	179.355	0.990	0.36 *	$b_1^x$
	Band 6 (Red-Edge)	Compound	167.905	0.996	0.23 <sup>ns</sup>	$b_1^x$
	Band 7 (NIR1)	—	—	—	<0.1	—
	Band 8 (NIR2)	—	—	—	<0.1	—
	NDVI <sub>7-5</sub>	Growth	4.517	0.002	0.33 *	Exp( $b_1x$ )
	NDVI <sub>8-5</sub>	Growth	4.545	0.002	0.37 *	Exp( $b_1x$ )
	NDVI <sub>7-6</sub>	Compound	7.233	1.020	0.42 *	$b_1^x$
	NDVI <sub>8-6</sub>	Compound	5.256	1.021	0.44 *	$b_1^x$
FBD/ALOS & WorldView-2 (dataset D)	CVI <sub>1</sub>	Linear	-132.333	62.275	0.52 **	$x$
	CVI <sub>2</sub>	Linear	-114.558	54.896	0.62 **	$x$
	CVI <sub>3</sub>	Linear	-107.183	46.293	0.60 **	$x$
	CVI <sub>4</sub>	Linear	-95.233	41.881	0.49 *	$x$
	CVI <sub>5</sub>	Linear	-65.017	32.089	0.56 **	$x$
	CVI <sub>6</sub>	Linear	-36.260	26.556	0.41 *	$x$
	CVI <sub>7</sub>	Linear	-67.279	19.682	0.20 <sup>ns</sup>	$x$
	CVI <sub>8</sub>	Linear	-110.518	24.296	0.24 <sup>ns</sup>	$x$

<sup>ns</sup> Not significant. \* Significant at the 0.05 level.

\*\* Significant at the 0.01 level. x: Pixel value of the parameter maps.

Although MLR was the approach frequently used to predict changes in forest biomass in previous studies [69,105,106], several problems remain with these models. For example, not all variables are linearly correlated with the AGB [55,107], and thus the variables not included in the linear models should be analyzed by another statistical method. Accordingly, the artificial neural network (ANN) approach, a very useful modeling technique for non-linear problems [75], was also used to produce predictive models to estimate the AGB using the multilayer perception (MLP) algorithm. For each dataset (A, B, C, D, and E), three MLP models, called MLP1, MLP2, and MLP3, were achieved using the principal components that were included in the MLR model, using all the principal components extracted from the corresponding dataset as mentioned above, and using all the original variables (*i.e.*, not linear-transformed) from each dataset (in datasets C and E, the bands 7 and 8 of WorldView-2 were included), respectively.

#### **4.1.6 Error Assessments of Estimated to Observed AGB**

In this study, the coefficient of determination ( $R^2$ ) of the actual vs. predicted AGB and the absolute and relative RMSEs (root mean square error) were used to evaluate the quality and reliability of the estimate models for forest biomass. The absolute RMSE (Mg/ha) of each biomass estimated model was calculated as  $\text{SQRT}(\text{SUM}(B_E -$

$B_O)^2/n)$ , where  $B_E$  is the estimated biomass,  $B_O$  is the AGB derived from the inventory data, and  $n$  is the number of the plots. The relative RMSE (%) was defined as  $\text{RMSE}/\text{Mean}(B_O) \times 100$ .



## **4.2 Results**

In our study, using the single variables derived from the PALSAR/ALOS and WorldView-2 data explained only approximately 20% to 50% of the variance in the plot-level measurements for the forest biomass (Table 5). Accordingly, combinations of several variables were considered to improve the relationships with the AGB.

### **4.2.1 Estimating Forest Biomass Using the FBD/PALSAR Data**

Numerous studies have found that polarization ratios have advantages for biomass estimation because these ratios do not saturate as quickly as single polarization data [106,108]. Moreover, ratios are known to mitigate topographic effects [109] and to reduce forest structural effects due to forest type [110,111]. However, the relationship of the polarization ratio of the FBD data with the field biomass was worse than that of the single polarization data in our study. Thus, we attempted to investigate whether the combination of the three variables could improve the biomass estimation. Using the calibration dataset ( $n = 63$ ), stepwise linear regression was first used to establish a relationship between the observed AGB as the dependent variable to be predicted and the two principal components (PC), which were extracted from the linear-transformed backscatter coefficients (HH and HV) of the FBD data and the ratio of HV to HH as possible

independent variables. The regression can be expressed as the following:

$$B = 137.978 + 18.523 \times P_{a1} + 6.289 \times P_{a2} \quad (17)$$

where  $B$  is the estimated biomass and  $P_{a1}$  and  $P_{a2}$  are the two principal components of dataset A. The FBD/PALSAR-derived MLR model explained approximately 68% of the variance in the validation dataset ( $n = 27$ ) and produced a relative RMSE of 31.74% (Table 6). An  $F$ -test indicated that the model is significant at the 0.01 level ( $P = 0.008$ ).

**Table 6.** Performance of the multivariate linear regression (MLR) and multilayer perception (MLP) models for the AGB estimation.

Dataset	Models	Calibration ( $n = 63$ )			Independent Validation ( $n = 27$ )		
		$R^2$ Actual vs. Predicted	RMSE/(Mg/ha)	Relative RMSE/%	$R^2$ Actual vs. Predicted	RMSE/(Mg/ha)	Relative RMSE/%
A	MLR	0.70 **	43.09	30.61	0.68 **	45.36	31.74
	MLP1	0.67 **	46.98	33.37	0.67 **	47.85	33.48
	MLP3	0.71 **	42.77	30.38	0.68 **	46.33	32.42
B	MLR	0.75 ***	38.55	27.38	0.71 ***	42.82	29.97
	MLP1	0.67 **	47.21	33.53	0.64 **	51.99	36.38
	MLP2	0.63 **	53.66	38.12	0.64 **	52.58	36.79
	MLP3	0.73 ***	41.35	29.37	0.68 **	46.76	32.72
C	MLR	0.70 **	42.87	30.45	0.65 **	49.40	34.57
	MLP1	0.65 **	51.11	36.30	0.59 *	57.23	40.05
	MLP2	0.69 **	44.58	31.67	0.66 **	48.52	33.95
	MLP3	0.72 ***	40.71	28.92	0.70 **	41.97	29.37
D	MLR	0.83 ***	30.75	21.84	0.79 ***	35.13	24.58
	MLP1	0.70 **	42.99	30.54	0.68 **	44.02	30.80
	MLP2	0.67 **	46.89	33.31	0.66 **	47.33	33.12
	MLP3	0.78 ***	34.41	24.44	0.75 ***	37.88	26.51
E	MLR	0.91 ***	22.39	15.90	0.89 ***	24.41	17.08
	MLP1	0.80 ***	34.92	24.80	0.76 ***	37.30	26.10
	MLP2	0.83 ***	31.09	22.08	0.81 ***	33.55	23.48
	MLP3	0.93 ***	19.57	13.90	0.89 ***	24.38	17.06

\* Significant at the 0.05 level. \*\* Significant at the 0.01 level. \*\*\* Significant at the 0.001 level.

Based on the multilayer perception (MLP) algorithm, the neural network approach was also used to produce several models to estimate the AGB using the FBD/PALSAR dataset (A). However, there was no MLP2 model for this dataset because the two principal components were included in the MLR model. The MLP1 and MLP3 models were created using the two PCs and directly using the values of HH, HV, and HV/HH in the FBD data, respectively. The MLP1 model for AGB estimation had a moderate fit of  $R^2 = 0.67$  with a relative RMSE of 33.48% in the validation dataset (Table 6). In other words, approximately 33% of the variance in the observed AGB was not explained by this model. The MLP3 model explained approximately 68% of the variance and showed a relative RMSE of 32.42%. There was little difference in explaining the variance between the three models derived from dataset A, possibly because the two principal components included most of the information in the dataset, with a very high cumulative variance of 99.99%.

#### **4.2.2 Estimating Forest Biomass Using the PLR/PALSAR Data**

Although some variables of the PLR/PALSAR data (dataset B) were significantly correlated with forest biomass, most of them had poor fits and explained less than 40% of the variance. For the purpose of increased accuracy, an MLR model was also established for the

AGB estimation using the five PCs of the PLR dataset as possible independent variables. The regression can be expressed as follows:

$$B = 140.134 + 12.417 \times P_{b1} + 7.099 \times P_{b2} + 7.970 \times P_{b3} + 14.295 \times P_{b4} \quad (18)$$

where  $B$  is the estimated biomass and  $P_{b1}$ ,  $P_{b2}$ ,  $P_{b3}$ , and  $P_{b4}$  are the principal components produced from the ten linear-transformed parameters of the PLR/PALSAR data (Table 5). This linear model showed an  $R^2$  of 0.71 and a relative RMSE of 29.97% when validated with the independent testing dataset (Table 6). An  $F$ -test indicated that the MLR model is significant at the 0.001 level ( $P < 0.001$ ).

In addition, three MLP models, called MLP1, MLP2, and MLP3, were used for the biomass estimate using the four PCs included in the MLR regression, using all five PCs extracted from the PLR/PALSAR data, and using the ten parameters that were not linear-transformed, respectively. The MLP1 and MLP2 models had the lowest fits to the observed AGB in the validation dataset, with an  $R^2$  of 0.64 and relative RMSEs of 36.38% and 36.79%, respectively. The MLP3 model explained approximately 68% of the variance and had a relative RMSE of 32.72%.

#### **4.2.3 Estimating Forest Biomass Using the WorldView-2 Data**

Four principal components with a cumulative variance of 99.09% were extracted from the ten linear-transformed parameters of the

WorldView-2 data (except for bands 7 and 8) to perform MLR. Three of the PCs were included by the stepwise approach. The MLR model can be expressed by the following equation:

$$B = 154.335 + 7.770 \times P_{c1} - 5.177 \times P_{c3} - 4.260 \times P_{c4} \quad (19)$$

where  $B$  is the estimated biomass and  $P_{c1}$ ,  $P_{c3}$ , and  $P_{c4}$  are the PCs extracted from dataset C. This WorldView-2 derived linear model was only able to explain approximately 65% of the variance, with a relative RMSE of 34.57% in the validation plots (Table 6).

Regarding the MLP-based models, MLP1 and MLP2 were moderately correlated with the observed biomass by an  $R^2$  of 0.59 and 0.66, respectively, whereas MLP3 had the highest correlation with the AGB, which explained approximately 70% of the variance and led to a relative RMSE of 29.37%. For the WorldView-2 data, we found that the best MLP-based model ( $R^2 = 0.70$  and RMSE = 41.97 Mg/ha for the validation data) was more highly correlated with the AGB than the MLR-based model ( $R^2 = 0.65$ , RMSE = 49.40 Mg/ha), primarily due to the use of bands 7 and 8 in the MLP3 model.

#### **4.2.4 Estimating Forest Biomass Using the CVIs**

Table 5 indicates that the eight CVI variables developed from the combination of the FBD/ALOS and WorldView-2 data had the best-fitted linear correlations with the AGB when using the eight

functions (Equations (6) to (13)) to fit. Therefore, the values of the eight CVIs were directly used to perform the principal component analysis without linear transformation. Three PCs with a cumulative variance of 99.56% were extracted from the CVI dataset. Then, using the 63 calibration plots, the MLR model was obtained by the stepwise linear approach and can be expressed as the following:

$$B = 148.651 + 16.586 \times P_{d1} - 9.822 \times P_{d2} \quad (20)$$

where  $B$  is the estimated biomass and  $P_{d1}$  and  $P_{d2}$  are the two principal components of the dataset D. The analysis of variance indicated that the CVI dataset provided a significant improvement in the predicted values and had a lower relative RMSE compared to the use of single PALSAR or optical sensor data. This MLR model was able to explain an additional 11% and 14% of the variability in the plot-level biomass compared with the MLR models of the FBD and WorldView-2 data, respectively.

In terms of the three MLP-based models, MLP1 and MLP2 only explained approximately 68% and 66% of the variance and produced a relative RMSE of 30.80% and 33.12%, respectively. The MLP3 model was the most significantly correlated to the observed AGB at the 0.001 level, with a relative RMSE of 26.51% in the validation plots (Table 6). However, in contrast to the MLR model using dataset D, a slightly

poor explanation for the percentage variance was observed for the MLP3 model when validated with the independent testing dataset, possibly due to the good linear relationships between the AGB and the CVI variables.

#### **4.2.5 Estimating Forest Biomass by Combining the PALSAR and WorldView-2 Sensors**

As mentioned above, modeling forest biomass using the fusion of FBD/ALOS and WorldView-2 data provided improved fits relative to their respective individual values. However, although the result is promising, no more than 80% of the variability of the field biomass could be explained by the models derived from this fusion. Previous studies have reported increased accuracy when simultaneously using several datasets from different sensors [43,58,61,75,107,112] or using SAR images from more than one date [106,113,114] or further improvement of the model. Using the 31 variables in Table 5, seven PCs with a cumulative variance of 92.03% were produced as possible independent variables to achieve the multivariate stepwise regression. According to the component matrix, the first PC was dominated by the eight CVIs, the second PC was mainly composed of the variables of the WorldView-2 dataset and called the optical factor, while the third PC was called the vegetation index factor because it was dominated

by the RVI of the PLR data, the NDVIs of WorldView-2, and CVI1 to 4. The other four PCs were named as comprehensive factors. As a result, the linear model can be expressed as follows:

$$B = 141.418 + 13.887 \times P_{e1} + 13.084 \times P_{e2} + 8.274 \times P_{e3} + 10.270 \times P_{e4} + 13.093 \times P_{e6} \quad (21)$$

where  $B$  is the estimated biomass and  $P_{e1}$ ,  $P_{e2}$ ,  $P_{e3}$ ,  $P_{e4}$ , and  $P_{e6}$  are the principal components extracted from the dataset E. The standardized regression coefficients of the five PCs were 0.702, 0.681, 0.392, 0.519, and 0.677, respectively, which can be used to explain the relative weight of these factors in the model. The predicted value of this MLR model showed a significantly improved correlation ( $P < 0.001$ ) with the observed biomass, which was able to explain approximately 89% of the variance and give a much lower RMSE of 24.41 Mg/ha (relative RMSE = 17.08%) for the validation dataset (Table 6). The improvement obtained by combining the two PALSAR datasets and the WorldView-2 image is in agreement with the results of previous studies [44,54,58,75,107,115], which found that integrating the optical and SAR data for estimating forest biomass can counterbalance the limitations associated with each of the different available optical and radar data types.

The MLP-based models using dataset E also showed good fits with



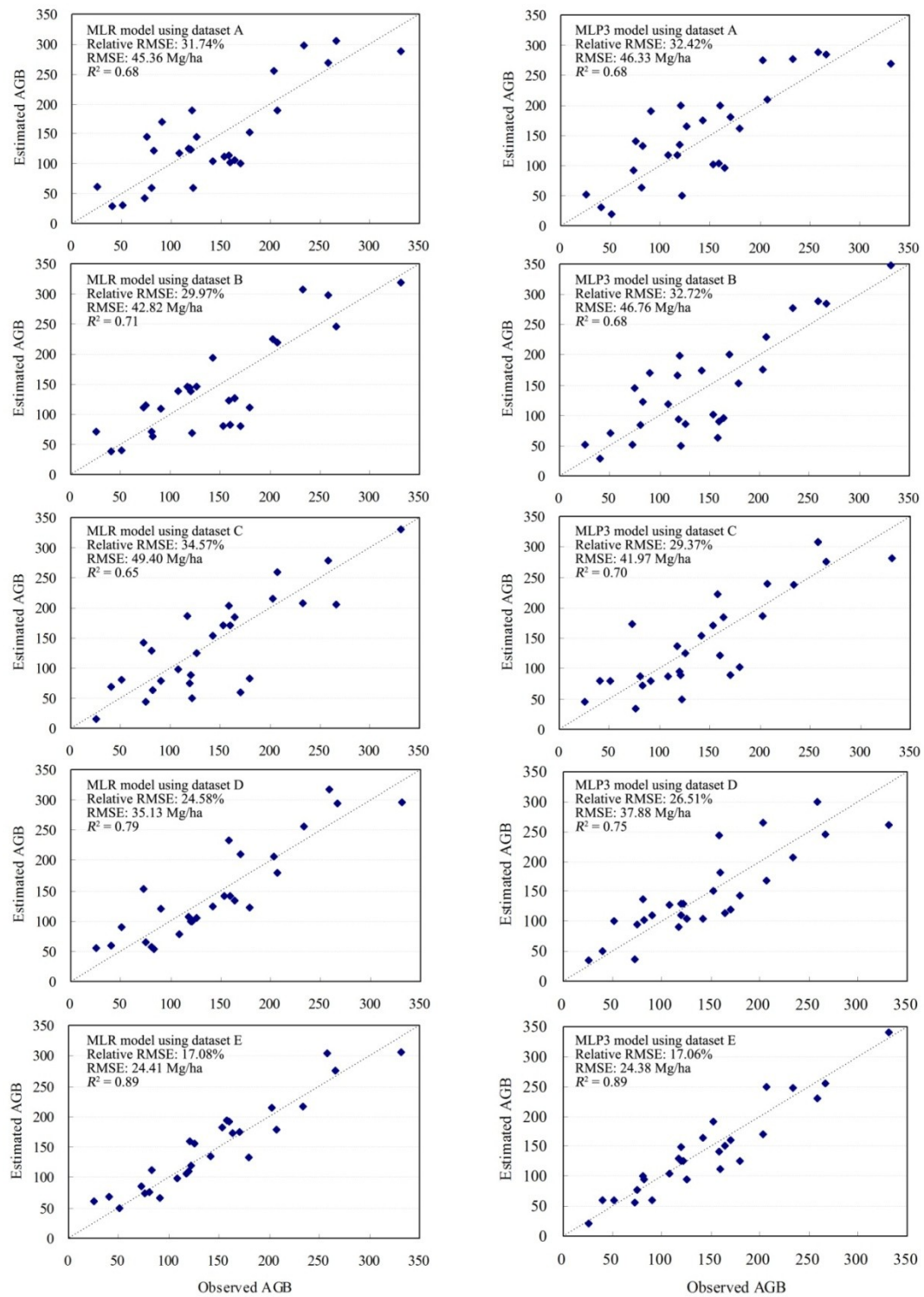
the field biomass in our study. The MLP3 model was the most correlated to the AGB, with an  $R^2$  of 0.93 and 0.89 for the training and testing data and a relative RMSE of 13.90% and 17.06%, respectively. However, MLP1 and MLP2 explained approximately 76% and 81% of the variance and produced a relative RMSE of 26.10% and 23.48% for the validation data, respectively.

#### **4.2.6 Best Estimated Model Selection and AGB Mapping in Study Area**

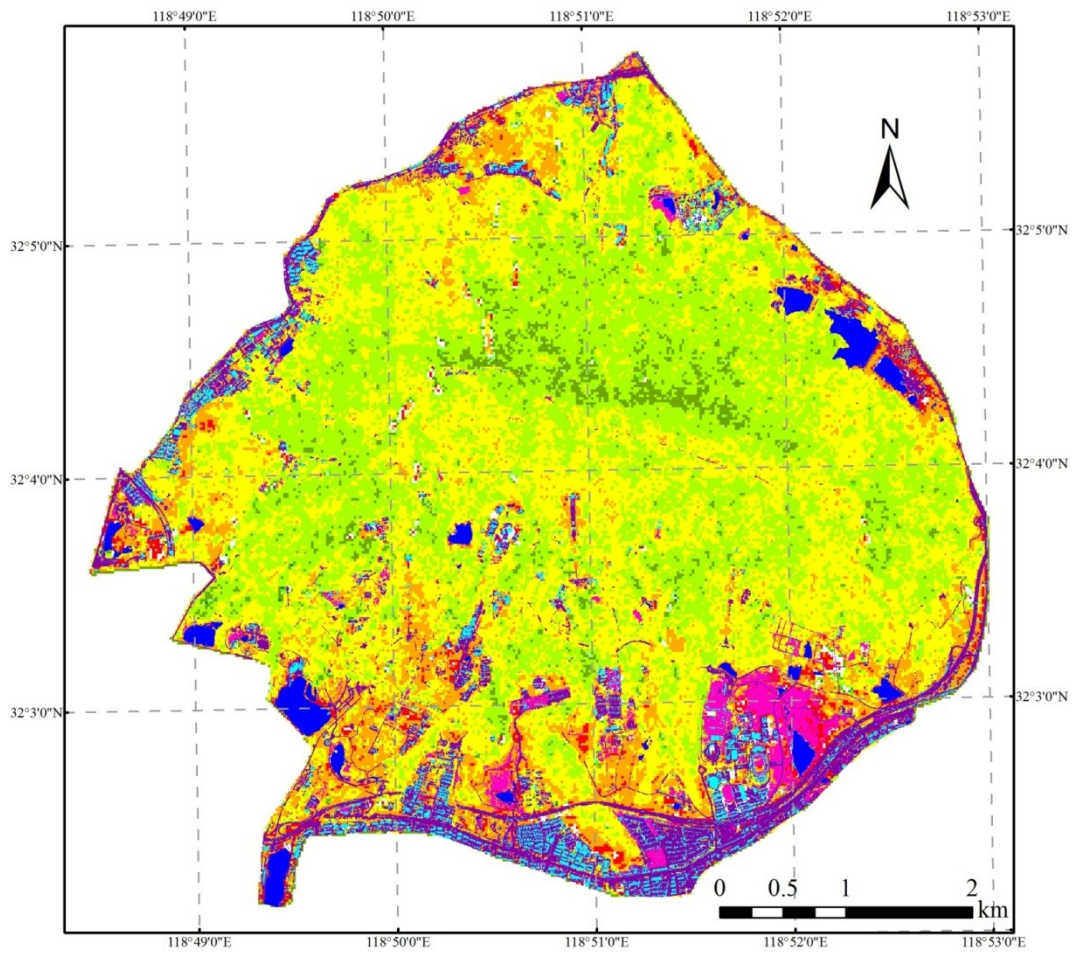
The validations of the forest biomass estimation models in Table 6 yielded the following results: (1) the MLP3 models had better fits than the MLP1 and MLP2 models, which were established using the principal components extracted from the linear-transformed variables in the five datasets, indicating the high capability of the neural network model for non-linear problems [101,107]; and (2) the validation accuracy during model development improved as the information content of the datasets increased, *i.e.*, the best performances were obtained by the models using dataset E, followed by the models using dataset D, while using the single images produced the lowest correlations. For comparison purposes, the predicted *vs.* observed biomass of the testing samples ( $n = 27$ ) was plotted for the MLR and MLP3 models using the five datasets and is displayed in

Figure 11. The plot shows the fairly high agreements between the estimates and observations of MLR and MLP models using dataset E.

In addition, the differences in the absolute bias of the estimated *vs.* observed biomass between the MLR and MLP models and between the five datasets were tested by analysis of variance (ANOVA). The results suggest that the models established using dataset E exhibited a significantly lower bias at the 0.05 level than the models established using the other four datasets, while a highly consistent bias distribution was observed in the MLR and MLP3 of dataset E ( $F = 0.000$ ,  $P = 0.995$ ). Although the MLP3 model ( $R^2 = 0.93$ ) fit the AGB slightly better than the MLR model ( $R^2 = 0.91$ ) in the calibration plots, the two models had the same  $R^2 = 0.89$  for the testing data, indicating that the MLR model was more stable than the MLP model. In addition, the MLP-based model is more difficult to interpret than the MLR regression because it has one or more hidden layer(s) and may therefore appear to be a “black box”. Accordingly, the MLR model derived from dataset E was further used to retrieve the AGB of forests in the study area at the pixel level. The forest mask map and the land-use classification were generated in a previous study using the WorldView-2 image [71]. The overlay of the AGB map with the land-use classification is displayed in Figure 12.



**Figure 11.** Comparison of the estimated and observed AGB for the MLR and MLP3 models using different datasets (Mg per hectare). The dashed line is the 1:1 line.



### Legend

#### Non-forest area

- Building
- Water
- Soil
- Road

#### Biomass (Mg/ha)

- |   |   |  |
|---|---|--|
| <span style="color: white;">■</span> <10        | <span style="color: yellow;">■</span> 150 - 200     | <span style="color: green;">■</span> 350 - 400     |
| <span style="color: red;">■</span> 10 - 50      | <span style="color: orange;">■</span> 200 - 250     | <span style="color: darkgreen;">■</span> 400 - 450 |
| <span style="color: orange;">■</span> 50 - 100  | <span style="color: lightgreen;">■</span> 250 - 300 |  |
| <span style="color: yellow;">■</span> 100 - 150 | <span style="color: limegreen;">■</span> 300 - 350  |  |

**Figure 12.** AGB mapping in the study area retrieved by the MLR model using dataset E.

The extrapolations using the predicted models for the remaining area might lead to the overestimated or underestimated biomass due to the limited number of calibration and validation plots, because these

plots usually had a smaller range of AGB values than the existent in the whole study area. Consequently, the reliability of the finally recommended model was tested by the quantitative comparison of the two AGB mappings retrieved by the MLR and MLP3 models using dataset E. The two biomass maps showed a very high correlation with an  $R^2$  of 0.993. In addition, a total of 1500 random points were produced from the forest area. The AGB values of these points in the above two maps (MLR and MLP3) were then extracted for establishing a linear regression between the MLR value as the dependent variable ( $y$ ) and the MLP3 value as the independent variable ( $x$ ) (Figure 13). The result indicates that the two datasets were in good agreement.

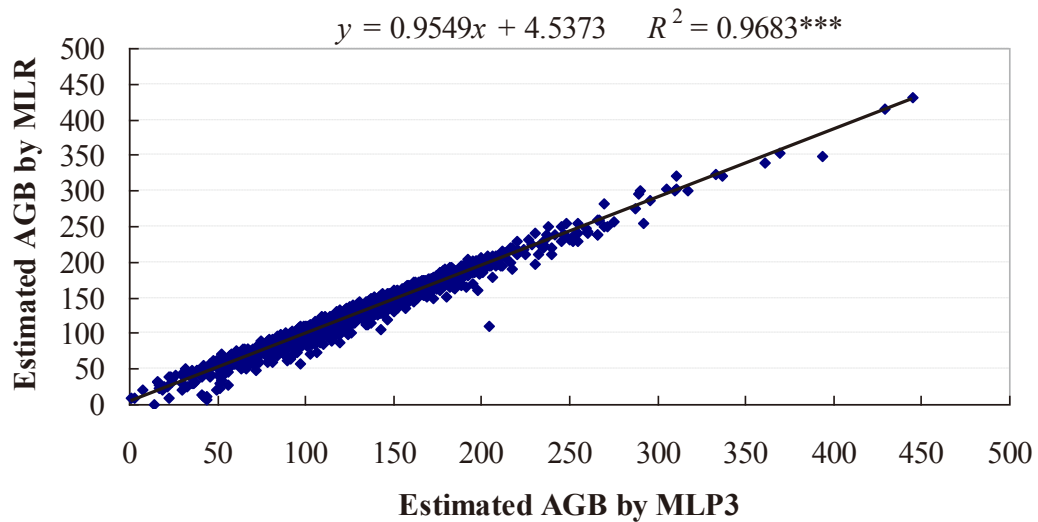


**Figure 13.** Linear regression between the AGB values in the 1500 random points predicted by the MLR and MLP3 models using dataset E (Mg/ha).

#### **4.2.7 The Effects of Forest Type and Vertical Structure on AGB Estimation**

In this study, the forests in the 90 plots were divided into three types (broad-leaved, coniferous, and mixed forest, Table 1) and five vertical structures (VS1, VS2, VS3, VS4, and VS5, Figure 14) to analyze the effects of different forest types and structures on AGB retrieval. In Figure 14, the lengths of the bold lines represent the relative numbers of the stems of the three DBH classes ( $DBH > 20$ ,  $10 \leq DBH \leq 20$ , and  $DBH < 10$  cm) in the plots. For example, in VS1, the ratio of stems decreased with increased DBH in a pyramid shape, while the inverse relationship was observed for VS3 in the form of an inverted pyramid. In VS5, the number of stems at  $10 \leq DBH \leq 20$  cm is far less than that at  $DBH > 20$  and  $DBH < 10$  cm. Due to the limited number of validation plots ( $n = 27$ ), these 27 samples were divided into nine groups such that each group included a low, moderate, and high biomass plot. Then, each group with three plots was used once to replace three plots of the calibration data for achieving the MLR and MLP models using the dataset E (*i.e.*, nine iterations), yielding a total of 270 accumulated validation samples for the accuracy assessment of the biomass estimation. The absolute and relative RMSEs of the multivariate stepwise regressions and the MLP-based models using



the dataset E with 10 iterations are shown in Table 7, in which the forest types and the vertical structures are distinguished. The results indicate that the relative RMSE decreases gradually from broad-leaved to coniferous to mixed forest. VS4, in which the stem ratio was approximately the same in the 3 DBH classes, had a lower absolute RMSE, whereas VS3, in which the forest was dominated by large-size trees and lacked undergrowth trees, has the highest RMSE of the five vertical structures.

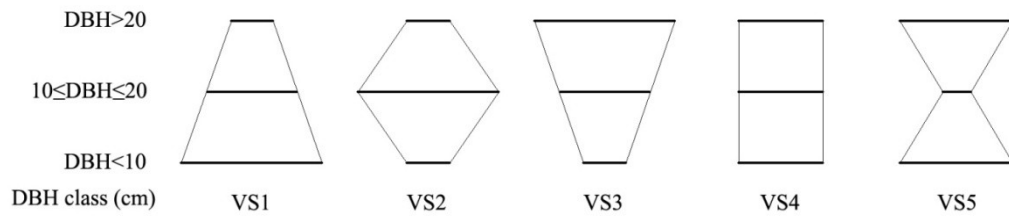


**Figure 14.** Vertical Structure Charts.

**Table 7.** The absolute and relative RMSEs of the MLR and MLP3 models using dataset E with 10 iterations for different forest types and vertical structures.

Forest Types and Vertical Structures	MLR Models Using the Dataset E		MLP3 Models Using the Dataset E	
	RMSE/(Mg/ha)	Relative RMSE/%	RMSE/(Mg/ha)	Relative RMSE/%
Broadleaved ( $n = 137$ )	31.44	21.92	29.80	20.78
Coniferous ( $n = 34$ )	23.63	16.41	21.71	15.08
Mixed ( $n = 99$ )	15.89	11.51	18.99	13.75
VS1 ( $n = 130$ )	18.56	15.34	20.35	16.82
VS2 ( $n = 36$ )	21.82	17.25	19.76	15.62
VS3 ( $n = 29$ )	58.94	24.74	56.88	23.88
VS4 ( $n = 33$ )	12.11	9.54	11.27	8.87
VS5 ( $n = 42$ )	34.49	20.26	32.69	19.21

#### **4.2.8 The Effects of Other Factors on AGB Estimation**

Pine forests are widely distributed over a lot of countries that are counting on REDD+ programs for revenue generation through biomass conservation. With the purpose of the probable implications of our research for these countries, we analyzed the effect of the relative number of pine trees in the plots on the AGB estimates by dividing the above 270 accumulated validation samples into three groups: the relative number of pine trees ranging from 0% to 30% (PR1), 30% to 60% (PR2), and over 60% (PR3), respectively. The absolute and relative RMSEs of the three groups are documented in Table 8. The results indicate that PR2 and PR3 had lower RMSEs, whereas PR1, in which the forests were mainly dominated by broad-leaved trees, had the highest RMSEs of the three groups. In other words, the method developed by our study can be used to accurately estimate the AGB of the forests containing pine trees more than 30%.

In addition, we selected the slope and the aspect as environmental factors that could possibly impact the retrieval of the AGB. The slope was generated from the DEM with a spatial resolution of 30 m and ranged from 0° to 31° in the 90 plots. The aspect was defined as north (Azimuth ranging from 0° to 22.5° and 337.5° to 360°), northeast



(22.5° to 67.5°), east (67.5° to 112.5°), southeast (112.5° to 157.5°), south (157.5° to 202.5°), southwest (202.5° to 247.5°), west (247.5° to 292.5°), and northwest (292.5° to 337.5°), and there was no flat type in the field plots. We first analyzed the relationships between the slope and the RMSEs. No significant correlations ( $P > 0.05$ ) have been found, suggesting that the corrected measures mitigated the effect of different effective back-scattering surface areas caused by the local topography and SAR imagery geometry [116,117]. However, when the 270 validation samples were divided into three groups as gentle slope (GS, 0° to 10°), moderate slope (MS, 10° to 20°), and steep slope (SS, 20° to 31°) for counting estimated errors, we found that SS had the highest absolute and relative RMSEs of the three groups (Table 8). In terms of the aspects, the directions of northeast, east, southeast, south, and southwest had lower relative RMSEs less than 15%, whereas the other three directions had the relative RMSEs of approximately 20%.

**Table 8.** The absolute and relative root mean square errors (RMSEs) of the MLR and MLP3 models using dataset E with 10 iterations for the relative numbers of pine trees in plots, slopes, and aspects. GS, gentle slope; MS, moderate slope; SS, steep slope.

Other Three Factors	MLR Models Using the Dataset E		MLP3 Models Using the Dataset E	
	RMSE/(Mg/ha)	Relative RMSE/%	RMSE/(Mg/ha)	Relative RMSE/%
PR1 ( $n = 148$ )	32.06	22.40	30.25	21.13
PR2 ( $n = 75$ )	16.37	11.84	19.26	13.93
PR3 ( $n = 47$ )	21.59	15.03	20.08	13.98
GS ( $n = 129$ )	19.76	14.31	18.43	13.35
MS ( $n = 93$ )	22.88	15.52	23.21	15.75
SS ( $n = 48$ )	31.08	22.37	30.34	21.84
North ( $n = 25$ )	25.87	20.67	26.31	21.02
Northeast ( $n = 16$ )	20.94	14.34	19.76	13.53
East ( $n = 15$ )	13.85	12.91	15.16	14.13
Southeast ( $n = 52$ )	18.57	13.17	16.71	11.85
South ( $n = 42$ )	15.98	12.24	14.66	11.23
Southwest ( $n = 36$ )	19.31	13.65	19.10	13.50
West ( $n = 39$ )	33.02	21.17	31.27	20.05
Northwest ( $n = 45$ )	30.65	19.90	30.92	20.08

### 4.3 Discussions

Mapping the spatial distribution of forest aboveground biomass is an important and challenging task. For a given ecosystem, these maps can be used to monitor forests and capture national deforestation processes; forest degradation; and the effects of conservation actions, sustainable management and the enhancement of carbon stocks [56]. In China, the national biomass estimation was mainly completed by conducting national forest inventories using the sample plotting method every five years, which is difficult to be implemented in remote areas. In recent years, although some common approaches of remote sensing have been used for estimating Chinese forest biomass on a landscape to regional scale using optical images [39,118] or SAR data [59], the development of enhanced methods (e.g., the combined use of different sensors) that can accurately retrieve forest biomass remains an important topic of study [119] due to not only the vast size of forests in China but also the limited usefulness of empirical models for different forests. Therefore, this study developed an improved approach that exploits the synergy of ALOS PALSAR and WorldView-2 data to integrate the advantages of both sensors for biomass estimation.

Although the ratio of radar backscattering is often effective for

estimating forest biomass [108–111], our results did not confirm this, most likely because the SAR data were adequately geometrically and radiometrically terrain corrected to reduce topographic effects during pre-processing. Acquiring the datasets during the dry seasons (October for the FBD and March for the PLR) also helped mitigate the influence of soil and surface moisture on L-band microwave backscatter [120], which can be particularly strong when low levels of aboveground biomass are present [121]. Moreover, another reason for the poor correlation between the ratio of backscattering and the observed AGB may be the high biomass level in the study area, which is far greater than the reported saturation of approximately 60–100 Mg/ha for L-band SAR.

In our study, in addition to the backscattering coefficients of PLR/PALSAR data, several decomposition parameters, such as entropy and Alpha, and other variables (*i.e.*, RVI and T33) were used to retrieve the AGB. Although the single variables of the PLR data had relatively low fits with the field biomass, the combined use of these variables in principal component analysis improved the estimate accuracy to approximately 71%. In addition, based on the ability of multispectral images to provide surface information about tree crowns and ability of SAR data to measure forests based on backscattering

from the branches and stems of the trees, a new variable called CVI (combined volume index) was developed using the HV backscattering of the FBD data and the bands of the WorldView-2 image. The CVI dataset yielded a significant improvement in the biomass estimation compared to the use of single PALSAR or an optical sensor. Moreover, we found that the first PC extracted from the dataset E was dominated by the eight CVIs and had the highest weight in the final MLR model. Consequently, the results of this study recommend the use of these variables introduced above in the AGB estimation of forests. However, this conclusion is based on empirical models and should be further studied and verified in other forests and different seasons [69,122].

The results from this study suggest that the standard NDVI calculated from band 7 (NIR1, 0.77–0.90  $\mu\text{m}$ ) and band 5 (Red, 0.63–0.69  $\mu\text{m}$ ) of the WorldView-2 data had the lowest correlation with the surveyed AGB in the 4 NDVIs. This poor correlation reflected the saturation level reached on densely vegetated areas [69,101,103,123]. In the highly dense forests, the red band, which can be absorbed by vegetation, reaches a peak, while the reflectance of near infrared continues to increase due to multiple scattering effects [102]. Furthermore, it is likely that the WorldView-2 image was acquired in December, when the leaves of some of the tree species had fallen and

the reflectance of multispectral bands was easily disturbed by the undergrowth vegetation and the ground surface, in which the forest was dominated by deciduous trees. However, we also found that many forests dominated by deciduous trees had similar reflectance characteristics with the evergreen forests by comparing their spectral features. This result probably resulted from the distribution of evergreen broad-leaved trees under the deciduous trees. Accordingly, the difference of the reflectance between deciduous and evergreen broad-leaved forests in the study area needs to be clarified by further study using another WorldView-2 image acquired in summer.

In addition, we found that the developed NDVIs computed from the NIRs and the additional red-edge band were slightly better fitted to the AGB than those calculated from the NIRs and the red band. This result was consistent with previous studies indicating that red-edge or longer wavelengths result in higher correlations with biomass in dense vegetations than the standard NDVI [41]. The indices calculated from the red-edge may be more sensitive to vegetation properties such as canopy biomass and chlorophyll content than other electromagnetic spectrums [37,124]. A slight change in these vegetation properties will lead to a shift in the red-edge curve [125]. In addition, the expanded NDVIs computed from the red-edge and NIRs can mitigate the effects

of the atmospheric and water absorption and soil background [126]. As a consequence, the additional bands of the WorldView-2 satellite are able to estimate biomass in highly dense forests. However, these bands should be further tested by application to other forests during different seasons.

Most previous studies used a simple logarithmic or exponential function to establish relationships between the AGB and the backscattering coefficients of the SAR data [47,56,59,127]. However, when using the eight functions listed in the methods section for fitting, we determined that the variables had different best-fitted models, as judged by the  $R^2$  value and significance. For most parameters of PALSAR data, the compound and growth functions had better fits than the other functions. In fact, the trend lines of the two functions were similar to those of the exponential or logarithmic functions in correlation with the observed biomass, but they had higher significance than the latter in the model test. Finding the best-fitted function is favorable for the improvement of AGB retrieval when using the MLR method to estimate the biomass because implementing linear transformations for these curvilinear-correlated variables is essential before performing the multivariate stepwise regression. However, the neural network approach did not improve the AGB

estimation when using linear transformations, as indicated by the higher correlation with the observed biomass for the MLP3 models than for the MLP1 and MLP2 models in the five datasets.

MLR is a common approach used for estimating the biomass of forests [69,105,106]. However, with the increasingly synergistic use of different sensors, the MLR method has some limitations, e.g., the estimate accuracy no longer improves when additional variables are added [58] because not all parameters are linearly correlated with the biomass [42,55,101,104]. Accordingly, for the purpose of comparison with the multivariate stepwise regression, the neural network approach was also used to develop several estimated models using the multilayer perception algorithm. Several studies have indicated that the neural network approach significantly improves forest biomass estimation [38,55,75,101,107]. However, in this study, the results obtained using the network approach were inconsistent for different datasets. Overall, the MLP3 models had slightly better fits to the field biomass in the calibration plots. However, for dataset D, the MLP models were more poorly fitted to the AGB than the MLR model in the training and testing plots. The superior fit of the MLR model may be due to the good linear correlations between the biomass and the CVI variables. In terms of dataset E, although the MLP3 model was



slightly better correlated with the AGB than the MLR model in the calibration plots, the two models had the same  $R^2$  value for the testing data, suggesting that the MLR model was more stable than the MLP model. As a result, our study recommended using the final MLR model rather than the MLP approach to map the AGB in the study area.

Figure 12 suggests that the final stepwise model can be used to retrieve the forest biomass when the AGB level is approximately 10 Mg/ha to 450 Mg/ha, levels that are typical of most subtropical and warm temperate zone forests in China [91], indicating that the approach generated by our study can provide some knowledge for AGB estimation in China. However, slightly lower  $R^2$  values and higher RMSEs were obtained in our study compared with previous studies [59,67,74,106,114]. Several factors may explain the relatively poor results. First, to contain the biomass levels of the study area, we investigated plots with AGBs that ranged from approximately 25 to 342 Mg/ha. Because no AGB plots lower than 60 Mg/ha were found in the closed stand, some plots with lower biomasses had to be located in open forest land, where the reflectance of remote sensors is easily affected by the ground surface, leading to high RMSEs at these plots. For example, the reflectance of NIRs in the closed forest is evidently

higher than that in open forest land. Second, the inexact calculation of the observed AGB could also lead to a high RMSE. Generally, the biomass of individual trees in the plot can be accurately estimated using allometric equations on the basis of the DBH and the height of the trees [44,59,90]. However, no allometric equations were available for the study area, indicating that further basic research is needed in this region. Therefore, we had to use the method presented by [91], in which the biomass of each plot is estimated from the regression of the biomass and the total volume of the plot. Although this method is considered accurate for AGB estimation over a large area and has been adopted by numerous researchers, the accuracy must be improved by incorporating more forest field data on a regional scale.

Moreover, we have analyzed the effects of different forest types and vertical structures on the biomass estimate. In terms of forest types, the RMSE decreases gradually from broad-leaved to coniferous to mixed forest. In the study area, most of the broad-leaved stands are composed of secondary forests derived from clear-cutting of the land. These stands have disorganized structures and lower AGBs, resulting in a higher RMSE for broad-leaved forest than for the other stands. However, the coniferous forests, which have a regular spatial structure and a higher AGB, are derived from manmade plantations that were

planted approximately 60 to 80 years ago. The mixed forests are mainly composed of coniferous trees with large sizes distributed in the upper layer and broad-leaved trees in the understory. These forests have a complicated spatial structure and high canopy density, increasing their sensitivity to the signals of both SAR and optical sensors and reducing ground surface effects. Of the five vertical structures, VS3 has the highest errors because the forest lacks undergrowth trees; the absence of undergrowth trees reduces the random scattering of the forest and enhances the single reflection of the ground surface on the SAR. By contrast, the VS4 forest, which has approximately same ratio of stems as the three DBH classes, has a complex spatial structure in which the scattering is characterized by a high degree of randomness and thus has the lowest estimated error.

Finally, we have analyzed the effects of the relative numbers of pine trees in plots, slopes, and aspects on the AGB estimation. We found that the PR1 group, in which the relative number of pine trees in the plots ranged from 0% to 30%, has higher average RMSEs than the other two groups, because most plots in PR1 were dominated by broad-leaved forests. By contrast, PR2 has the lowest RMSEs of the three groups, because most plots in PR2 were composed of mixed forests that had lower estimated errors than other forest types.

Additionally, although no significant correlations between the slope and the RMSEs have been found, the plots within steep slope had the highest average error. Two reasons may explain this result. First, the DEM data with a spatial resolution of 30 m was used for geometric and radiometric terrain correction, which is difficult to mitigate the effect of the steep topography on the back-scattering [49,117]. Consequently, this issue requests future studies using a high resolution DEM. Second, many forests in the plots within steep slope had the vertical structure of VS3 that had the highest estimated error of the five vertical structures. In terms of aspects, the plots facing the directions of west, northwest, and north had higher estimated errors than those facing other directions. The steep topography of the three directions, which had an average slope of  $14^{\circ}$ ,  $13^{\circ}$ , and  $11^{\circ}$ , respectively, probably leads to this result.

#### **4.4 Conclusions**

In our study, the single variables derived from the PALSAR/ALOS and WorldView-2 data correlated very poorly with the observed biomass and were able to explain only approximately 20% to 50% of the variance. Accordingly, combinations of several variables were considered to improve the relationship with the AGB. Using principal component analysis and multivariate stepwise regression, the performances of the FBD, PLR, and optical data for biomass estimation were improved to 65% to 71%. In addition, using the additional dataset derived from the combination of FBD/PALSAR and WorldView-2 data increased the performance to 79% and produced a relative RMSE of 24.58% when using MLR. Moreover, the synergistic use of the 31 variables introduced by our study resulted in further improvement, ultimately explaining 89% of the variance with a relative RMSE of 17.08%. The results presented here demonstrate that combining independent observation data from the PALSAR and WorldView-2 sources may provide great improvements for biomass estimation in the study area. However, because most biomass models or regressions are developed for specific locations, the models generated by our study should be further tested by application to other forests during different seasons. In addition, for the purpose of

comparison with the multivariate stepwise regression, a neural network approach using the multilayer perception (MLP) algorithm was used to produce several estimated models of forest biomass. However, few improvements were obtained from the MLP approach in this study. Consequently, we recommend using the final MLR model to map the AGB of the study area. Finally, analyzing the effects of different forest types and vertical structures on the biomass estimation revealed that the RMSE decreased gradually from broad-leaved to coniferous to mixed forest. In terms of different vertical structures, VS3 had the highest errors because the forest lacks undergrowth trees, while the VS4 forest, in which the three DBH classes have approximately the same ratio of stems, had the lowest RMSE.

## Chapter 5 Object-based Classification of Forest Types

### 5.1 Data Analysis Method

The Landsat-8 imagery was used to classify the forests of the study area into three stand types (broadleaved, coniferous, and mixed forest) by an object-based supervised classification approach using the Nearest Neighbor classifier built in the eCognition v8.8 software. The research flow chart in Figure 15 provides an overview of the methods.

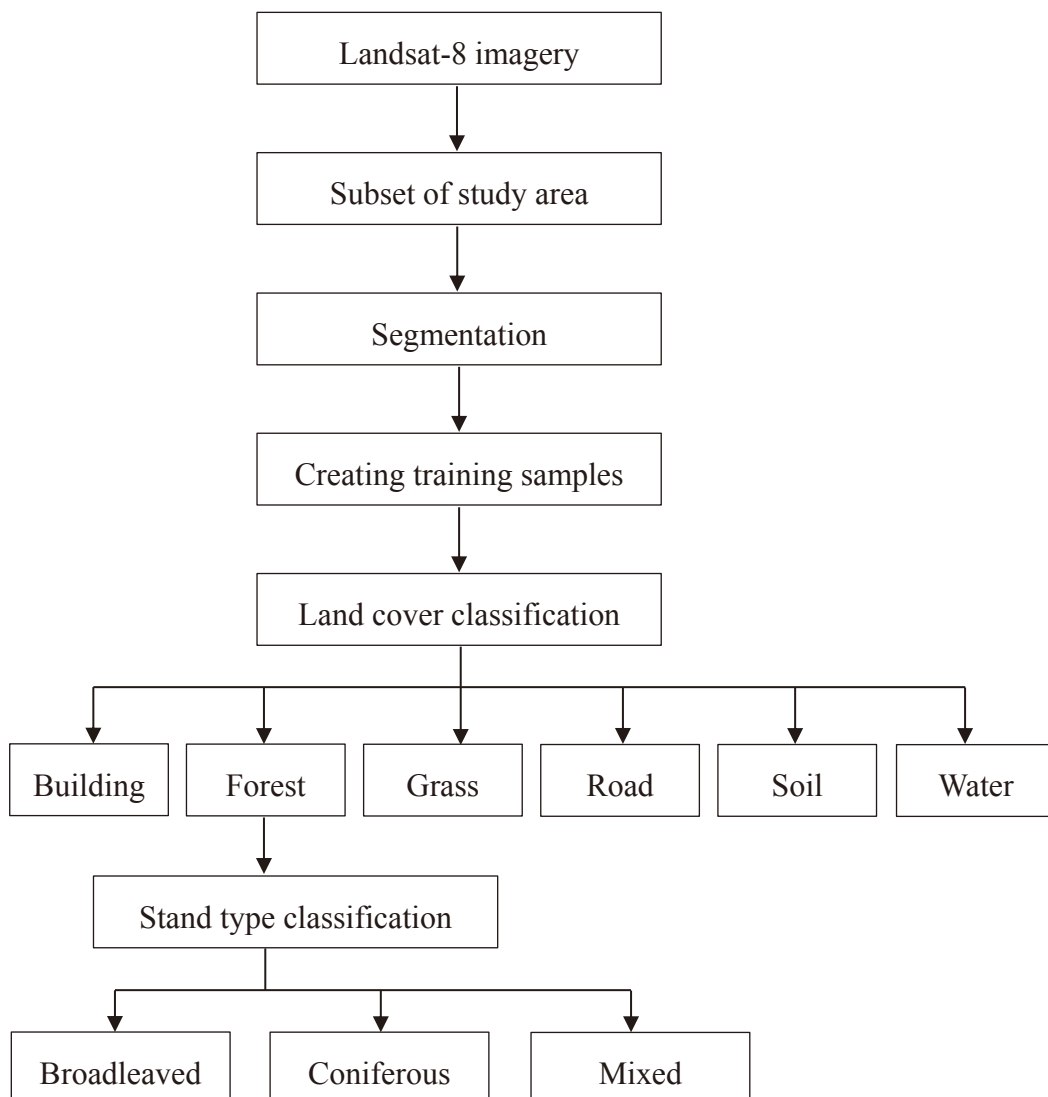


**Figure 15.** Research flow chart.

## 5.2 Results and discussions

### 5.2.1 Subset of the Study Area

Because the cover area of the Landsat-8 image is far more than the study area, for the purpose of decreasing processing time, a subset area that completely contained Purple Mountain was extracted from the Landsat-8 image using the Subset function built in ERDAS Imagine. The subset image is showed by R: G: B = NIR: Green: Blue in Figure 16.



**Figure 16.** The subset area containing Purple Mountain displayed by R: G: B = 5(NIR): 3(Red): 2(Blue).



### **5.2.2 Segmentation**

The first step of an eCognition image analysis is to cut the image into pieces, which serve as building blocks for further analysis. This step is called segmentation and there is a choice of several algorithms to do this. Commonly, the term segmentation means subdividing entities, such as objects, into smaller partitions. In eCognition, however, it is differently used. Segmentation is any operation that creates new image objects or alters the morphology of existing image objects according to specific criteria. This means that a segmentation can be a subdividing operation, a merging operation, or a reshaping operation.

There are two basic segmentation principles: top-down strategy and bottom-up strategy. Top-down segmentation means cutting objects into smaller objects. It can – but does not have to – originate from the entire image as one object. The eCognition v8.8 offers three top-down segmentation methods: chessboard segmentation, quadtree-based segmentation and multi-threshold segmentation. Bottom-up segmentation means assembling objects to create larger objects. It can – but does not have to – start with the pixels of the image. Examples of bottom-up strategy are multiresolution segmentation and classification-based segmentation. The multiresolution segmentation

is the most widely used approach. Because the shape of objects in the study area is not regular, the multiresolution segmentation was used to cut the image into pieces in this study.

The multiresolution segmentation algorithm consecutively merges pixels or existing image objects [128]. Essentially, the procedure identifies single image objects of one pixel in size and merges them with their neighbors, based on relative homogeneity criteria. The homogeneity criterion of the multiresolution segmentation algorithm measures how homogeneous or heterogeneous an image object is within itself. It is calculated as a combination of the color and shape properties of the initial and resulting image objects of the intended merging. Color homogeneity is based on the standard deviation of the spectral colors. The shape homogeneity is based on the deviation of a compact (or smooth) shape. Homogeneity criteria can be customized by weighting shape and compactness criteria. The shape criterion can be given a value of up to 0.9. This ratio determines to what degree shape influences the segmentation compared to color. For example, a shape weighting of 0.6 results in a color weighting of 0.4. In the same way, the value assigned for compactness gives it a relative weighting against smoothness. Additionally, another variable called scale parameter can also affect the segmentation. Higher values for the scale

parameter result in larger image objects, smaller values in smaller ones. By testing several times, we found that the segmentation using shape weighting of 0.1, compactness weighting of 0.5, and scale parameter of 150 yielded good results. The segmented objects overlaying the subset image are displayed in Figure 17.

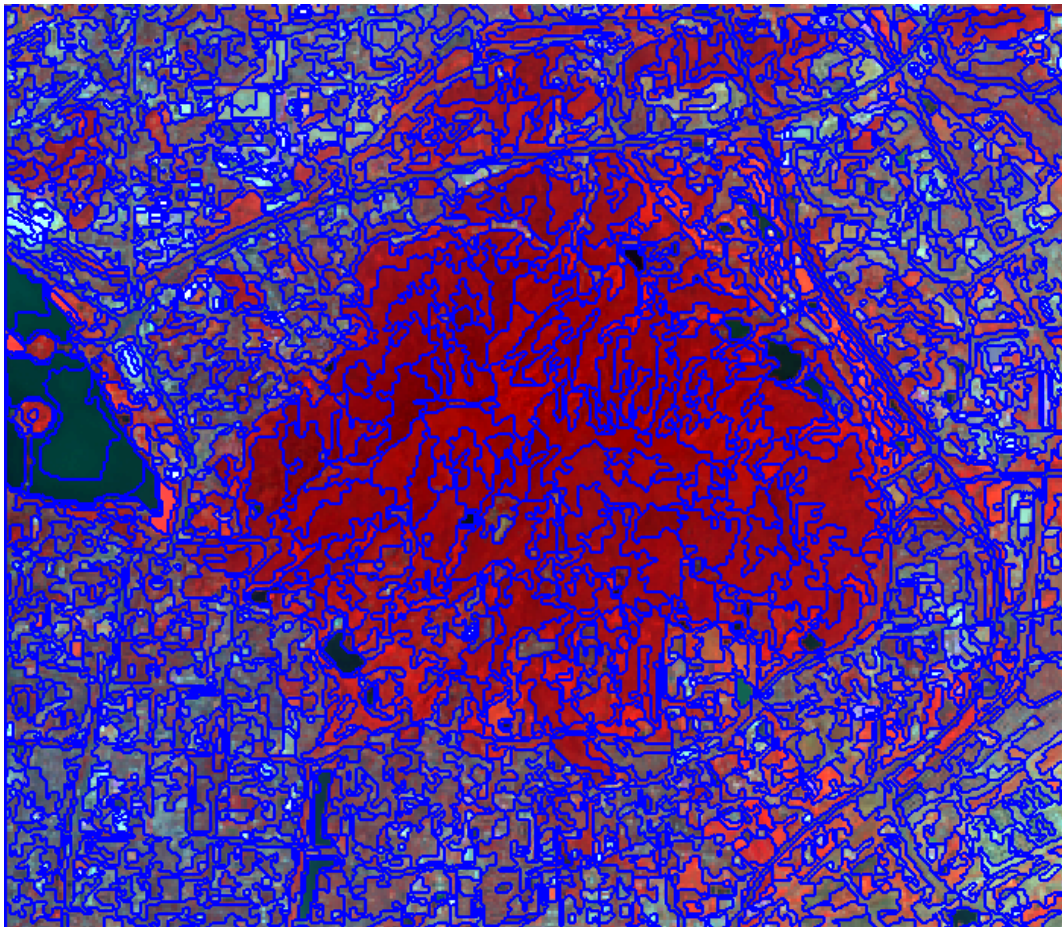


**Figure 17.** The segmentation results using shape weighting of 0.1, compactness weighting of 0.5, and scale parameter of 150. The blue lines are boundaries of the segmented objects.

### 5.2.3 Land Cover Classification

When the segmentation processing was completed, six classes: Building, Forest, Grass, Road, Soil, and Water, were created in the Class Hierarchy window of the eCognition v8.8 (Figure 18).

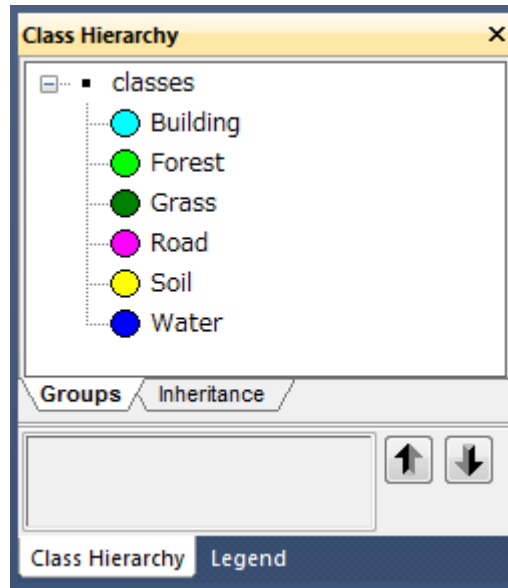


**Figure 18.** The six classes of land cover.

Next, several training samples were selected for each class. These samples are displayed in Figure 19 with the same color as the corresponding class. Then, a total of 13 feature spaces, including a customized feature (NDVI), ten spectral features (*i.e.*, the average values of the 8 bands, brightness, and max difference), and two geometry features (length/width, shape index) (Figure 20), were created and/or selected as the rules of the object-based supervised classification. The NDVI feature was calculated using the equation (4).



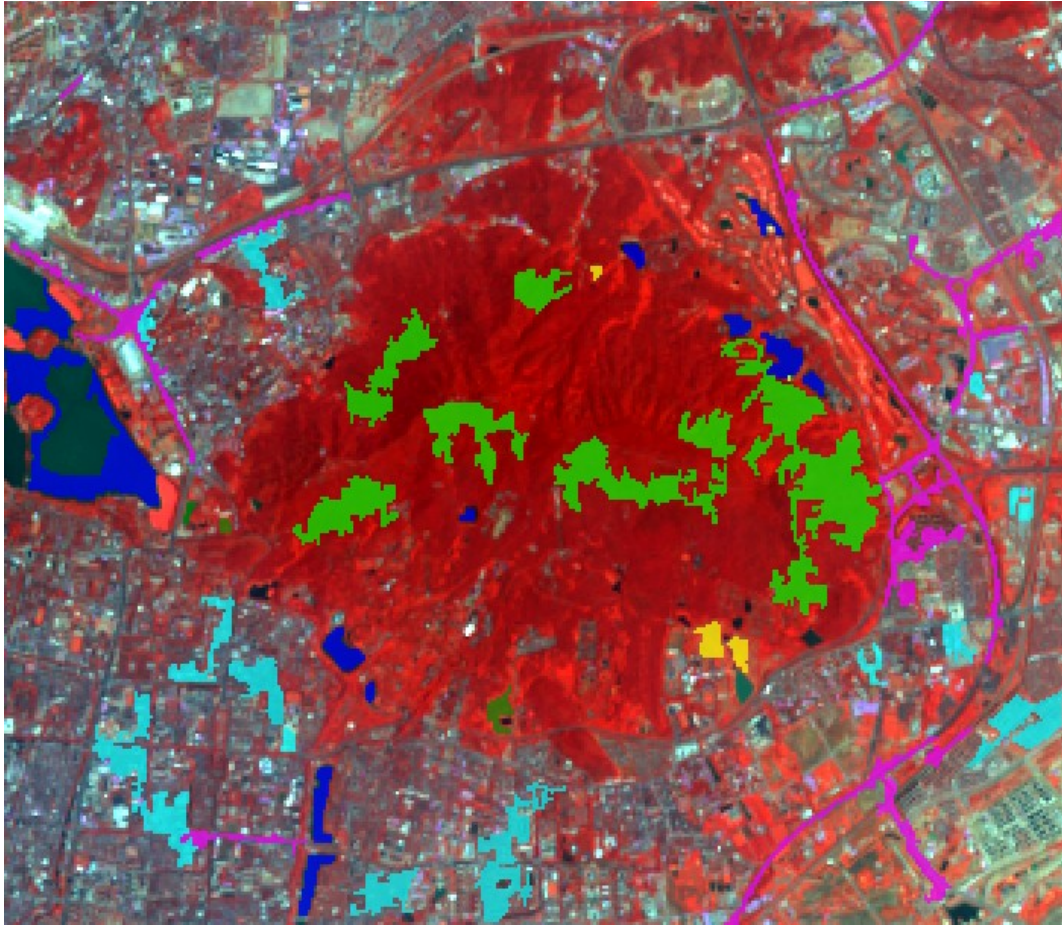


**Figure 19.** Selected training samples for the six classes. The legends are the same as in Figure 18.

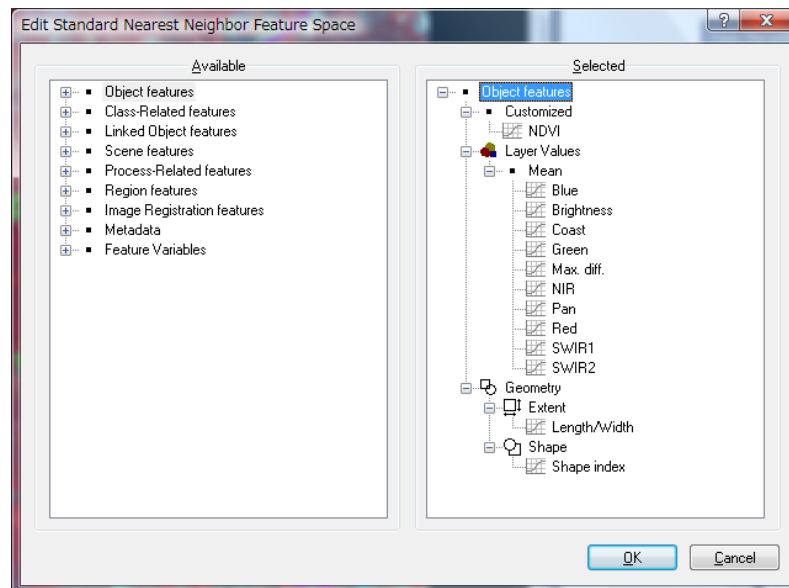


**Figure 20.** The 13 selected features for the object-based classification.

Finally, classifying the segmented objects into six classes was completed using the Nearest Neighbor classifier. The results are displayed in Figure 21. The accuracy assessment indicates that all the training samples of the six classes were correctly classified with an overall accuracy of 1 (Figure 22).

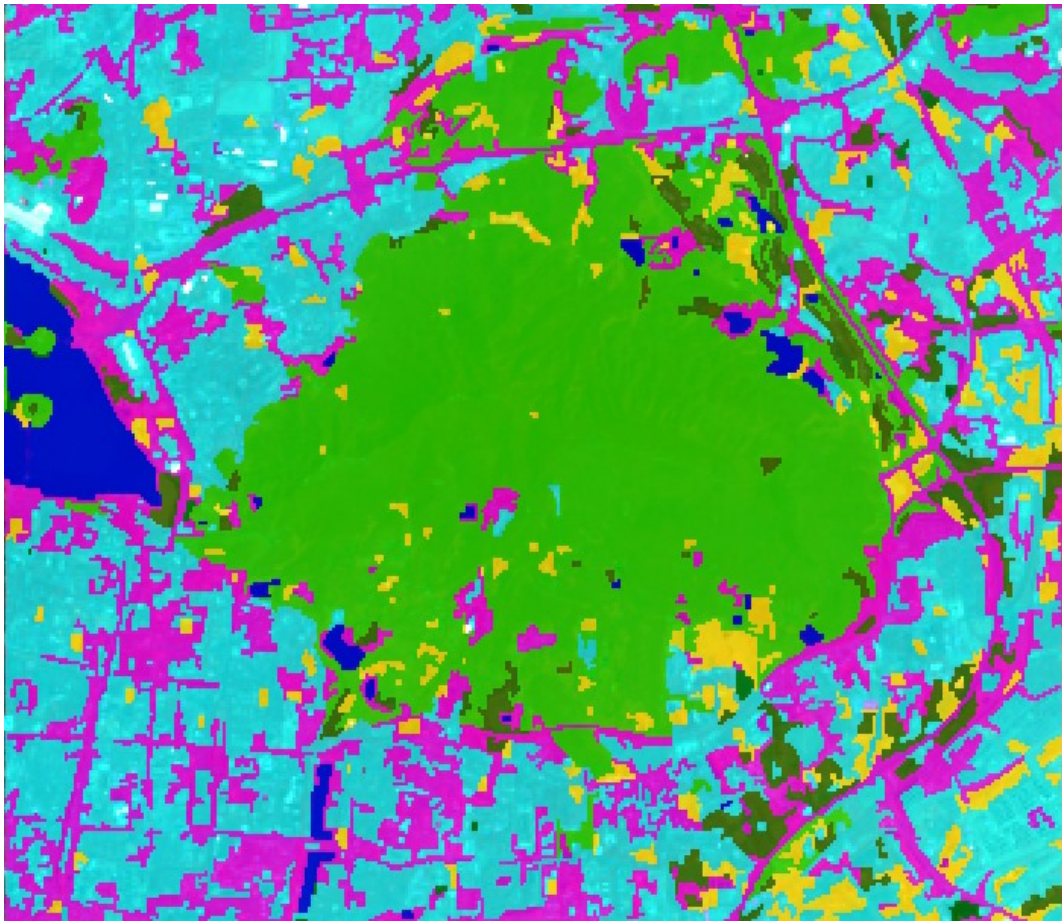


**Figure 21.** The results of object-based land cover classification using the Nearest Neighbor classifier. The legends are the same as in Figure 18.

Error Matrix based on Samples							
User Class \ Sample	Building	Grass	Forest	Road	Soil	Water	Sum
<b>Confusion Matrix</b>							
Building	15	0	0	0	0	0	15
Grass	0	3	0	0	0	0	3
Forest	0	0	8	0	0	0	8
Road	0	0	0	17	0	0	17
Soil	0	0	0	0	3	0	3
Water	0	0	0	0	0	13	13
unclassified	0	0	0	0	0	0	0
Sum	15	3	8	17	3	13	
<b>Accuracy</b>							
Producer	1	1	1	1	1	1	
User	1	1	1	1	1	1	
Hit	1	1	1	1	1	1	
Short	1	1	1	1	1	1	
KIA Per Class	1	1	1	1	1	1	
<b>Totals</b>							
Overall Accuracy	1						
KIA	1						

**Figure 22.** The results of accuracy assessment for the land cover classification.

#### 5.2.4 Forest Type Classification

Based on the results of land cover classification, the forest class was classified into three stand types: broadleaved, coniferous, and mixed forest. First, three sub-classes were created for the forest class in the Class Hierarchy window of the eCognition v8.8 software (Figure 23).

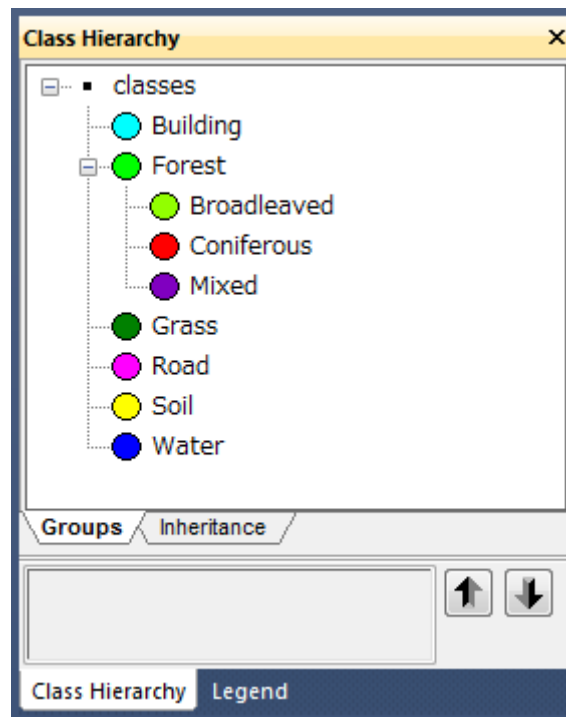


**Figure 23.** Overview of the final class hierarchy.

Second, several training samples were added to the three sub-classes based on the field data. These samples are displayed in Figure 24 with the same color as the corresponding class. Because the forest objects have irregular shapes, the two geometry features (length/width and shape index) were not used for the forest type classification. Consequently, a total of 11 feature spaces, including a



customized feature (NDVI) and ten spectral features (*i.e.*, the average values of the 8 bands, brightness, and max difference) (Figure 20), were used to classify the forest objects into three stand types.

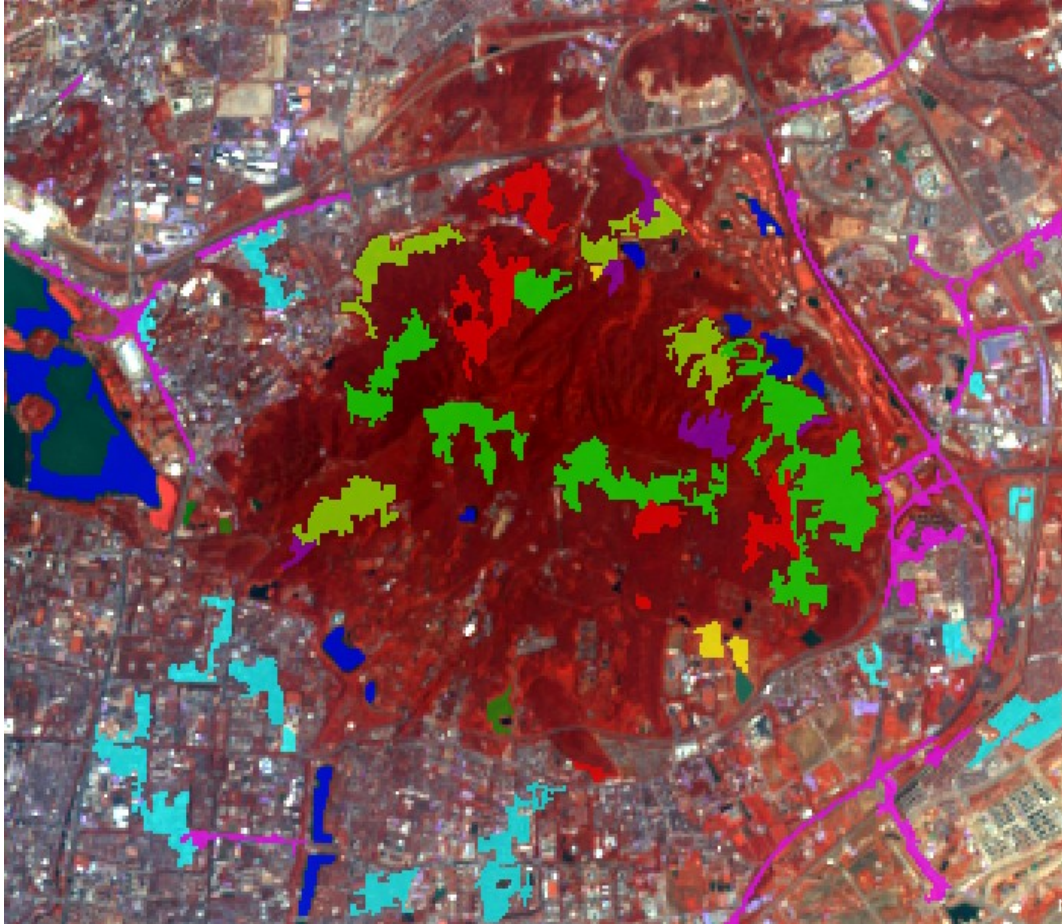


**Figure 24.** Added training samples to the three sub-classes. The legends are the same as in Figure 23.

Next, classifying the forest objects into three sub-classes was completed using the Nearest Neighbor classifier. The classification results are showed in Figure 25. The accuracy assessment indicates that most training samples of the three sub-classes were correctly classified with an overall accuracy of 91.9% (Figure 26).

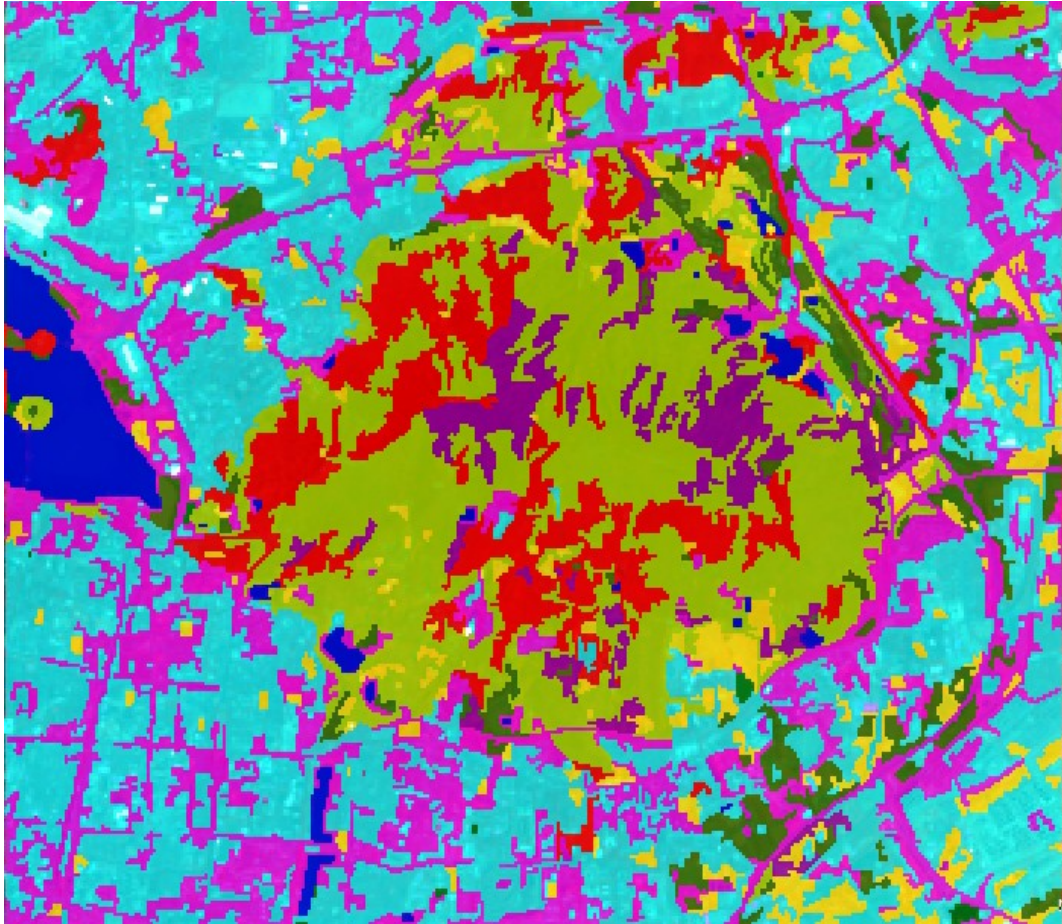


**Figure 25.** The results of forest type classification using the Nearest Neighbor classifier. The legends are the same as in Figure 23.

Error Matrix based on Samples										
User Class \ Sample	Forest	Building	Grass	Road	Soil	Water	Mixed	Coniferous	Broadleaved	Sum
<b>Confusion Matrix</b>										
Forest	0	0	0	0	0	0	0	0	0	0
Building	0	15	0	0	0	0	0	0	0	15
Grass	0	0	3	0	0	0	0	0	0	3
Road	0	0	0	17	0	0	0	0	0	17
Soil	0	0	0	0	3	0	0	0	0	3
Water	0	0	0	0	0	13	0	0	0	13
Mixed	1	0	0	0	0	0	5	0	0	6
Coniferous	0	0	0	0	0	0	0	7	0	7
Broadleaved	5	0	0	0	0	0	0	0	5	10
unclassified	0	0	0	0	0	0	0	0	0	0
Sum	6	15	3	17	3	13	5	7	5	
<b>Accuracy</b>										
Producer	0	1	1	1	1	1	1	1	1	
User	undefined	1	1	1	1	1	0.8333333	1	0.5	
Heiden	0	1	1	1	1	1	0.909	1	0.6666667	
Short	0	1	1	1	1	1	0.8333333	1	0.5	
KIA Per Class	0	1	1	1	1	1	1	1	1	
<b>Totals</b>										
Overall Accuracy	0.919									
KIA	0.9044339									

**Figure 26.** The results of accuracy assessment for forest type classification.

Finally, the adjacent objects in the same class were merged into larger objects for each class using the Merge algorithm built in the eCognition v8.8 software. The merged results were then exported to the ESRI .shp files containing the object outlines.

### **5.3 Conclusions**

A good segmentation of the study area was performed by the multiresolution approach in this study. The land cover of the study area was classified into six classes with an accuracy of 100% using the object-based classification. Additionally, the forest in the study area was classified into three stand types with an accuracy of 91.9% using the object-based classification.

## **Chapter 6 Management of Forests in the Study Area**

### **6.1 Database Establishment**

Using the results of Chapter 5, the object outlines of forest type classification were first segmented by the compartment boundaries using the Intersect function built in the ArcGIS v10 software. Second, the stem density and carbon density of these segmented sub-objects were calculated using the interpreted treetop results (Chapter 3) and the biomass map (Chapter 4). Finally, the stem density was divided into three levels: low ( $\leq 300$  stem/ha), moderate ( $> 300$  and  $\leq 500$  stem/ha), and high ( $> 500$  stem/ha), using the Natural Breaks (Jenks) algorithm, which is displayed in Figure 27. The carbon density was also divided into three levels: low ( $\leq 100$  Mg/ha), moderate ( $> 100$  and  $\leq 150$  Mg/ha), and high ( $> 150$  Mg/ha), using the Natural Breaks (Jenks) algorithm (Figure 28).



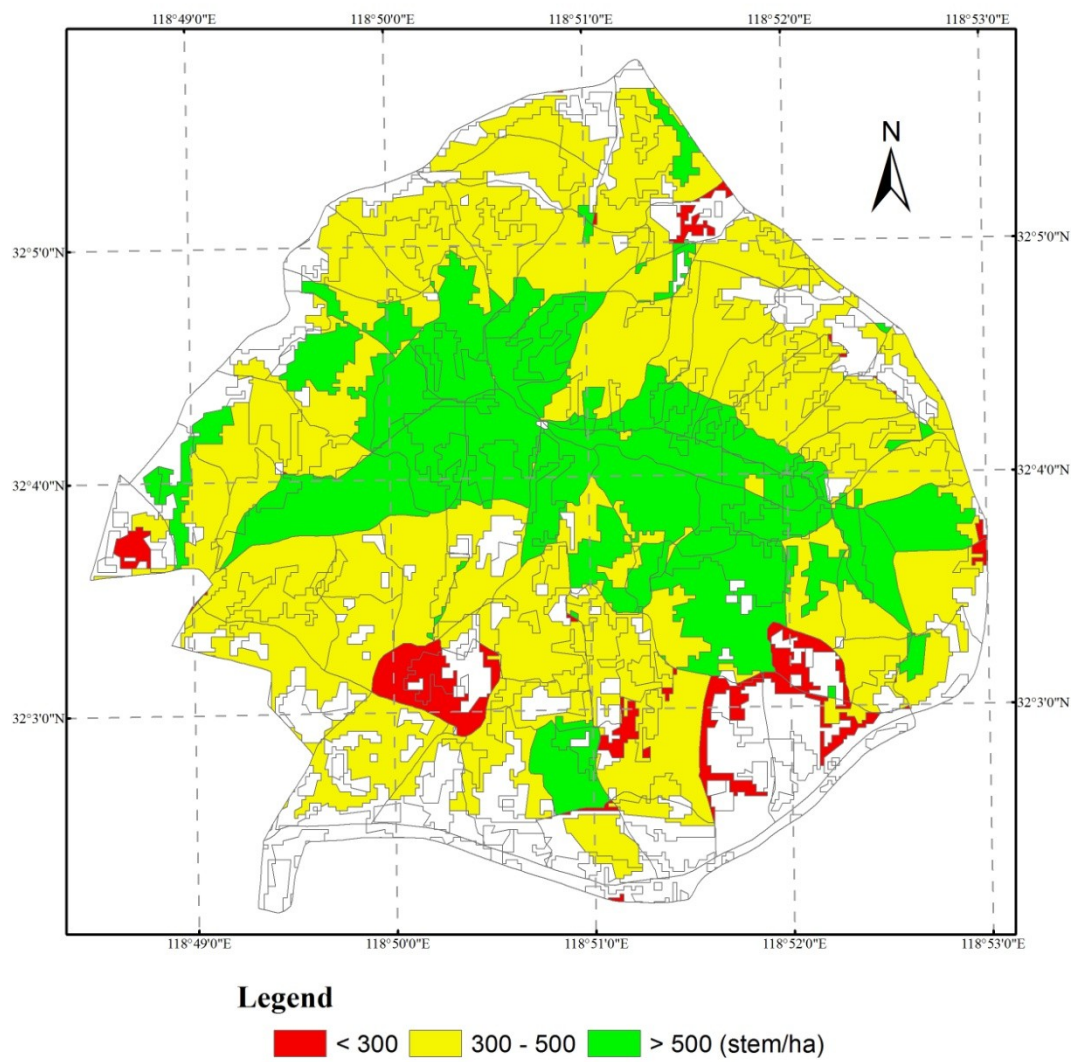


**Figure 27.** The stem density of the sub-objects segmented by the object outlines of forest type classification and the compartment boundaries.

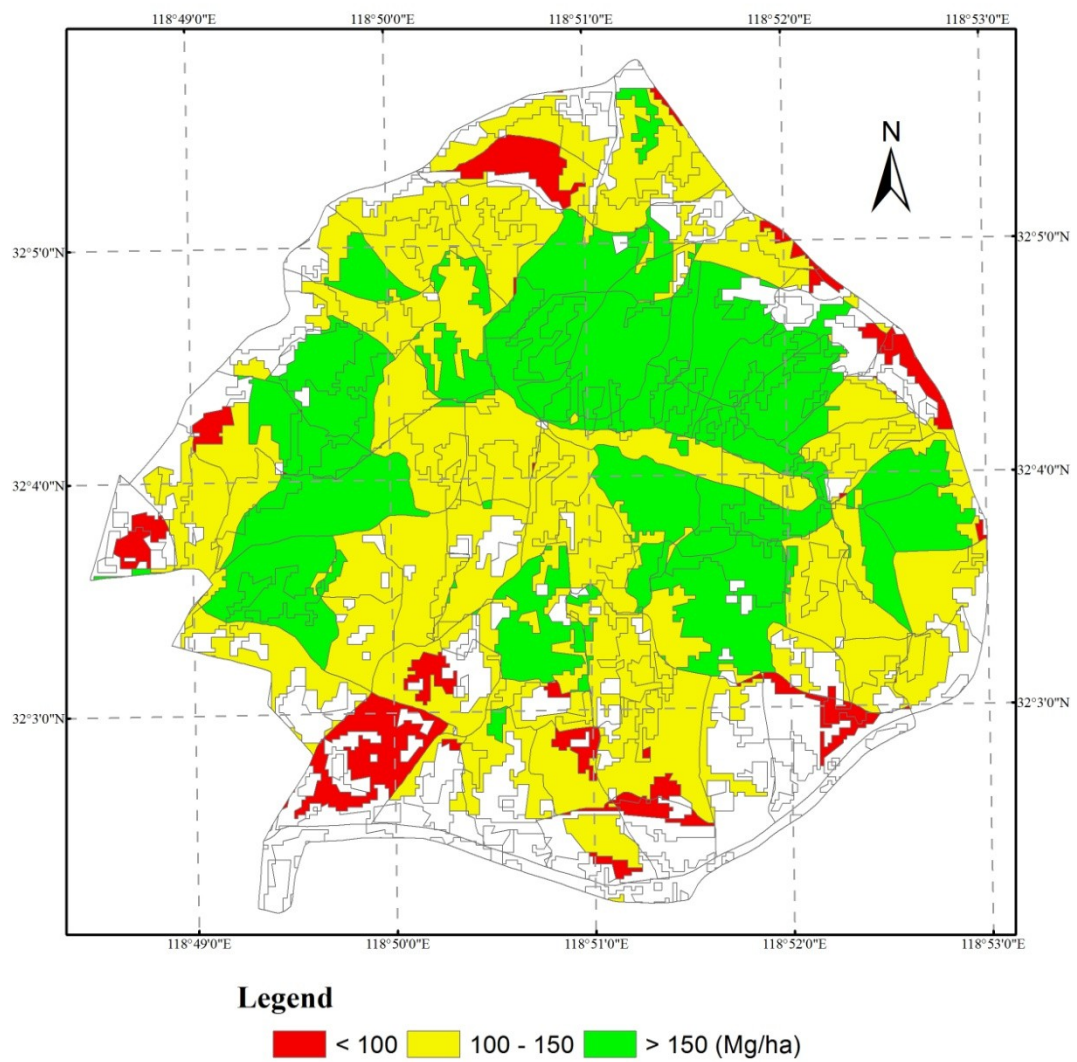


**Figure 28.** The carbon density of the sub-objects segmented by the object outlines of forest type classification and the compartment boundaries.

## 6.2 Priority Level of Forest Management

Currently, thinning and replanting are the two most common methods of forest management in China [78]. In our study, another method called promoting regeneration of young trees was recommended for managing the forests of the study area. Additionally, because the Purple Mountain is located in the center of Nanjing City, its leisure and ecological functions received increasing attention. Consequently, with the purpose of producing protection forests, the recommendations of management approaches and priority based on the stem density and carbon density are listed in Table 9.

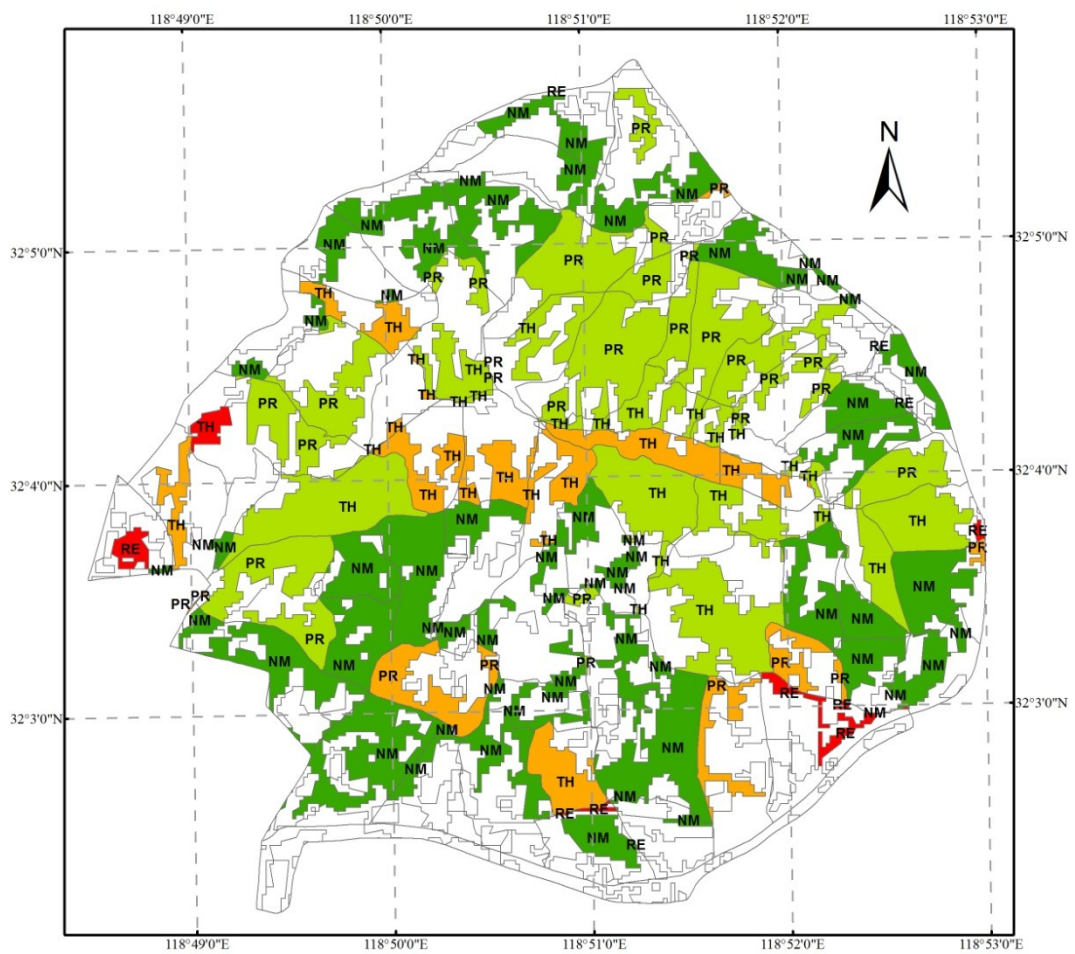
**Table 9.** The approaches and priority of forest management on the basis of stem density and carbon density.

		Biomass density (Mg/ha)		
		> 150	150 - 100	≤ 100
Stem density (stem/ha)	> 500	TH (L2)	TH (L3)	TH (L4)
	300 - 500	PR (L2)	NM (L1)	NM (L1)
	≤ 300	PR (L4)	PR (L3)	RE (L4)

TH: Thinning; PR: Promoting regeneration of young trees; RE: Replantation; NM: Non-management.

Variable *L* in brackets represents the priority level of management ( $L4 > L3 > L2 > L1$ ).

Next, the priority level of forest management was calculated using these rules in Table 9. Finally, in addition to priority level, the recommended management approaches to the forests in the previously produced sub-object area are showed in Figures 29 to 31 by distinguishing stand types.

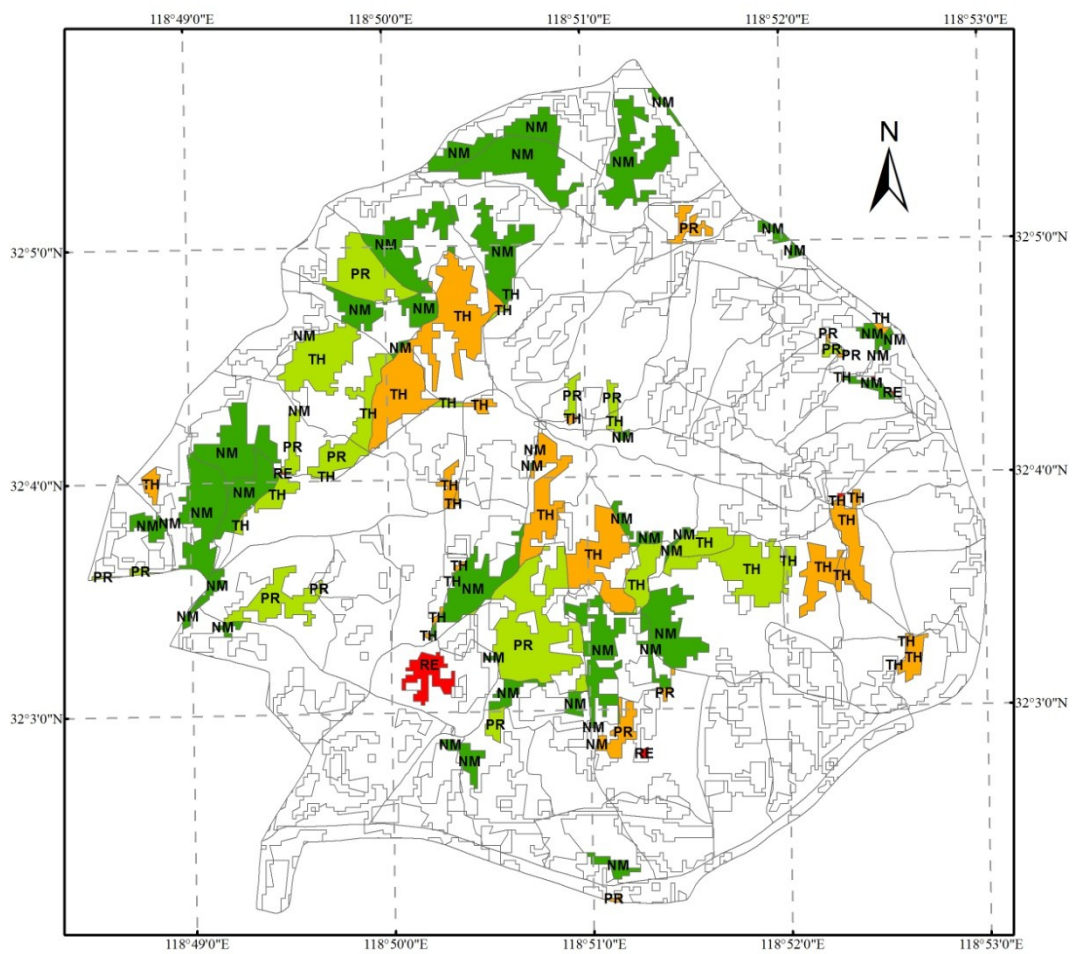


### Legend

Priority Level    ■ 1    ■ 2    ■ 3    ■ 4

**Figure 29.** Broadleaved forest management.





### Legend

Priority Level    ■ 1    ■ 2    ■ 3    ■ 4

**Figure 30.** Coniferous forest management.

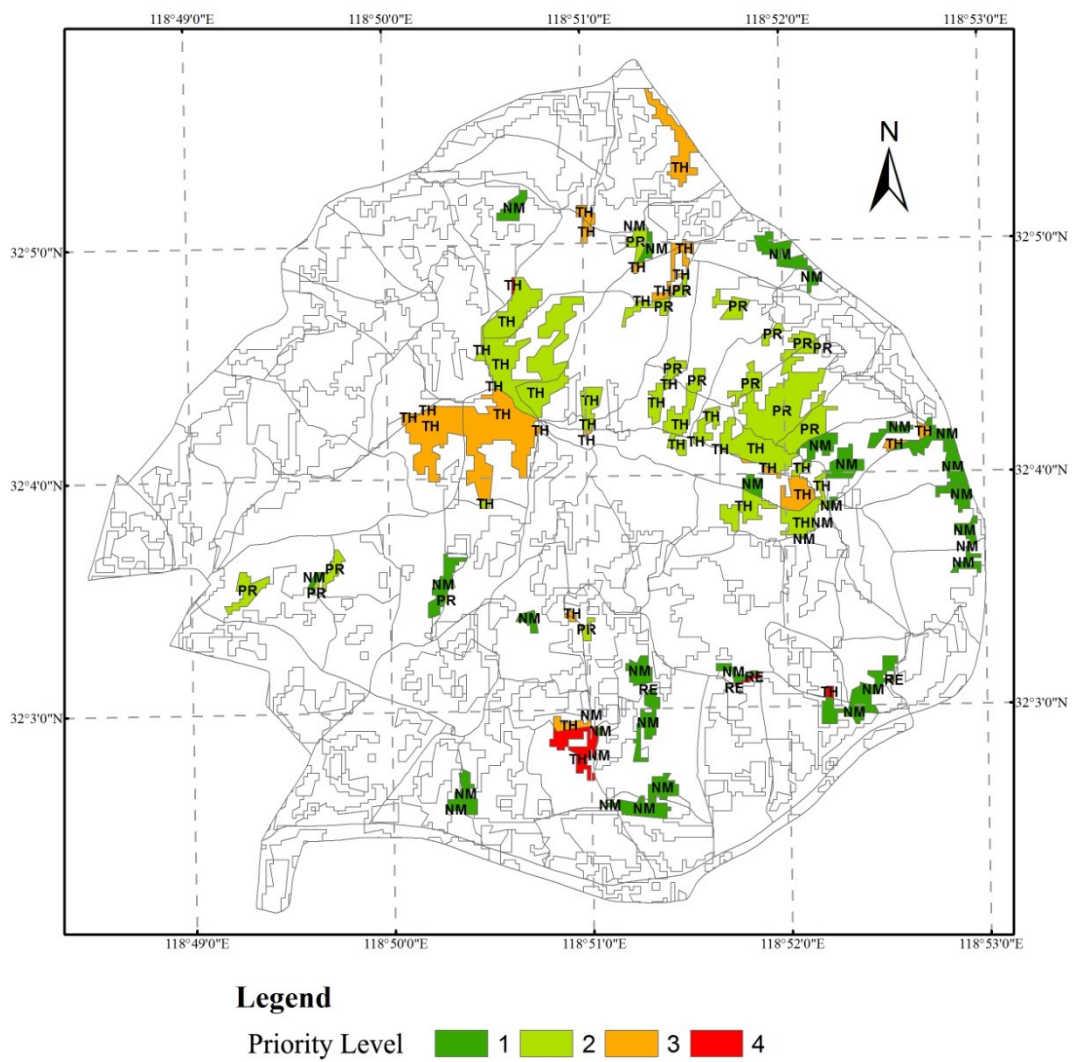


**Figure 31.** Mixed forest management.

### 6.3 Conclusions

First, our study has measured the forest resources at the individual tree level at Purple Mountain using the WorldView-2 data and the ITC approach by combining GPS, RS, and Geographic Information System (GIS) technologies. The results indicate that the forest of Purple Mountain is mainly dominated by *Quercus acutissima*, *Liquidambar formosana* and *Pinus massoniana*. Second, an improved approach to retrieving forest aboveground biomass has been developed by combining PALSAR/ALOS and WorldView-2 data. The results demonstrate that combining independent observation data from the PALSAR and WorldView-2 sources may provide great improvements for biomass estimation in the study area. Next, the forests at Purple Mountain were classified into three types: broadleaved, coniferous, and mixed forest by an object-based classification approach using the Landsat-8 image. Finally, we have developed some recommendations for the management of forests in the study area at the stand level based on the results of tree top interpretation, biomass estimation, and forest classification. The successful interpretation of forest resources at the individual tree level over large areas in this study provided the possibility of forest management at the individual tree level using the stand spatial structure theory that was completely introduced by our

previous study [129]. Consequently, the next issue is developing the professional system of semi-automatically calculating spatial structure indices and selecting the target trees for reserving or cutting using the ArcGIS Engine platform.

## **Acknowledgments**

I first wish to express sincere acknowledgment to my honorific supervisor Professor Dr. Masato KATOH, Director of the Institute of Mountain Science, Shinshu University for his thorough guidance in study and kind care in life. His insightful and valuable advice can be found in every section of this dissertation. His deeds in scientific research have been encouraging me constantly.

I would like to express my sincere appreciation to my co-supervisors: Dr. Tatsuhito UEKI and Dr. Hiroshi NAKAMURA, Professors, Faculty of Agriculture, Shinshu University for their helpful suggestions toward strengthening key elements of this dissertation and other constructive advice on my research.

Additionally, I want to express my earnest thanks to all the members of Forest Measurement and Planning Laboratory, Faculty of Agriculture, Shinshu University for their help in my research. I wish to thank Dr. Mohammad Abdullah AL FARUQ for his correction of English.

Especially, I wish to express my deep respect and special appreciation to Professor Dr. Qingwei GUAN, Forest Resources and Environment Faculty, Nanjing Forestry University for his guidance, advice, support, and care all the time. I would like to thank Professor

Dr. Mingyang LI for providing the basic data of the study area and for his advice on my research. I also want to thank the members of the Forest Ecology Laboratory, Nanjing Forestry University for their assistance with my study.

This study was financially supported by a Grant-in-Aid for Scientific Research from the Japan Society for the Promotion of Science (No. 24380077), the National Basic Research Program of China (973 program, 2012CB416904), and the Natural Science Foundation of China (Grant No. 50978054, MCDA/GIS-based spatial decision making method for recreational forest in open urban space). I want to acknowledge the helpful comments of the anonymous reviewers and editors in my manuscript submissions. Moreover, I would like to thank the Japanese Government (Monbukagakusho: MEXT) Scholarship Foundation for providing the full scholarship for me. Without this scholarship, I could not perfectly complete my research.

I gratefully thank my friends, Dr. Nan WANG and Dr. Tong ZHANG for their advice on my research and great help in my life in Japan. Additionally, I would like to express heartfelt thanks to all of my good friends living in China now for their help and great support in my study abroad.

Finally, I must express my deep sense of gratitude to my family for their selfless supports in my whole study period. Without them, I would be unable to complete my study. I want to express my miss and love to my mother. Thank you very much for leaving me so many beautiful memories. I will miss you forever.

**Thank you very much, everyone!**

By Songqiu DENG

2014.11.30

## References

1. Katoh, M.; Gougeon, F.A. Improving the precision of tree counting by combining tree detection with crown delineation and classification on homogeneity guided smoothed high resolution (50 cm) multispectral airborne digital data. *Remote Sens.* **2012**, *4*, 1411–1424.
2. Immitzer, M.; Atzberger, C.; Koukal, T. Tree species classification with random forest using very high spatial resolution 8-band WorldView-2 satellite data. *Remote Sens.* **2012**, *4*, 2661–2693.
3. State Forestry Administration of China. *The Main Results of the 7th National Forest Resource Inventory (2004–2008)* (in Chinese); 2010. Available online: <http://www.forestry.gov.cn/portal/main/s/65/content-326341.html> (accessed on 6 February 2013).
4. Ke, Y.; Zhang, W.; Quackenbush, L.J. Active contour and hill climbing for tree crown detection and delineation. *Photogramm. Eng. Remote Sens.* **2010**, *76*, 1169–1181.
5. Wulder, M.; Niemann, K.O.; Goodenough, D.G. Local maximum filtering for the extraction of tree locations and basal area from high spatial resolution imagery. *Remote Sens. Environ.* **2000**, *73*, 103–114.



6. Clark, M.L.; Roberts, D.A.; Clark, D.B. Hyperspectral discrimination of tropical rain forest tree species at leaf to crown scales. *Remote Sens. Environ.* **2005**, *96*, 375–398.
7. Larsen, M. Single tree species classification with a hypothetical multi-spectral satellite. *Remote Sens. Environ.* **2007**, *110*, 523–532.
8. Nagendra, H. Using remote sensing to assess biodiversity. *Int. J. Remote Sens.* **2001**, *22*, 2377–2400.
9. Hill, D.A.; Leckie, D.G. Forest Regeneration: Individual Tree Crown Detection Techniques for Density and Stocking Assessments. In Proceedings of the International Forum on Automated Interpretation of High Spatial Resolution Digital Imagery for Forestry, Victoria, BC, Canada, 10–12 February 1998; pp. 169–177.
10. Jensen, J.R. Remote Sensing and GIS Integration. In *Remote Sensing of the Environment: An Earth Resource Perspective*, 2nd ed.; Prentice-Hall: Englewood Cliffs, NJ, USA, 2007; pp. 544–545.
11. Katoh, M. The Identification of Large Size Trees. In *Forest Remote Sensing: Applications from Introduction* (in Japanese), 3rd ed.; Japan Forestry Investigation Committee: Tokyo, Japan, 2010; pp. 308–309.

12. Leckie, D.G.; Gillis, M.D. A Crown-Following Approach to the Automatic Delineation of Individual Tree Crowns in High Spatial Resolution Aerial Images. In Proceedings of the International Forum on Airborne Multispectral Scanning for Forestry and Mapping, Chalk River, ON, Canada, 13–16 April 1993; pp. 86–93.
13. Koukal, T.; Atzberger, C. Potential of multi-angular data derived from a digital aerial frame camera for forest classification. *IEEE J. Sel. Top. Appl. Earth Obs. Remote Sens.* **2012**, *5*, 30–43.
14. Gougeon, F.A.; Leckie, D.G. The individual tree crown approach applied to IKONOS images of a coniferous plantation area. *Photogramm. Eng. Remote Sens.* **2006**, *72*, 1287–1297.
15. Katoh, M. Comparison of high resolution IKONOS imageries to interpret individual trees (in Japanese with English abstract). *J. Jpn. For. Soc.* **2002**, *84*, 221–230.
16. Wang, L.; Gong, P.; Biging, G.S. Individual tree-crown delineation and treetop detection in high-spatial resolution aerial imagery. *Photogramm. Eng. Remote Sens.* **2004**, *70*, 351–357.
17. Erikson, M. Segmentation of individual tree crowns in color aerial photographs using region growing supported by fuzzy rules. *Can. J. For. Res.* **2003**, *33*, 1557–1563.

18. Katoh, M.; Gougeon, F.A.; Leckie, D.G. Application of high-resolution airborne data using individual tree crown in Japanese conifer plantations. *J. For. Res.* **2009**, *14*, 10–19.
19. Leckie, D.G.; Gougeon, F.A.; Walsworth, N.; Paradine, D. Stand delineation and composition estimation using semi-automated individual tree crown analysis. *Remote Sens. Environ.* **2003**, *85*, 355–369.
20. Leckie, D.G.; Gougeon, F.A.; Tinis, S.; Nelson, T.; Burnett, C.N.; Paradine, D. Automated tree recognition in old growth conifer stands with high resolution digital imagery. *Remote Sens. Environ.* **2005**, *94*, 311–326.
21. Pollock, R. A Model-Based Approach to Automatically Locating Individual Tree Crowns in High-Resolution Images of Forest Canopies. In Proceedings of the First International Airborne Remote Sensing Conference and Exhibition, Strasbourg, France, 12–15 September 1994; pp. 11–15.
22. Culvenor, D.S. Extracting Individual Tree Information. In *Remote Sensing of Forest Environment: Concepts and Case Studies*; Wulder, M., Franklin, S.E., Eds.; Kluwer Academic Publishers: Boston, MA, USA/Dordrecht, The Netherlands/London, UK, 2003; pp. 255–278.

23. Erikson, M.; Olofsson, K. Comparison of three individual tree crown detection methods. *Mach. Vis. Appl.* **2005**, *16*, 258–265.
24. Gougeon, F.A. A crown following approach to the automatic delineation of individual tree crowns in high spatial resolution aerial images. *Can. J. Remote Sens.* **1995**, *21*, 274–284.
25. Ke, Y.; Quackenbush, L.J. A comparison of three methods for automatic tree crown detection and delineation methods from high spatial resolution imagery. *Int. J. Remote Sens.* **2011**, *32*, 3625–3647.
26. Mutanga, O.; Adma, E.; Cho, M.A. High density biomass estimation for wetland vegetation using WorldView-2 imagery and random forest regression algorithm. *Int. J. Appl. Earth Obs. Geoinf.* **2012**, *18*, 399–406.
27. Sridharan, H. Multi-level Urban Forest Classification Using the WorldView-2 8-Band Hyperspectral Imagery. In *8 Bands Research Challenge*; DigitalGlobe: Longmont, CO, USA, 2010.
28. Gougeon, F.A. *The ITC Suite Manual: A Semi-Automatic Individual Tree Crown (ITC) Approach to Forest Inventories*; Pacific Forestry Centre, Canadian Forest Service, Natural Resources Canada: Victoria, BC, Canada, 2010; pp. 1–92.

29. Canadell, J.; Ciais, P.; Cox, P.; Heimann, M. Quantifying, understanding and managing the carbon cycle in the next decades. *Climatic Change* **2004**, *67*, 147–160.
30. Campbell, B. Beyond Copenhagen: REDD plus, agriculture, adaptation strategies and poverty. *Glob. Environ. Change-Human and Policy Dimens.* **2009**, *19*, 397–399.
31. Peregon, A.; Yamagata, Y. The use of ALOS/PALSAR backscatter to estimate above-ground forest biomass: A case study in Western Siberia. *Remote Sens. Environ.* **2013**, *137*, 139–146.
32. Gibbs, H.K.; Brown, S.; Niles, J.O.; Foley, J.A. Monitoring and estimating tropical forest carbon stocks: Making REDD a reality. *Environ. Res. Lett.* **2007**, *2*, doi:10.1088/1748-9326/2/4/045023.
33. Herold, M.; Johns, T. Linking requirements with capabilities for deforestation monitoring in the context of the UNFCCC-REDD process. *Environ. Res. Lett.* **2007**, *2*, doi:10.1088/1748-9326/2/4/045025.
34. Avitabile, V.; Baccini, A.; Friedl, M.A.; Schmulius, C. Capabilities and limitations of Landsat and land cover data for aboveground woody biomass estimation of Uganda. *Remote Sens. Environ.* **2012**, *117*, 366–380.

35. Franklin, J. Thematic mapper analysis of coniferous forest structure and composition. *Int. J. Remote Sens.* **1986**, *7*, 1287–1301.
36. Steininger, M. Satellite estimation of tropical secondary forest above-ground biomass: Data from Brazil and Bolivia. *Int. J. Remote Sens.* **2000**, *21*, 1139–1157.
37. Ozdemir, I.; Karnieli, A. Predicting forest structural parameters using the image texture derived from WorldView-2 multispectral imagery in a dryland forest, Israel. *Int. J. Appl. Earth Obs. Geoinf.* **2011**, *13*, 701–710.
38. Foody, G.M.; Boyd, D.S.; Cutler, M.E.J. Predictive relations of tropical forest biomass from Landsat TM data and their transferability. *Remote Sens. Environ.* **2003**, *85*, 463–474.
39. Zheng, G.; Chen, J.M.; Tian, Q.J.; Ju, W.M.; Xia, X.Q. Combining remote sensing imagery and forest age inventory for biomass mapping. *J. Environ. Manag.* **2007**, *85*, 616–623.
40. Powell, S.L.; Cohen, W.B.; Healey, S.P.; Kennedy, R.E.; Moisen, G.G.; Pierce, K.B.; Ohmann, J.L. Quantification of live aboveground forest biomass dynamics with Landsat time-series and field inventory data: A comparison of empirical modeling approaches. *Remote Sens. Environ.* **2010**, *114*, 1053–1068.

41. Mutanga, O.; Skidmore, A.K. Narrow band vegetation indices overcome the saturation problem in biomass estimation. *Int. J. Remote Sens.* **2004**, *25*, 3999–4014.
42. Labrecque, S.; Fournier, R.A.; Luther, J.E.; Piercey, D. A comparison of four methods to map biomass from Landsat-TM and inventory data in western Newfoundland. *For. Ecol. Manag.* **2006**, *226*, 129–144.
43. Duncanson, L.; Niemann, K.; Wulder, M. Integration of GLAS and Landsat TM data for aboveground biomass estimation. *Can. J. Remote Sens.* **2010**, *36*, 129–141.
44. Lu, D.S. The potential and challenge of remote sensing-based biomass estimation. *Int. J. Remote Sens.* **2006**, *27*, 1297–1328.
45. Wulder, M.A. Optical remote-sensing techniques for the assessment of forest inventory and biophysical parameters. *Prog. Phys. Geogr.* **1998**, *22*, 449–476.
46. Wang, Y.; Kasischke, E.S.; Melack, J.M.; Davis, F.W.; Christensen, N.L., Jr. The effects of changes in loblolly pine biomass and soil moisture on ERS-1 SAR backscatter. *Remote Sens. Environ.* **1994**, *49*, 25–31.

47. Hamdan, O.; Aziz, H.K.; Rahman, K.A. Remotely sensed L-Band SAR data for tropical forest biomass estimation. *J. Trop. For. Sci.* **2011**, *23*, 318–327.
48. Dobson, M.C.; Ulaby, F.T.; LeToan, T.; Beaudoin, A.; Kasischke, E.S.; Christensen, N. Dependence of radar backscatter on coniferous forest biomass. *IEEE Trans. Geosci. Remote Sens.* **1992**, *30*, 412–415.
49. Castel, T.; Beaudoin, A.; Stach, N.; Stussi, N.; Le Toan, T.; Durand, P. Sensitivity of space-borne SAR data to forest parameters over sloping terrain. Theory and experiment. *Int. J. Remote Sens.* **2001**, *22*, 2351–2376.
50. Sandberg, G.; Ulander, L.M.H.; Fransson, J.E.S.; Holmgren, J.; Le Toan, T. L and P-band backscatter intensity for biomass retrieval in hemiboreal forest. *Remote Sens. Environ.* **2011**, *115*, 2874–2886.
51. Cloude, S.R.; Pottier, E. An entropy based classification scheme for land applications of polarimetric SAR. *IEEE Trans. Geosci. Remote Sens.* **1997**, *35*, 68–78.
52. Englhart, S.; Keuck, V.; Siegert, F. Aboveground biomass retrieval in tropical forests—The potential of combined X- and L-band SAR data use. *Remote Sens. Environ.* **2011**, *115*, 1260–1271.



53. Rosenqvist, A.; Shimada, M.; Ito, N.; Watanabe, M. ALOS PALSAR: A pathfinder mission for global-scale monitoring of the environment. *IEEE Trans. Geosci. Remote Sens.* **2007**, *45*, 3307–3316.
54. Hoan, N.T.; Tateishi, R.; Alsaadeh, B.; Ngigi, T.; Alimuddin, I.; Johnson, B. Tropical forest mapping using a combination of optical and microwave data of ALOS. *Int. J. Remote Sens.* **2013**, *34*, 139–153.
55. Santos, J.R.; Freitas, C.C.; Araujo, L.S.; Dutra, L.V.; Mura, J.C.; Gama, F.F.; Soler, L.S.; Sant’Anna, S.J.S. Airborne P-band SAR applied to the aboveground biomass studies in the Brazilian tropical rainforest. *Remote Sens. Environ.* **2003**, *87*, 482–493.
56. Carreiras, J.M.B.; Vasconcelos, M.J.; Lucas, R.M. Understanding the relationship between aboveground biomass and ALOS PALSAR data in the forests of Guinea-Bissau (West Africa). *Remote Sens. Environ.* **2012**, *121*, 426–442.
57. Cartus, O.; Santoro, M.; Kelldorfer, J. Mapping forest aboveground biomass in the Northeastern United States with ALOS PALSAR dual-polarization L-band. *Remote Sens. Environ.* **2012**, *124*, 466–478.

58. Häme, T.; Rauste, Y.; Antropov, O.; Ahola, H.A.; Kilpi, J. Improved mapping of tropical forests with optical and SAR imagery, Part II: Above ground biomass estimation. *IEEE J. Sel. Top. Appl. Earth Obs. Remote Sens.* **2013**, *6*, 92–101.
59. He, Q.S.; Cao, C.X.; Chen, E.X.; Sun, G.Q.; Ling, F.L.; Pang, Y.; Zhang, H.; Ni, W.J.; Xu, M.; Li, Z.Y.; *et al.* Forest stand biomass estimation using ALOS PALSAR data based on LiDAR-derived prior knowledge in the Qilian Mountain, western China. *Int. J. Remote Sens.* **2012**, *33*, 710–729.
60. Lefsky, M.A.; Cohen, W.B.; Acker, S.A.; Parker, G.G.; Spies, T.A.; Harding, D. Lidar remote sensing of the canopy structure and biophysical properties of Douglas-fir western hemlock forests. *Remote Sens. Environ.* **1999**, *70*, 339–361.
61. Montesano, P.M.; Cook, B.D.; Sun, G.; Simard, M.; Nelson, R.F.; Ranson, K.J.; Zhang, Z.; Luthcke, S. Achieving accuracy requirements for forest biomass mapping: A spaceborne data fusion method for estimating forest biomass and LiDAR sampling error. *Remote Sens. Environ.* **2013**, *130*, 153–170.
62. Popescu, S.C.; Wynne, R.H.; Scrivani, J.A. Fusion of small-footprint LiDAR and multi-spectral data to estimate

- plot-level volume and biomass in deciduous and pine forests in Virginia, USA. *For. Sci.* **2004**, *50*, 551–565.
63. Næsset, E.; Gobakken, T. Estimation of above- and below-ground biomass across regions of the boreal forest zone using airborne laser. *Remote Sens. Environ.* **2008**, *112*, 3079–3090.
  64. Zhao, K.G.; Popescu, S.; Nelson, R. LiDAR remote sensing of forest biomass: A scale invariant estimation approach using airborne lasers. *Remote Sens. Environ.* **2009**, *113*, 182–196.
  65. Boudreau, J.; Nelson, R.; Margolis, H.; Beaudoin, A.; Guindon, L.; Kimes, D. Regional aboveground forest biomass using airborne and spaceborne LiDAR in Québec. *Remote Sens. Environ.* **2008**, *112*, 3876–3890.
  66. Mitchard, E.T.A.; Saatchi, S.S.; White, L.J.T.; Abernethy, K.A.; Jeffery, K.J.; Lewis, S.L.; Collins, M.; Lefsky, M.A.; Leal, M.E.; Woodhouse, I.H.; *et al.* Mapping tropical forest biomass with radar and spaceborne LiDAR in Lopé National Park, Gabon: Overcoming problems of high biomass and persistent cloud. *Biogeosciences* **2012**, *9*, 179–191.
  67. Tsui, O.W.; Coops, N.C.; Wulder, M.A.; Marshall, P.L.; McCardle, A. Using multi-frequency radar and discrete-return LiDAR measurements to estimate above-ground biomass and biomass

- components in a coastal temperate forest. *ISPRS J. Photogram. Remote Sens.* **2012**, *69*, 121–133.
68. Nelson, R.; Kimes, D.S.; Salas, W.A.; Routhier, M. Secondary forest age and tropical forest biomass estimation using thematic mapper imagery. *BioScience* **2000**, *50*, 419–431.
  69. Zheng, D.; Rademacher, J.; Chen, J.; Crow, T.; Bresee, M.; Moine, J.L.; Ryu, S.R. Estimating aboveground biomass using Landsat 7 ETM+ data across a managed landscape in northern Wisconsin, USA. *Remote Sens. Environ.* **2004**, *93*, 402–411.
  70. Omar, H. Commercial timber tree species identification using multispectral worldview-2 data. In *8-Bands Research Challenge*; Digital Globe: Longmont, CO, USA, 2010.
  71. Deng, S.; Katoh, M.; Guan, Q.; Yin, N.; Li, M. Interpretation of forest resources at the individual tree level at Purple Mountain, Nanjing City, China, using WorldView-2 imagery by combining GPS, RS and GIS technologies. *Remote Sens.* **2014**, *6*, 87–110.
  72. Peerbhay, K.Y.; Mutanga, O.; Ismail, R. Investigating the capability of few strategically placed Worldview-2 multispectral bands to discriminate forest species in KwaZulu-Natal, South Africa. *IEEE J. Sel. Top. Appl. Earth Obs. Remote Sens.* **2014**, *7*, 307–316.

73. Eckert, S. Improved forest biomass and carbon estimations using texture measures from WorldView-2 satellite data. *Remote Sens.* **2012**, *4*, 810–829.
74. Sun, G.; Ranson, K.J.; Guo, Z.; Zhang, Z.; Montesano, P.; Kimes, D. Forest biomass mapping from Lidar and radar synergies. *Remote Sens. Environ.* **2011**, *115*, 2906–2916.
75. Cutler, M.E.J.; Boyd, D.S.; Foody, G.M.; Vetrivel, A. Estimating tropical forest biomass with a combination of SAR image texture and Landsat TM data: An assessment of predictions between regions. *ISPRS J. Photogram. Remote Sens.* **2012**, *70*, 66–77.
76. XinhuaNet. *The development of the national forest parks in China in the recent 30 years* (in Chinese); 2012. Available online: [http://news.xinhuanet.com/politics/2012-09/20/c\\_113144120.htm](http://news.xinhuanet.com/politics/2012-09/20/c_113144120.htm) (accessed on 15 November 2013).
77. Deng, S.; Yan, J.; Guan, Q.; Katoh, M. Short-term effects of thinning intensity on scenic beauty values of different stands. *J. For. Res.* **2013**, *18*, 209–219.
78. Deng, S.; Yin, N.; Guan, Q.; Katoh, M. Dynamic response of the scenic beauty value of different forests to various thinning intensities in central eastern China. *Environ. Monit. Assess.* **2014**, *186*, 7413–7429.

79. Deng, S.; Katoh, M.; Guan, Q.; Yin, N.; Li, M. Estimating forest aboveground biomass by combining ALOS PALSAR and WorldView-2 data: A case study at Purple Mountain National Park, Nanjing, China. *Remote Sens.* **2014**, *6*, 7878–7910.
80. Jiangsu Forestry Investigation and Planning Institute. *Report on the Forest Resources of the Purple Mountain National Park*; Purple Mountain National Park Administration: Nanjing, China, 2002; pp. 1–183. (In Chinese)
81. Gougeon, F.A.; Leckie, D.G. *Forest Information Extraction from High Spatial Resolution Images Using an Individual Tree Crown Approach*; Canadian Forest Service: Victoria, BC, Canada, 2003; p. 27.
82. Landgrebe, D.; Biehl, L. *An Introduction to MultiSpec (Version 5.01)*; Purdue University: West Lafayette, IN, USA, 2001; p. 27.
83. Whiteside, T.G.; Boggs, G.S.; Maier, S.W. Comparing object-based and pixel-based classifications for mapping savannas. *Int. J. Appl. Earth Obs. Geoinf.* **2011**, *13*, 884–893.
84. Yan, G.; Mas, J.F.; Maathuis, B.H.P.; Zhang, X.; van Dijk, P.M. Comparison of pixel-based and object-oriented image classification approaches—A case study in a coal fire area, Wuda, Inner Mongolia, China. *Int. J. Remote Sens.* **2006**, *27*, 4039–4055.

85. Haara, A.; Haarala, M. Tree species classification using semi-automatic delineation of trees on aerial images. *Scand. J. For. Res.* **2002**, *17*, 556–565.
86. Katoh, M. Classifying tree species in a northern mixed forest using high-resolution IKONOS data. *J. For. Res.* **2004**, *9*, 7–14.
87. Schlerf, M.; Atzberger, C. Vegetation structure retrieval in beech and spruce forests using spectrodirectional satellite data. *IEEE J. Sel. Top. Appl.* **2012**, *5*, 8–17.
88. Sridharan, H. Multi-Level Comparison of WorldView-2 8-Band and AISA Hyperspectral Imageries for Urban Forest Classification. In *8-Band Research Challenge*; DigitalGlobe: Longmont, CO, USA, 2011.
89. Katoh, M. Tree Height Measurement Using LiDAR Data. In *Forest Remote Sensing: Applications from Introduction* (in Japanese); Japan Forestry Investigation Committee: Tokyo, Japan, 2004.
90. Chave, J.; Andalo, C.; Brown, S.; Cairns, M.A.; Chambers, J.Q.; Eamus, D.; Folster, H.; Fromard, F.; Higuchi, N.; Kira, T.; *et al.* Tree allometry and improved estimation of carbon stocks and balance in tropical forests. *Oecologia* **2005**, *145*, 87–99.

91. Fang, J.; Liu, G.; Xu, S. Biomass and net production of forest vegetation in China. *Acta. Ecol. Sin.* **1996**, *16*, 497–508. (In Chinese with English abstract)
92. Shimada, M.; Isoguchi, O.; Tadono, I.; Isono, K. PALSAR polarimetric calibration and geometric calibration. *IEEE Trans. Geosci. Remote Sens.* **2009**, *47*, 3915–3932.
93. Kim, C. Quantative analysis of relationship between ALOS PALSAR backscatter and forest stand volume. *J. Marine Sci. Tech.* **2012**, *20*, 624–628.
94. Freeman, A.; Durden, S.L. A three-component scattering model for Polarimetric SAR data. *IEEE Trans. Geosci. Remote Sens.* **1998**, *36*, 963–973.
95. Yamaguchi, Y.; Moriyama, T.; Ishido, M.; Yamada, H. Four-component scattering model for Polarimetric SAR image decomposition. *IEEE Trans. Geosci. Remote Sens.* **2005**, *43*, 1699–1706.
96. Van Zyl, J.J.; Arii, M.; Kim, Y. Model-Based decomposition of Polarimetric SAR covariance matrices constrained for nonnegative eigenvalues. *IEEE Trans. Geosci. Remote Sens.* **2011**, *49*, 3452–3459.



97. Avtar, R.; Sawada, H.; Takeuchi, W.; Singh, G. Characterization of forests and deforestation in Cambodia using ALOS/PALSAR observation. *Geocarto. Int.* **2012**, *27*, 119–137.
98. Cloude, S.R.; Pottier, E. A review of target decomposition theorems in radar Polarimetry. *IEEE Trans. Geosci. Remote Sens.* **1996**, *34*, 498–518.
99. Qi, Z.; Yeh, A.G.; Li, X.; Lin, Z. Land use and land cover classification using RADARSAT-2 polarimetric SAR image. *Int. Arch. Photogram. Remote Sens.* **2010**, *XXXVIII*, 198–203.
100. Kim, Y.; van Zyl, J. Comparison of forest parameter estimation techniques using SAR data. In Proceedings of IEEE 2001 International Geoscience and Remote Sensing Symposium (IGARSS), Sydney, NSW, Australia, 9–13 July 2001; pp. 1395–1397.
101. Foody, G.M.; Cutler, M.E.; McMorrow, J.; Pelz, D.; Tangki, H.; Boyd, D.S.; Douglas, I. Mapping the biomass of Bornean tropical rain forest from remotely sensed data. *Glob. Ecol. Biogeogr.* **2001**, *10*, 379–387.
102. Dong, J.; Kaufmann, R.K.; Myneni, R.B.; Tucker, C.J.; Kauppi, P.E.; Liski, J.; Buermann, W.; Alexeyev, V.; Hughes, M.K. Remote sensing estimates of boreal and temperate forest woody

- biomass: carbon pools, sources, and sinks. *Remote Sens. Environ.* **2003**, *84*, 393–410.
103. Tan, K.; Piao, S.; Peng, C.; Fang, J. Satellite-based estimation of biomass carbon stocks for northeast China's forests between 1982 and 1999. *For. Ecol. Manag.* **2007**, *240*, 114–121.
  104. Soenen, S.A.; Peddle, D.R.; Hall, R.J.; Coburn, C.A.; Hall, F.G. Estimating aboveground forest biomass from canopy reflectance model inversion in mountainous terrain. *Remote Sens. Environ.* **2010**, *114*, 1325–1337.
  105. Kasischke, E.S.; Christensen, N.L.; Bourgeau-Chavez, L.L. Correlating radar backscatter with components of biomass in loblolly pine forests. *IEEE Trans. Geosci. Remote Sens.* **1995**, *33*, 643–659.
  106. Sarker, M.L.R.; Nichol, J.; Ahmad, B.; Busu, I.; Rahman, A.A. Potential of texture measurements of two-date dual polarization PALSAR data for the improvement of forest biomass estimation. *ISPRS J. Photogram. Remote Sens.* **2012**, *69*, 146–166.
  107. Amini, J.; Tetuko Sri Sumantyo, J. Employing a method on SAR and optical images for forest biomass estimation. *IEEE Trans. Geosci. Remote Sens.* **2009**, *47*, 4020–4026.

108. Harrell, P.A.; Kasischke, E.S.; Bourgeau-Chavez, L.L.; Haney, E.M.; Christensen, N.L., Jr. Evaluation of approaches aboveground biomass in using SIR-C data. *Remote Sens. Environ.* **1997**, *59*, 223–233.
109. Ranson, K.J.; Sun, G.; Kharuk, V.I.; Kovacs, K. Characterization of forests in Western Sayani Mountains, Siberia from SAR data. *Remote Sens. Environ.* **2001**, *75*, 188–200.
110. Dobson, M.C.; Ulaby, F.T.; Pierce, L.E.; Sharik, T.L.; Bergen, K.M.; Kelldorfer, J.; Kendra, J.R.; Li, E.; Lin, Y.C.; Nashashibi, A.; *et al.* Estimation of forest biomass characteristics in northern Michigan with SIR-C/XSAR data. *IEEE Trans. Geosci. Remote Sens.* **1995**, *33*, 877–894.
111. Foody, G.M.; Green, R.M.; Curran, P.J.; Lucas, R.M.; Honzak, M.; Do Amaral, I. Observations on the relationship between SIR-C radar backscatter and the biomass of regenerating tropical forests. *Int. J. Remote Sens.* **1997**, *18*, 687–694.
112. Cohen, W.B.; Spies, T.A. Estimating structural attributes of Douglas-fir/western hemlock forest stands from Landsat and Spot imagery. *Remote Sens. Environ.* **1992**, *41*, 1–17.
113. Kurvonen, L.; Pulliainen, J.; Hallikainen, M. Retrieval of biomass in boreal forests from

- multi-temporal ERS-1 and JERS-1 SAR data. *IEEE Trans. Geosci. Remote Sens.* **1999**, *37*, 198–205.
114. Englhart, S.; Keuck, V.; Siegert, F. Modeling aboveground biomass in tropical forests using Multi-Frequency SAR data—A comparison of methods. *IEEE J. Sel. Top. Appl. Earth Obs. Remote Sens.* **2012**, *5*, 298–306.
115. Ghasemi, N.; Sahebi, M.R.; Mohammadzadeh, A. Biomass estimation of a temperate deciduous forest using wavelet analysis. *IEEE Trans. Geosci. Remote Sens.* **2012**, *51*, 765–776.
116. Ulander, L.M.H. Radiometric slope correction of synthetic-aperture radar images. *IEEE Trans. Geosci. Remote Sens.* **1996**, *34*, 1115–1122.
117. Shimada, M.; Hirosawa, H. Slope corrections to normalized RCS using SAR interferometry. *IEEE Trans. Geosci. Remote Sens.* **2000**, *38*, 1479–1484.
118. Gao, Y.; Liu, X.; Min, C.; He, H.; Yu, G.; Liu, M.; Zhu, X.; Wang, Q. Estimation of the North–South transect of Eastern China forest biomass using remote sensing and forest inventory data. *Int. J. Remote Sens.* **2013**, *34*, 5598–5610.

119. Tian, X.; Su, Z.; Chen, E.; Li, Z.; van der Tol, C.; Guo, J.; He, Q.  
Estimation of forest  
above-ground biomass using multi-parameter remote sensing data  
over a cold and arid area. *Int. J. Appl. Earth Obs. Geoinf.* **2012**, *14*,  
160–168.
120. Lucas, R.; Armston, J.; Fairfax, R.; Fensham, R.; Accad, A.;  
Carreiras, J.; Kelley, J.; Bunting, P.; Clewley, D.; Bray, S.; *et al.*  
An evaluation of the ALOS PALSAR L-band backscatter-above  
ground biomass relationship Queensland, Australia: Impacts of  
surface moisture condition and vegetation structure. *IEEE J. Sel.*  
*Top. Appl. Earth Obs. Remote Sens.* **2010**, *3*, 576–593.
121. Kasischke, E.S.; Tanase, M.A.; Bourgeau-Chavez, L.L.; Borr, M.  
Soil moisture limitations on monitoring boreal forest regrowth  
using spaceborne L-band SAR data. *Remote Sens. Environ.* **2011**,  
*115*, 227–232.
122. Gobron, N.; Pinty, B.; Verstraete, M.M. Theoretical limits to the  
estimation of the leaf area index on the basis of visible and  
near-infrared remote sensing data. *IEEE Trans. Geosci. Remote*  
*Sens.* **1997**, *35*, 1438–1445.

123. Nichol, J.E.; Sarker, M.L.R. Improved biomass estimation using the texture parameters of two high-resolution optical sensors. *IEEE Trans. Geosci. Remote Sens.* **2011**, *49*, 930–948.
124. Filella, I.; Penuelas, J. The red edge position and shape as indicators of plant chlorophyll content, biomass and hydric status. *Int. J. Remote Sens.* **1994**, *15*, 1459–1470.
125. Lucas, N.S.; Curran, P.J.; Plummer, S.E.; Danson, F.M. Estimating the stem carbon production of a coniferous forest using an ecosystem simulation model driven by the remotely sensed red edge. *Int. J. Remote Sens.* **2000**, *21*, 619–631.
126. Kokaly, R.F.; Clark, R.N. Spectroscopic determination of leaf biochemistry using band-depth analysis of absorption features and stepwise multiple linear regression. *Remote Sens. Environ.* **1999**, *67*, 267–287.
127. Morel, A.C.; Saatchi, S.S.; Malhi, Y.; Berry, N.J.; Banin, L.; Burslem, D.; Nilus, R.; Ong, R.C. Estimating aboveground biomass in forest and oil palm plantation in Sabah, Malaysian Borneo using ALOS PALSAR data. *For. Ecol. Manag.* **2011**, *262*, 1786–1798.
128. Benz, U.C.; Hofmann, P.; Willhauck, G.; Lingenfelder, I.; Heynen, M. Multi-resolution, object-oriented fuzzy analysis of

- remote sensing data for GIS-ready information. *ISPRS J. Photogram. Remote Sens.* **2004**, 58, 239–258.
129. Deng, S.; Katoh, M. Change of spatial structure characteristics of the forest in Oshiba Forest Park in 10 years. *J. For. Plann.* **2011**, 17, 9–19.